Devices and Circuit Design Strategies for Building Scalable Integrated Molecular Circuits

by

Craig D. LaBoda

Department of Electrical and Computer Engineering
Duke University

Date:_____

Approved:

_____
Alvin R. Lebeck, Supervisor

_____
Hisham Z. Massoud

_____
Daniel J. Sorin

_____
Benjamin C. Lee

Dissertation submitted in partial fulfillment of
the requirements for the degree of Doctor
of Philosophy in the Department of
Electrical and Computer Engineering in the Graduate School
of Duke University

2017

ABSTRACT

Devices and Circuit Design Strategies for Building Scalable

Integrated Molecular Circuits

by

Craig D. LaBoda

Department of Electrical and Computer Engineering
Duke University

Date:_____

Approved:

_____
Alvin R. Lebeck, Supervisor

_____
Hisham Z. Massoud

_____
Daniel J. Sorin

_____
Benjamin C. Lee

An abstract of a dissertation submitted in partial
fulfillment of the requirements for the degree
of Doctor of Philosophy in the Department of
Electrical and Computer Engineering in the Graduate School
of Duke University

2017

Abstract

Resonance energy transfer (RET) logic provides a method for building integrated molecular circuits using self-assembled networks of fluorescent molecules to perform computation. The unique operating principles and materials of these circuits make them suitable candidates for introducing computation to domains that are incompatible with conventional silicon-based systems. To realize the full potential of this technology, however, a variety of technical challenges currently preventing the design of larger, more complex systems must be overcome. Two of these primary challenges are energy loss and exciton loss. Energy loss forces the outputs from RET devices to be red-shifted from their inputs. This prevents most independently designed RET components from being cascaded with one another. Exciton loss weakens the output signals from RET devices, making it difficult to observe the computational results. Together, these forms of signal degradation constrain both the size and topology of RET systems.

This work explores new RET devices and circuit design strategies that address the above limitations. The primary contributions of this dissertation are threefold. First, a RET device capable of restoring energy in these systems is designed and experimentally demonstrated. This device enables cascading and feedback in RET logic, two circuit design concepts commonly used in large-scale digital systems. Second, a new style of RET logic design, called Pre-Charge Logic (PCL), is introduced. PCL addresses

both forms of signal loss while simultaneously providing a library of cascadable RET logic gates, many of which cannot be implemented using previous methods of RET logic design. Third, the design methods of PCL are explored and validated by simulation and experimental demonstration. Continuous-time Markov chain modeling confirms that the proposed PCL devices perform their intended Boolean operations, while an experimental demonstration of a PCL PASS gate substantiates the underlying operating principles of these devices. Collectively, these contributions pave the way for developing larger, more complex RET systems in the future.

Contents

List of Figures

Acknowledgements

First, and foremost, I would like to thank my family. My parents have always been an unending source of wisdom, encouragement, and empathy, and my brother and sister have been excellent role models ever since I was young. I cannot express how grateful I am for my family's constant positive influence.

I would like to thank my fiancée, Heather, for her continual support through the challenges of graduate school. A mentor of mine once told me that a Ph.D. program is a marathon, not a sprint, and without her encouragement, I may never have finished.

I would like to thank my advisor, Professor Chris Dwyer, for encouraging me to explore my own research ideas and for treating me more like a colleague than a student. His passion and creativity are inspiring. I would like to thank Professor Alvin Lebeck for always having an open door. Our discussions regarding this dissertation and research in general have been invaluable. I would like to thank Professor Dan Sorin for helping me pursue teaching opportunities and for his advice regarding my professional development. I would also like to thank Professor Hisham Massoud and Professor Ben Lee for serving on my committee, teaching me key engineering concepts during my course work, and showing me infinite patience whenever I had too many questions.

Last but not least, I would like to thank all of my labmates and friends that made my graduate school experience such an enjoyable one, including Arjun, Isvar, Siyang, Chris, Xiangyu, Ugonna, Heather, Vishwa, Mohammad, Viresh, and many others.

1. Introduction

Over the last several decades, advances in silicon-based integrated circuits have significantly altered everyday life. The incredible reduction in feature sizes achievable by lithographic fabrication has led to smaller, faster, and more computationally complex integrated circuits that can be embedded in almost any macroscale object we touch. Yet, even as transistor sizes approach fundamental scaling limits, certain computational domains remain inaccessible to silicon-based integrated circuits. The aqueous environments necessary for biological applications, for example, are generally incompatible with current methods of computation, simply due to the materials and operating principles of semiconductor devices. Thus, there is a need for an integrated circuit technology that introduces computation to these unexplored, molecular-scale domains.

Resonance energy transfer (RET) logic offers a promising route towards building integrated molecular circuits for such applications [1-3]. In this technology, networks of fluorescent molecules (also referred to as fluorophores, chromophores, or dyes) are spatially arranged with angstrom-level resolution using inexpensive, self-assembled DNA nanostructures. RET-based circuits move and manipulate information in the form of exciton currents, similar to the carrier currents that dictate the functionality of semiconductor devices. The unique composition and molecular scale of these circuits

make them compatible with a variety of untapped computational domains. When introduced to a liquid, for instance, RET circuits diffuse about, sensing, analyzing, and reporting the liquid's contents back to the user [4]. Entire architectures have been proposed that fit within a single cell, and with experimental evidence mounting that DNA nanostructures can be directly fabricated by living organisms, RET circuits may offer a route towards real-time analysis and manipulation of cellular information [5, 6]. Just as the continual scaling of semiconductor devices has brought computation to most macroscale objects, RET circuits have the potential to bring computation to most molecular-scale environments.

Despite this potential, RET logic currently suffers from a number of limitations that constrain both the scalability and the complexity of these systems. RET circuits are subject to two forms of signal loss: exciton loss and energy loss. Exciton loss includes any excitons that are intentionally generated at the input of a RET circuit but ultimately never reach the output of the circuit. This loss stems from less than unity transfer efficiencies between fluorophores and increases exponentially with the length of a RET network, i.e. the total number of fluorophores from input to output. Thus, exciton loss places practical limitations on the depth of any RET circuit. The second form of signal degradation, energy loss, forces the output from a RET circuit to be lower in energy than the input. This red-shifting arises from vibrational relaxations of each molecule [7].

Energy loss makes it difficult to cascade RET circuit components since the output from one component is typically too low in energy to act as the input to a subsequent component. It also prevents the use of feedback in RET systems because downstream signals are generally incompatible with upstream devices. Energy loss increases with the number of unique fluorophores between the input and the output, and thus, this form of loss also tends to scale with circuit size.

In addition to these forms of signal loss, current methods of RET logic design are limited by various constraints that restrict the complexity of these systems. First, there is currently no method for inverting signals in RET logic. Logical 0s and 1s are typically encoded as the absence and presence of excitons, and a RET-based device has yet to be designed that generates output excitons based on the absence of input excitons. Second, most RET-based devices are limited to outputting a partial sum of the inputs that are applied at runtime. This property, coupled with the lack of inversion, restricts any single RET device to performing only a subset of Boolean operations such as AND and OR, while other common operations like XOR and NAND cannot be implemented.

In this dissertation, we present new RET devices and circuit design strategies that address the challenges above and ultimately enable the creation of larger, more computationally complex integrated molecular systems. More specifically, we hypothesize the following:

"It is possible to decouple the length of RET circuits from their exciton loss and energy loss, and to expand the range of Boolean operations performed by these circuits."

In the subsequent sections, we briefly summarize how this dissertation supports the thesis statement above.

1.1 Restoring Energy in RET Systems

To overcome the energy loss in RET logic, we engineered a proof-of-principle device, called the RET relay, that takes in low energy excitons and produces high energy excitons [8]. The central component of this device is an upconverting nanoparticle (UCNP). UCNPs perform a process known as photon upconversion, in which they combine multiple low energy, near-infrared (NIR) photons to produce higher energy, visible photons [9]. The relay is composed of a single UCNP coated with two different fluorophores: one that absorbs NIR light and one that absorbs visible light. When the NIR fluorophores are excited, e.g. by external inputs or upstream fluorophores, they supply the UCNP with low energy excitons. Leveraging the UCNP's innate blue-shifting capabilities, the relay converts three or more of these excitons into a single high energy exciton that is accepted by the visible fluorophore. Thus, when placed between two RET networks, the relay serves as an energy restoring buffer, taking in the low energy signal from the upstream network and supplying a compatible high energy signal to the downstream network. Although this device works as designed, the relay trades energy

loss for substantial exciton loss, making it incompatible with large-scale systems that already suffer from low exciton throughput.

1.2 Decoupling Circuit Length and Signal Loss

Given the RET relay's inability to address exciton loss, we shifted our focus towards the development of a new method of RET logic design that overcomes both forms of signal loss, while simultaneously expanding the set of logic operations available to RET systems. This form of RET logic design, called Pre-Charge Logic (PCL), exploits a molecular phenomenon known as the dark state to temporarily toggle specific fluorophores on and off. Leveraging this modulation mechanism, we created a library of nonlinear RET logic gates that share many of the same design principles used by standard switch-based logic. This library currently includes AND, NAND, OR, NOR, XOR, XNOR, PASS, and Negated PASS (NPASS), many of which, as described earlier, cannot be achieved using current RET logic design principles. Individual PCL gates can be cascaded with one another to implement complex Boolean functions. These cascades can also be split into stages and evaluated sequentially. This multi-stage evaluation technique allows circuit designers to choose the size and complexity of each stage, thereby decoupling the overall length of the RET circuit from both its exciton loss and its energy loss.

1.3 Validating Pre-Charge Logic

PCL offers a method for designing complex, scalable RET systems. Before it can be applied in practice, however, its design principles must first be validated. To this end, we simulated each PCL gate using continuous-time Markov chain (CTMC) models of the underlying fluorophore networks [10]. These simulations provide us with the expected output from each logic gate as a function of the input combinations. They also allow us to evaluate the performance of PCL gates as a function of controllable design parameters, offering important insight regarding their implementation and optimization in the future. Most importantly, the results of these simulations confirm that PCL gates perform their intended Boolean operations. In addition to these simulations, we fabricated and characterized a working PCL PASS gate. This experimental demonstration shows that PCL gates can be feasibly designed and fabricated, and that the underlying operating principles of these devices are sound.

1.4 Contributions

The specific contributions of this dissertation are the following:

- The design and experimental demonstration of a nanoassembly that converts multiple low energy excitons into high energy excitons
- A new style of RET logic design that leverages the dark state of fluorescent molecules to modulate the flow of excitons

- A library of RET logic gates based on the above design principles including AND, NAND, OR, NOR, XOR, XNOR, PASS, and NPASS
- Design strategies for cascading these logic gates to implement complex Boolean functions that decouple the size of a RET circuit from both its exciton and energy loss
- Evaluations of the above logic gates and cascades as a function of controllable design parameters using CTMC models
- An experimental demonstration of a working PASS gate including its design, layout, fabrication, and characterization

1.5 Dissertation Outline

The remainder of this dissertation is organized in the following manner. Chapter 2 describes the fundamentals of RET logic. This includes a review of fluorescence and RET. It also provides an overview of RET-based computation, ranging from inputs and outputs to examples of logic gates designed thus far. Chapter 3 describes the design and experimental demonstration of the RET relay. Chapter 4 introduces PCL, outlining the design principles for individual logic gates and techniques for cascading these devices. Chapter 5 evaluates the performance of PCL gates and cascades using CTMC models. Chapter 6 details the experimental demonstration of a PCL PASS gate.

2. Fundamentals of RET Logic

The following chapter outlines the fundamentals of RET logic. We begin with a review of the common excitation and de-excitation pathways of fluorescent molecules. We then discuss the underlying principles of RET and the equations that govern this energy transfer phenomenon. Afterwards, we explore current methods of RET logic design and the fabrication of these circuits using DNA self-assembly.

2.1 Fluorescence

Before examining how fluorophores can be networked together to perform computation, we must first review the basic excitation and de-excitation pathways of these molecules. These pathways are best visualized using a Jablonski diagram, as displayed in Figure 2.1.

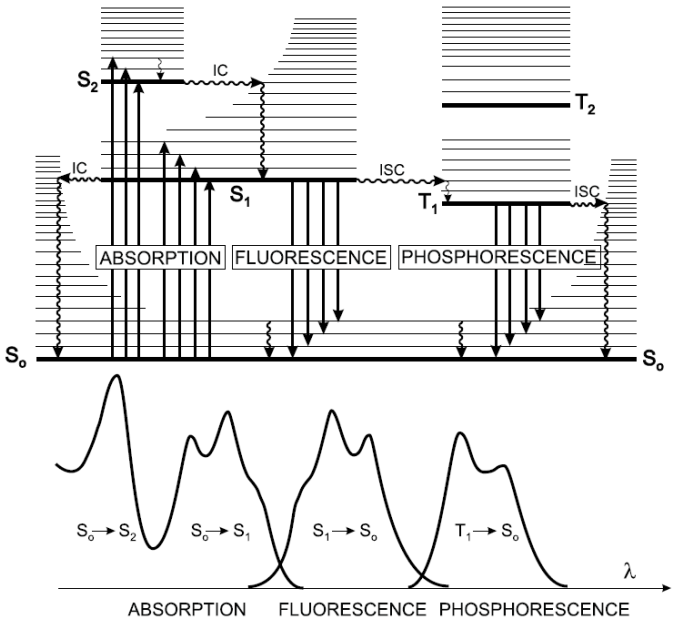

Figure 2.1: A Jablonski diagram (top) depicting the excitation and de-excitation pathways of a fluorescent molecule along with the fluorophore's corresponding absorption and emission spectra (bottom). Reproduced with permission from reference [7]. (Copyright 2001 John Wiley and Sons)

At room temperature, fluorophores reside in their lowest electronic state, the singlet ground state, typically denoted as S_0. When a fluorophore absorbs an incident photon, it undergoes an electronic transition to one of its excited singlet states S_n, where a larger value of n denotes a higher energy level. In Figure 2.1, these absorption transitions are illustrated as arrows extending from S_0 to one of the vibrational states of S_1 or S_2, where vibrational states are depicted as a series of thinner, parallel lines directly above each electronic state. For this absorption transition to occur, the energy of the incident photon must be equivalent to the energy difference between the final and initial states involved. Wavelengths that satisfy this condition compose the absorption

spectrum of the fluorophore. The relative strengths of these transitions are characterized by the fluorophore's molar extinction coefficient, $\varepsilon(\lambda)$, and depend primarily on the underlying structure of the molecule. Upon absorbing a photon, one of the molecule's electrons lying in the Highest Occupied Molecular Orbital (HOMO) is promoted to an available energy state in the Lowest Unoccupied Molecular Orbital. This transition leaves behind a hole in the HOMO, and together, this electron-hole pair is referred to as a molecular exciton.

After absorption, the fluorophore relaxes to the lowest vibrational state associated with its current excited electronic state. The molecule then randomly undergoes one of many parallel, competing de-excitation pathways. These paths are commonly split into two categories: radiative and non-radiative decay. Upon radiative decay, the fluorophore transitions from S_1 to one of the vibrational states of S_0, emitting a photon at a lower energy, or longer wavelength, than the photon it originally absorbed. These radiative transitions compose the fluorescence spectrum of the fluorophore and the likelihood of this transition is called the quantum yield, i.e. the probability of fluorescence. The red-shift between the absorption and fluorescence spectra is known as the Stokes shift. This parameter quantifies the amount of energy lost due to vibrational relaxations immediately following absorption. Close inspection of the absorption and fluorescence spectra in Figure 2.1 reveals that there is some spectral overlap between

these two distributions. At first, this seems to violate the conservation of energy, i.e. it implies that fluorophores can emit higher energy photons than they absorb; however, this overlap is the result of a small population of fluorophores residing in the higher vibrational states of S_0 at room temperature. These higher energy fluorophores require less energy to reach S_1, giving rise to the red tail of the absorption spectrum that overlaps with the fluorescence spectrum.

The second de-excitation category, non-radiative decay, encompasses any molecular transition that does not release a photon. The two most common forms of non-radiative decay are internal conversion and intersystem crossing (labeled as IC and ISC respectively, and represented as wavy arrows in Figure 2.1). During internal conversion, the excited fluorophore returns to its ground state through a series of vibrational relaxations. This is the dominant form of non-radiative decay. Intersystem crossing is a slightly more complicated de-excitation path in which the excited electron's spin changes and the molecule enters the triplet state, denoted by T_1 in Figure 2.1. This transition is technically forbidden by the selection rules of quantum mechanics, yet a phenomenon known as spin-orbit coupling allows the transition to proceed with a very low efficiency [7, 11]. Once in the triplet state, the fluorophore may either undergo intersystem crossing a second time to return to its ground state or it may emit a photon. This emission process, known as phosphorescence, releases lower energy photons than

those of the fluorescence spectrum. Phosphorescence can largely be ignored for fluorophores diffusing in an aqueous solution at room temperature, i.e. the standard operating environment for RET systems, since collisions between the solvent and the triplet state fluorophore usually force the molecule to return to its ground state. In fact, the triplet state altogether is often neglected due to the rarity of its formation; however, as we will see in Chapter 4, this state plays a dominant role in accessing additional molecular pathways that are useful for engineering more complex fluorophore-based systems.

Together, the rates of radiative and non-radiative decay, denoted as k_r and k_{nr} respectively, define the intrinsic lifetime of the fluorophore, τ_0, according to Equation 2.1.

$$\tau_0 = \frac{1}{k_r + k_{nr}} \qquad \text{Equation 2.1}$$

This parameter characterizes the amount of time the molecule spends in the excited state before decaying. When a population of fluorophores is excited simultaneously, the fluorophores spontaneously return to their ground state over time following an exponential probability density function of the form $e^{\frac{-t}{\tau_0}}$ [7]. Typical fluorescence lifetimes are on the order of 1-10 nanoseconds and heavily depend on the molecule as well as its microenvironment.

2.2 Resonance Energy Transfer

When an excited fluorophore is placed within close proximity of a separate, ground state fluorophore, the excited molecule may transfer its energy non-radiatively to its neighbor through a phenomenon known as Förster Resonance Energy Transfer. First formulated by Theodor Förster in 1946, RET is a weak, dipole-dipole coupling between two fluorophores spaced 1-10 nm apart [7, 12, 13]. As a resonant process, RET requires the donor's fluorescence transitions to be equal in energy to the acceptor's excitation transitions. In the wavelength domain, this implies that donor's emission spectrum must overlap with the acceptor's excitation spectrum.[1] Both of these concepts are illustrated in Figure 2.2. When RET occurs, the exciton in the donor recombines and a new exciton forms in the acceptor. Thus, RET is commonly described as the transfer of an exciton from one fluorophore to another.

[1] The excitation spectrum is the portion of the fluorophore's absorption spectrum that ultimately results in fluorescence. Although the terms are often used interchangeably, certain absorption transitions may never result in fluorescence and should therefore not be considered a part of the excitation spectrum.

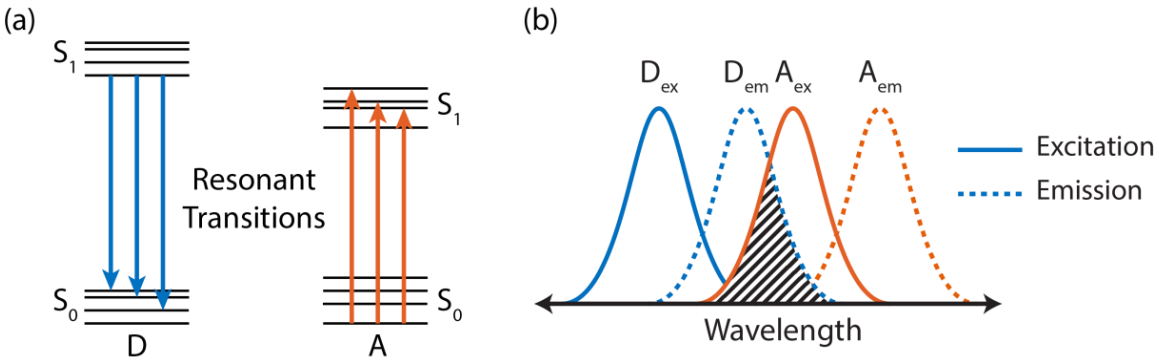

Figure 2.2: (a) A simplified energy diagram illustrating the resonant transitions between a donor (D) and an acceptor (A). (b) Resonant transitions can also be viewed as an overlap between the donor's emission spectrum and the acceptor's excitation spectrum, i.e. the shaded region between spectra.

The spectral overlap requirement, coupled with the Stokes shift of each fluorophore, forces RET to predominantly be a one-way transfer mechanism, much like a standard PN junction diode. RET can, however, occur between two instances of the same fluorophore due to the slight overlap of a fluorophore's excitation spectrum with its own emission spectrum. This process, known as homogeneous RET, is discussed further in Section 2.3.2 when it is applied to RET logic.

The compatibility of two fluorophores for undergoing RET is characterized by their Förster radius, R_0, a parameter specifying the distance at which the transfer efficiency is 50%. Typical values of R_0 range from 3-7 nm with larger values implying better energy coupling between the two molecules [14]. The Förster radius is determined by Equation 2.2 [15].

$$R_0^6 = \frac{9(\ln 10)\kappa^2 \Phi_D^0}{128\pi^5 N_A n^4} \int I_D(\lambda)\varepsilon_A(\lambda)\lambda^4 \, d\lambda \qquad \text{Equation 2.2}$$

The integral in this equation captures the overlap between the donor's normalized emission spectrum ($I_D(\lambda)$) and the acceptor's excitation spectrum (using its molar extinction coefficient, $\varepsilon_A(\lambda)$). Φ_D^0 represents the donor's quantum yield. N_A is Avogadro's number and n represents the average index of the refraction for the surrounding media within the spectral range involved (usually approximated as 4/3 for aqueous solutions). It should be noted that this surrounding media can also influence many of the fluorophores' other parameters aside from R_0, including their quantum yields, extinction coefficients, and emission spectra. Thus, to determine an accurate value of R_0, it is best to characterize the fluorophores in the appropriate solvent.

The remaining variable in Equation 2.2, κ^2, describes the relative orientations of the donor and acceptor fluorophores. This parameter takes on a value between 0 and 4, depending on the alignment between the donor's emission transition dipole moment and the acceptor's absorption transition dipole moment, which respectively define the polarization preferences of these molecules' absorption and emission transitions relative to their underlying structures. When the donor's emission dipole is perfectly aligned with the acceptor's absorption dipole, κ^2 is at its maximum value and transfer between the molecules is optimal. When these transition dipoles are perpendicular to one another, κ^2 is 0 and RET cannot take place. In solution, fluorophores often rotate, taking

on a distribution of orientations as a function of time [16]. Thus, when characterizing an ensemble of donor-acceptor pairs, the orientation factor is usually assumed to be 2/3, the average value for two freely rotating dipoles. A thorough derivation of both κ^2 and R_0 can be found in reference [15].

Equation 2.3 describes the transfer efficiency between two fluorophores, Φ_T, as a function of the distance separating the donor and the acceptor, r. As the distance increases, transfer efficiency drops dramatically.

$$\Phi_T = \frac{1}{1 + (r/R_0)^6} \qquad \text{Equation 2.3}$$

The relatively short values of R_0, coupled with the transfer efficiency's inverse sixth dependence on distance, imply that nanometer-scale control over intermolecular distances is essential to designing RET systems with both high accuracy and high precision. To achieve this control, we fabricate RET systems using DNA self-assembly, which allows us to position fluorophores relative to one another with sub-nanometer resolution. This fabrication strategy is described in Section 2.3.4.

The rate of energy transfer between fluorophores is governed by Equation 2.4. Similar to the transfer efficiency, this rate has an inverse sixth dependence on separation distance. It is also inversely related to the lifetime of the donor in the absence of the acceptor, τ_{D0}. Thus, shorter donor lifetimes lead to higher transfer rates. With standard fluorescence lifetimes on the order of 1-10 ns, the transfer rates for donor-acceptor pairs

separated by a distance of $0.5R_0$ range from 10^9 s^{-1} to 10^{10} s^{-1}. This provides a rough estimation of the speed at which RET can perform computation, e.g. assuming an operation takes less than 10 RET events, it can be completed in 1-10 nanoseconds.

$$k_T = \frac{1}{\tau_{D0}}\left(\frac{R_0}{r}\right)^6 \qquad \text{Equation 2.4}$$

Based on the governing principles described throughout this section, interactions between fluorophores, e.g. transfer efficiencies, transfer rates, can be controlled by simply designing the distance between the appropriate donor and acceptor fluorophores. We now explore how this concept can be applied to engineer groups of fluorescent molecules to perform computation at the molecular scale.

2.3 Resonance Energy Transfer Logic

Networks of fluorescent molecules can be arranged into spatial configurations that perform Boolean operations using RET. This form of computation is called RET logic and the molecular circuits involved are known as RET circuits (or more generally RET networks). In the following section, we explore this recently developed computing paradigm, beginning with the inputs, outputs, and methods of signal propagation. Afterwards, we provide examples of RET logic gates demonstrated thus far, discussing their operating principles and their current limitations. We conclude this section with a brief description of the bottom-up fabrication of RET logic using fully addressable, self-assembled DNA nanostructures.

2.3.1 Inputs and Outputs

RET circuits consist of two or more fluorophores deliberately positioned with respect to one another to control the transfer efficiencies between them. The external inputs and outputs to these circuits are absorbed and fluoresced photons respectively. Input photons are supplied by an external light source that directly excites designated input fluorophores. Since most useful computational systems require more than one input, RET circuits often contain more than one distinct input fluorophore, each independently addressed by a different excitation wavelength. It should be noted that the excitation spectra of these input fluorophores may have some overlap. When choosing the excitation wavelengths for these fluorophores, this overlapping region is avoided to retain independent addressability. Alternatively, this overlap can be leveraged to address multiple inputs with a single excitation source.

When an input fluorophore absorbs a photon, it generates a molecular exciton. This exciton then propagates through the network of fluorophores according to the engineered RET pathways until reaching a designated output fluorophore, conveying the result of the computation back to the user by fluorescing. RET circuits may have multiple output fluorophores, each fluorescing in a different region of the visible spectrum so that they can be independently observed. This output fluorescence is monitored by a nearby photodetector. When the signal rises above a pre-defined

threshold, the output is interpreted as a logical 1; otherwise, it is interpreted as a logical 0.

Figure 2.3 provides an example of an abstract RET logic device consisting of two input fluorophores (x_1 and x_2), two output fluorophores (o_1 and o_2), and an array of internal fluorophores for performing an arbitrary function. The two input fluorophores are independently excited at wavelengths λ_{I1} and λ_{I2}, and the two output fluorophores are independently monitored at wavelengths λ_{O1} and λ_{O2}.

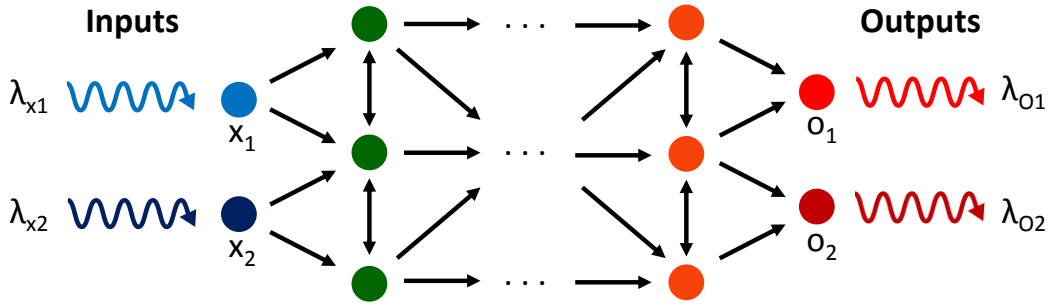

Figure 2.3: An abstract RET logic device with two input fluorophores (x_1 and x_2 excited at λ_{x1} and λ_{x2} respectively) and two output fluorophores (o_1 and o_2 observed at λ_{O1} and λ_{O2} respectively).

The visualization provided by Figure 2.3 is called an Exciton Flow Diagram (EFD). EFDs will be used throughout this dissertation to describe the operating principles of RET networks without focusing on the details of their implementation, e.g. the specific fluorophores chosen, exact coordinates of each fluorophore, etc. Distinct fluorophores in an EFD are represented by different colored circles corresponding to the relative portion of the visible spectrum consumed by that fluorophore. Note that the

input fluorophores in Figure 2.3 are blue-shifted from the output fluorophores. This is common in RET circuits since excitons must begin at a donor to progress through a RET network, and RET donors are generally blue-shifted from their acceptors due to the Stokes shift. RET pathways in EFDs are depicted as arrows extending from donors to potential acceptors. Thicker line weights denote higher transfer efficiencies. Although the abstract network in Figure 2.3 uses the same efficiency between all fluorophores, some RET networks will require a mixture of transfer efficiencies to perform a specific Boolean operation.

2.3.2 Wires

Individual RET circuit components are connected by chains of donor-acceptor pairs that form excitonic wires. Figure 2.4 illustrates a heterogeneous RET (hetero-RET) wire, which uses a linear cascade of distinct fluorophores to transport excitons. The blue fluorophore acts as the input to the wire. Excitons can be supplied to this input by either an external light source (as depicted in Figure 2.4) or an upstream RET donor, i.e. the output of an upstream RET device. Hetero-RET wires provide unidirectional exciton transfer; however, they quickly consume the visible spectrum available for building RET systems since the number of unique fluorophores scales with the wire length. Despite this drawback, a variety of hetero-RET wires have been experimentally demonstrated consisting of four or more unique fluorophores [17-19].

Figure 2.4: A hetero-RET wire composed of four distinct fluorophores.

The simple EFD of the hetero-RET wire provides an opportunity to discuss both types of signal loss that currently limit the size and complexity of RET systems. First, the end-to-end transfer efficiency of a RET network decreases exponentially with length, i.e. the number of fluorophores from input to output. For example, the transfer efficiency between each fluorophore in the hetero-RET wire is ideally 100%, such that every exciton entering the wire at the input exits the wire at the output. In reality, however, these transfer efficiencies never reach unity due to a variety of nonidealities, e.g. hindered rotations of fluorophores, unexpected quenching pathways due to the microenvironment, etc. If every donor-acceptor pair in the wire has a 90% transfer efficiency, the end-to-end efficiency is only 0.9^3, or ~73%. The remaining 27% of the excitons never reach the output simply because they are fluoresced or suppressed by internal conversion while traversing the wire. All RET systems are subject to this exciton loss, but, as we will see in Chapter 4, RET systems can be designed that decouple this loss from the overall length of a RET circuit.

The hetero-RET wire in Figure 2.4 also clearly demonstrates the energy loss experienced by RET networks. As excitons move through the wire from input to output, they are red-shifted. As mentioned in Section 2.1, this loss of energy stems from the

vibrational relaxation of each fluorophore, which forces an acceptor to have a longer wavelength excitation spectrum than its donor. Accordingly, the hetero-RET wire cannot supply excitons to any circuit component with an input fluorophore that is blue-shifted from the wire's output fluorophore, which even rules out an identical copy of the wire itself. In general, energy loss prevents independently designed RET circuit components from being cascaded. It also precludes the use of feedback since downstream outputs are incompatible with upstream RET devices.

Recall from Section 2.2 that different copies of the same fluorophore may undergo RET with one another due to the inherent overlap of their own excitation and emission spectra. This process is known as homogeneous RET (homo-RET), or energy migration (EM). Homo-RET can be exploited to build wires that conserve spectral content as a function of length by using multiple instances of the same fluorophore, as shown in Figure 2.5. Unlike hetero-RET wires, in which excitons primarily travel in one direction, excitons in a homo-RET wire are free to move both up and downstream due to the bidirectional nature of this transfer. Directionality can be induced, however, by supplying a constant stream of excitons at the input of the wire such that the occupancy of upstream fluorophores forces excitons to move towards the output. A wide variety of homo-RET wires have been experimentally demonstrated, some capable of transporting excitons over 25 nm in distance [20-24].

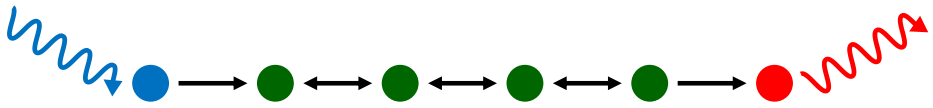

Figure 2.5: A homo-RET wire composed of only three distinct fluorophores.

Although homo-RET can decouple the energy loss of a RET wire from its overall length, it does not completely resolve the energy loss in RET circuits. Most RET devices require one or more unique fluorophores in order to perform their intended operation. For instance, the input and output fluorophores of every RET device must remain unique so that they can be independently addressed and observed. Additionally, some RET devices may require unidirectional transfer for certain RET pathways, which can only be guaranteed by hetero-RET. When possible, throughout this dissertation we will utilize homo-RET to design new logic devices that do not suffer from increasing energy loss as a function of length (Chapter 4). For cases in which homo-RET is not applicable, we have developed a device described in Chapter 3 that converts low energy excitons into high energy excitons.

2.3.3 Logic Gates

When properly designed, certain RET networks can perform Boolean operations similar to those of conventional digital logic. To demonstrate these principles, Figure 2.6a illustrates the EFD for an OR gate previously fabricated in our lab [25]. The OR gate consists of three fluorophores: two spectrally distinct input donors, x_1 and x_2, and a

single RET acceptor, O, which acts as the gate's output. Exciting either input independently results in RET and subsequently output fluorescence. Exciting both inputs simultaneously results in roughly double the output emission (assuming that the transfer efficiencies from each donor to the acceptor are roughly equal). Figure 2.6b plots this output fluorescence for each of the four input conditions.

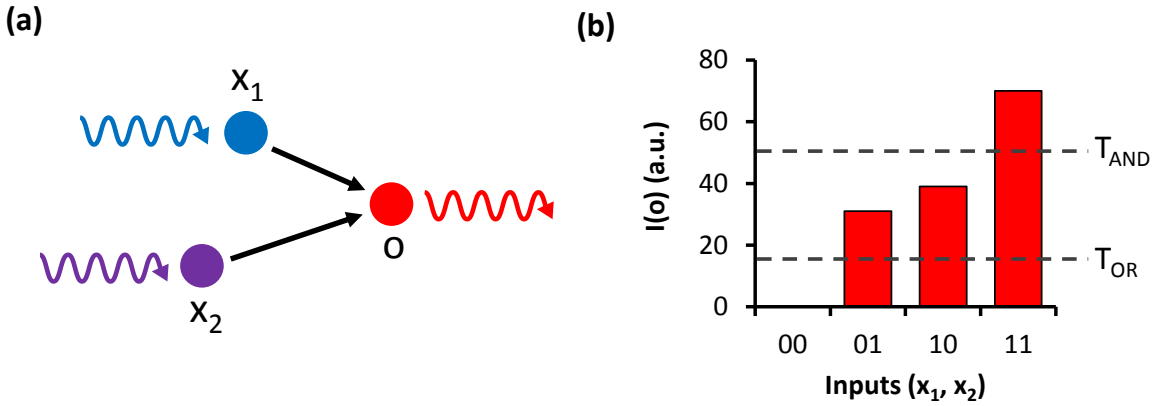

Figure 2.6: (a) A two-input OR/AND gate. (b) Output fluorescence (I(o)) from the logic gate for each combination of inputs. A low output threshold, T_{OR}, configures the device to behave as an OR gate. A high output threshold, T_{AND}, configures the device as an AND gate.

To assign OR functionality to this logic gate, an output threshold, T_{OR}, is set below the fluorescence value provided by each independent input. Thus, if neither input is excited, i.e. $x_1=0$ and $x_2=0$, the output signal is below the 0-1 threshold and evaluated as a logical 0. Every other input combination results in an output fluorescence signal that exceeds T_{OR}, and is therefore evaluated as a logical 1. Interestingly, this same RET network can be reconfigured to perform an AND operation by raising the 0-1 threshold

above the individual input contributions such that both inputs must be true to produce a logical 1. This second threshold is represented as T_{AND} in Figure 2.6b.

Current methods of RET logic design (like the AND/OR device described above) suffer from a few important limitations. First, there is no notion of inversion. A logic gate has yet to be demonstrated that produces output fluorescence based on the absence of input excitation. This lack of inversion can be circumvented by encoding logical 1s and 0s as separate inputs [26]. Known as dual-rail encoding, this solution allows logical 0s to propagate through RET networks in the same fashion as logical 1s, i.e. as the presence of excitons. This technique, however, requires the design, fabrication, and evaluation of duplicate sets of hardware for each output function, F: one that encodes F and a second that encodes $\bar{F}$.

In addition to this lack of inversion, RET logic gates like the one shown in Figure 2.6 are limited to producing a linear response with respect to the input conditions, i.e. the output is always a partial sum of the inputs applied during evaluation. This property restricts RET logic gates to only performing linearly separable Boolean operations in which the monotonically increasing output fluorescence can be thresholded to produce the correct truth table. For instance, AND and OR can both be implemented since they output a logical 1 when one or more inputs are true. XOR and NAND, however, cannot be implemented since they must produce a logical 0 when all

inputs are true. Furthermore, this linearity implies that logic gates may produce significant output fluorescence even when the output is evaluated as a logical 0, thereby leading to the incorrect evaluation of downstream logic when integrated into a larger system. To avoid this issue, logic gates should ideally have tunable nonlinear responses in which the output for a logical 1 is much greater than the output for a logical 0.

To introduce nonlinearity into RET logic devices, transfer efficiencies must be dynamically modulated based on the excitation conditions so that certain RET pathways can be either enhanced or removed. One such method of modulation is excited singlet saturation [27]. Most fluorophores cannot absorb more than one quantum of energy from the same visible far-field source or RET donor simply due to the energy spacing of their excited singlet states. Thus, if a fluorophore is consistently excited, or saturated, it cannot accept additional excitons from surrounding fluorophores.

Leveraging this concept, Thusu and Dwyer recently developed the Closed Diffusive Exciton Valve (C-DEV) [28]. At a high level, the C-DEV modulates the diffusion of excitons through a homo-RET wire based on a separate input, similar to the way the channel in a MOSFET is modulated by V_{GS}. As illustrated by the EFDs in Figure 2.7, the C-DEV is composed of four unique fluorophores: a source, mediator, drain, and gate. The source and the drain are connected by a channel of mediator fluorophores that form a homo-RET wire. Each of these mediators is accompanied by a gate fluorophore

that acts as an acceptor. When the source is excited, excitons travel into the channel and are stolen by the gate fluorophores as they diffuse towards the drain. As a result, the output fluorescence from the drain is low. This is called the "closed" state of the C-DEV (Figure 2.7a). When the gate fluorophores are saturated by continual excitation, they are temporarily turned off, thereby removing their exciton sinking pathways. Excitons can then diffuse towards the drain unhindered, resulting in higher output fluorescence. This is called the "open" state of the C-DEV (Figure 2.7b).

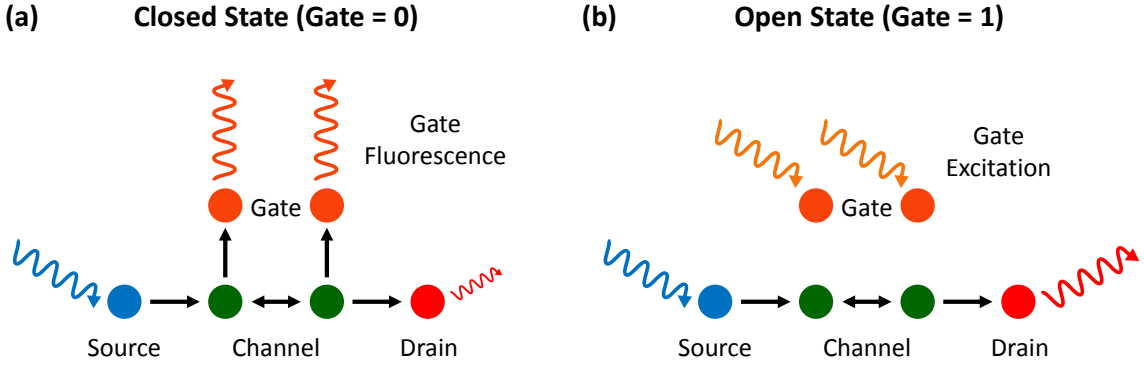

Figure 2.7: EFDs for the closed and open states of the C-DEV. (a) In the closed state, excitons in the channel are stolen by the gate fluorophores, resulting in low drain fluorescence. (b) In the open state, the gate fluorophores are saturated and the drain fluorescence increases.

Drain fluorescence from the C-DEV increases nonlinearly as a function of the number of saturated gate fluorophores [28]. While the EFD above uses only two mediator-gate fluorophore pairs, additional pairs may be placed between the source and drain to further increase the fluorescence ratio from the open and closed states, i.e. the on/off ratio. In practice, full saturation of a C-DEV with many mediator-gate pairs has

proven difficult, primarily due to the nanosecond lifetimes of florescent singlet states that in turn require very high excitation intensities. The first experimental demonstration of a C-DEV used four mediator-gate pairs and resulted in a maximum on/off ratio of 2.19. A more recent implementation of the C-DEV, using three mediators and two gate fluorophores, drastically improved upon this result, demonstrating an on/off ratio of 31.3 when saturated with a high power laser diode [29].

A device complementary to the C-DEV, a normally Open Diffusive Exciton Valve (O-DEV), has yet to be demonstrated. If possible, the O-DEV can introduce inversion to RET logic, producing high output fluorescence in the absence of gate excitation and low output fluorescence in the presence of gate excitation. In Chapter 4, we explore a new method for dynamically modulating RET networks, which enables such a structure and allows us to build a variety of new logic gates with nonlinear properties similar to the C-DEV.

Fabrication of the RET devices described in this section require fluorophores to be arranged with sub-nanometer resolution. We now describe one method for organizing these molecules into the desired arrangements using DNA as a structural material. This molecular assembly mechanism is particularly well-suited for RET circuit fabrication given the chemical compatibility of DNA and fluorescent molecules, and the ability of individual DNA strands to self-assemble into predefined nanostructures.

2.3.4 Fabrication by DNA Self-Assembly

Silicon-based computers have historically been fabricated using top-down methods. The common feature of a top-down process is a continuous reduction in the characteristic length scale of material structure from the macroscale to the molecular scale [30]. Standard integrated circuit fabrication begins with a silicon substrate upon which various layers of materials are deposited or removed to fabricate computational devices. As device sizes approach the few-atom limit, however, difficulties in structural and compositional control arise. To achieve the necessary resolution and control for building RET systems, these circuits are instead fabricated from the bottom-up using DNA self-assembly. A set of single-stranded DNA (ssDNA) sequences are designed such that when mixed together, the strands assemble into a rigid, complex nanostructure according to the strict Watson−Crick binding rules of DNA, illustrated in Figure 2.8 (i.e., adenine (A) binds to thymine (T); cytosine (C) binds to guanine (G)). This mechanism is considered programmable since the user has control over the formation of the target nanostructure through careful design of the DNA sequences. DNA self-assembly has been leveraged to build a variety of two and three dimensional objects, and over the last decade, its use has seen exponential growth largely driven by continuously decreasing DNA synthesis costs and higher throughput fabrication [31-36]. To build an integrated molecular system using this technology, individual molecules are chemically attached to

specific locations along the DNA strands before assembly. The physical self-assembly process then positions these molecules relative to one another to enable the desired interactions. Most attachment chemistries target individual DNA bases or the regions between them, providing a ~0.34 nm resolution based on the nucleotide spacing in a standard B-form DNA double helix (Figure 2.8) [37].

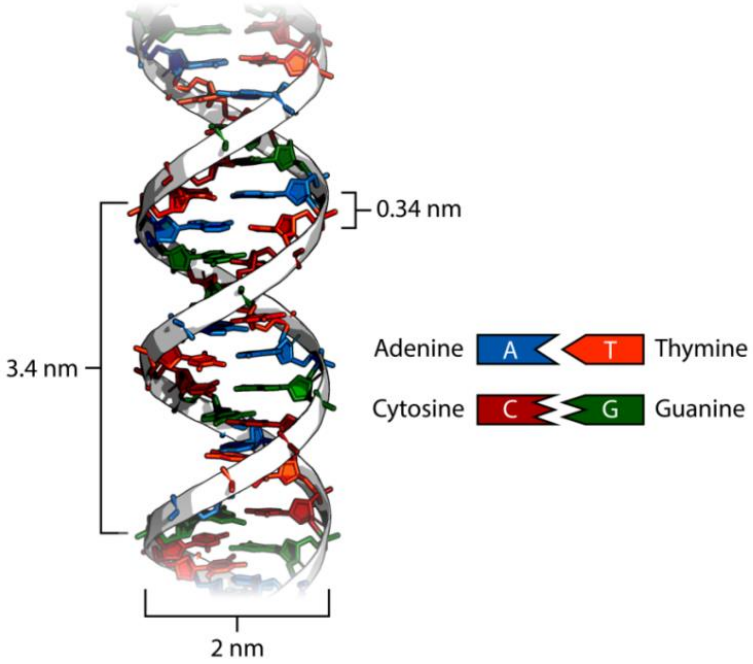

Figure 2.8: A standard (B-form) DNA double helix (generated by 3D-DART [38]). The distance between bases is approximately 0.34 nm. The width of the helix is 2 nm. A full helical twist occurs between the 10th and 11th base pairs. The four bases follow strict binding rules: A binds to T and C binds to G.

It is well established in computer science and engineering that real, practical computational systems require a large degree of complexity and aperiodicity. To achieve this, complex DNA nanostructures can be hierarchically assembled from smaller motifs.

By including short ssDNA overhangs, or sticky-ends, at the edges of a motif, motifs can be programmed to bind to one another and form complicated and dense patterns. For example, the cross motif, or tile, in Figure 2.9a, originally designed by Yan et al., is composed of nine strands: one core, four shells, and four sticky-ended arms [39]. Sixteen motifs were designed to form a 4x4 grid (Figure 2.9b), which can further assemble with other grids to fabricate larger macromolecules [40].

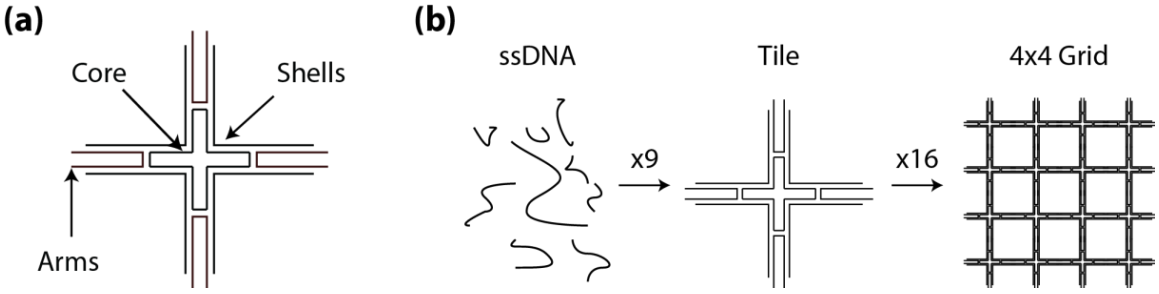

Figure 2.9: (a) A DNA cross motif. (b) A hierarchical assembly strategy for creating 4x4 DNA grids.

An ideal nanostructure for assembling RET logic must also offer full molecular addressability to allow for the placement of fluorophores at any location. One method for achieving this is to assign a unique sequence to each DNA strand so that its final position in the resulting structure is well-defined. This solution, however, limits the size of the DNA nanostructure due to the finite number of orthogonal sequences available. Instead, hierarchical assembly techniques can be employed to retain full addressability of the resulting nanostructures while allowing certain sequences to be reused [41]. In the case of the 4x4 grids, each cross motif can be assembled in a separate vial before being

mixed to form the grid. The core and shell strands, which are hybridized during the cross assembly step, can then be reused in all 16 motifs.

Using the fully addressable and hierarchically assembled DNA grid, the fabrication of an arbitrary RET circuit is relatively straightforward. A target network is first simulated to determine the optimal transfer efficiencies for providing the desired functionality. Afterwards, this abstract network is translated to a set of commercially available fluorophores with well-defined inter-molecular distances. The designer then chooses positions on the DNA grid that best approximate these ideal distances. Fluorophores are conjugated to these locations and the fluorophore-labeled strands are purified to remove waste products, excess fluorophores, and unlabeled strands. Individual tiles are assembled by mixing the labeled DNA strands with the remaining unmodified strands composing the tile. These samples are then annealed by raising the temperature to 96°C and cooling it back down to 4°C over the course of four hours [30]. The final grid is assembled by mixing individual tiles at room temperature and cooling them back down to 4°C. These annealing procedures help prevent the formation of structural defects that might arise during assembly [42, 43]. Based on this hierarchical

assembly procedure, we can currently fabricate 160 nm by 160 nm nanostructures for less than ~10^{-9} pennies per structure at a rate of ~10^{12} structures per hour.[2]

2.4 Summary

DNA self-assembly provides a strategy for fabricating RET networks, thereby enabling RET logic as a viable route for creating integrated molecular circuits. By properly engineering the transfer efficiencies between fluorophores, RET networks can designed to perform Boolean operations similar to standard digital systems. Although a variety of basic RET devices have been experimentally demonstrated, current methods of RET logic design are subject to a number of limitations preventing the construction of large-scale systems. The remainder of this dissertation is dedicated to addressing these challenges starting with a device that restores the energy loss in RET systems.

---

[2] This cost estimate assumes the following:

- 64 separate 1 μM tile samples are annealed in parallel, each with a sample volume of 60 μL
- Each tile costs ~10^{-11} pennies per tile (based on synthesis cost and yield estimates from Integrated DNA Technologies)
- Total assembly time is 8 hours (4 hours for tile assembly, 4 hours for grid assembly)

3. The Upconverting Nanoparticle RET Relay

As excitons move through RET networks, they lose energy due to the vibrational relaxation of each fluorophore. This loss makes it difficult to cascade RET networks or build systems with feedback. To remedy this loss, we have developed a device called the RET relay, which uses an inorganic nanoparticle to convert multiple low energy excitons into a single high energy exciton.

We begin this chapter with a brief review of the energy loss in RET circuits. We then discuss various upconversion mechanisms for restoring this energy, focusing on why certain methods, such as the use of upconverting nanoparticles, are more suitable for integration into RET circuits than others. Afterwards, we describe the design and assembly of the RET relay. We experimentally verify that the individual energy transfer mechanisms necessary for energy restoration work as proposed. We then show that the entire nanoassembly successfully converts low energy excitons into high energy excitons.

3.1 Energy Loss in RET Networks

Immediately after entering the excited state, a fluorophore undergoes a series of vibrational relaxations that force its emission spectrum to be red-shifted from its excitation spectrum. For fluorophores involved in a hetero-RET cascade, this red-shift implies that the excitation spectrum of every acceptor must be lower in energy than its

donor. Accordingly, as excitons traverse a RET cascade from input to output, they lose energy with each step.

Without a way to restore this energy, RET networks suffer from a variety of scaling and topological limitations. Networks using hetero-RET cannot take advantage of feedback since internal signals are not compatible with upstream portions of the network. By definition, this rules out the use of sequential circuits in RET logic (both synchronous and asynchronous) since they require a feedback path from output to input. In addition to this lack of feedback, independently designed RET networks are often incompatible with one another simply because the output of one network is usually too low in energy to act as the input to a subsequent network. This makes it difficult to create a library of cascadable logic components for building more complex systems. In certain cases, it may be possible to design an entire set of cascaded logic operations as a single RET network, ensuring that the design does not violate the required downhill energy flow; however, such solutions cannot be scaled to fabricate arbitrarily large circuits. These limitations prompted us to engineer a device that restores the energy of excitons as they transition from one RET network to another.

3.2 Upconversion Mechanisms

To achieve this energy restoration, we explored the use of upconversion. Upconversion processes combine many low energy inputs to form high energy outputs.

The most commonly utilized upconversion mechanisms rely entirely on far-field interactions. For example, two-photon excitation combines the energy of two simultaneously absorbed photons to elevate a molecule to its excited state [44]. Such, far-field mechanisms, however, are unfit for restoring energy in RET networks since suitable mechanisms must acquire at least one of the low energy quanta from near-field interactions with an upstream RET donor. Two lesser known, yet compatible, mechanisms called transfer-induced double-quantum excitation (TIDQE) and anti-Stokes electronic Raman-induced transfer (ASERIT) were proposed by Bradshaw and Andrews while analyzing multi-quanta transfer processes in donor-acceptor pairs [45]. Both of these mechanisms use a lower energy donor to excite a higher energy acceptor. In the case of ASERIT, a single donor fluorophore absorbs multiple excitons or photons to reach a virtual state that is higher in energy than its first real excited singlet state. From this highly excited transient state, the donor transfers a single energy quantum to the higher energy acceptor. In TIDQE, the energies of one exciton and one photon are combined in a manner similar to two-photon excitation to elevate an accepting molecule to an excited state. While both of these mechanisms offer a potential energy restoration solution for RET circuits, neither mechanism has been explored experimentally and, as the authors note, the required electronic transitions may even be quantum mechanically forbidden. Thus, while developing our energy restoring device, we focused our

attention on the more established and compatible upconversion processes found in upconverting nanoparticles.

Over the last decade, UCNPs have garnered significant attention due to their high upconversion efficiency and low excitation power requirements [9]. At a high level, UCNPs convert many low energy photons into a single, or a few, high energy photons. The most efficient UCNPs to date consist of a hexagonal $NaYF_4$ host lattice doped with two different lanthanide ions, known as the sensitizer and the activator [46]. The energy diagram for one particular sensitizer-activator pair is shown in Figure 3.1. The sensitizer lanthanide, commonly chosen as Yb^{3+}, strongly absorbs NIR excitation centered around 980 nm. Once in an excited state, Yb^{3+} donates this energy to a neighboring activator ion, which has a ladder-like set of electronic transitions that are resonant with the sensitizer. After transferring this energy, the sensitizer decays to ground while the activator remains excited for hundreds of microseconds. This provides time for the sensitizer to absorb another 980 nm photon and repeat this entire process. Thus, sequential energy transfer events from the sensitizer to the activator raise the activator to a highly excited state, from which it can visibly fluoresce (typically referred to more broadly as photoluminescence (PL)). The quantum yield of this upconversion process heavily depends on the dopant concentrations (typically 20 mol% for the sensitizer and <2 mol% for the activator) and the size of the particles, but is generally less than 1% [9, 47].

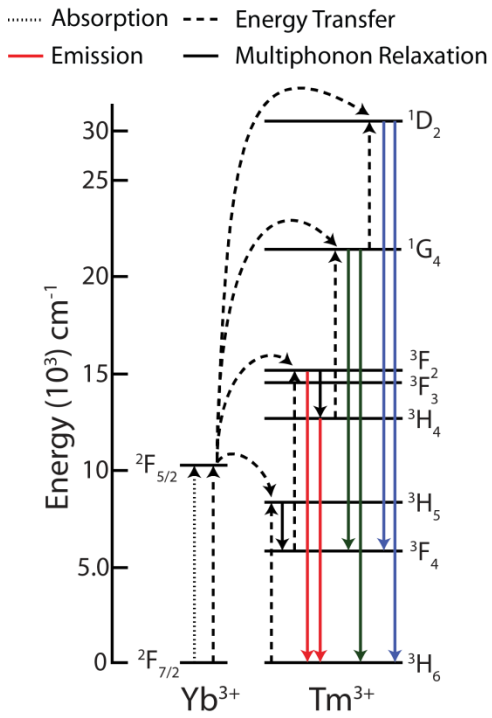

Figure 3.1: Upconversion pathways in $NaYF_4$:Yb/Tm nanoparticles, traced from reference [9] using Russell-Saunders notation. Photoluminescent transitions are broken into color coded groups to compare their relative wavelengths.

Upconverting nanoparticles have been used extensively as RET donors to both organic chromophores and quantum dots due to their anti-Stokes emission that favorably separates the excitation and observation bands [48-52]. In addition, their NIR absorption allows for deeper penetration into biological tissues, making them suitable RET donors for diagnostic and therapeutic applications. Very little work, however, has utilized UCNPs as RET acceptors [53, 54]. These few examples though provide sufficient evidence that UCNPs can act as RET acceptors and that this dye-sensitized emission is efficient enough to observe experimentally.

The evidence that UCNPs are RET compatible inspired us to design a RET-based device that exploits these inorganic nanoparticles to restore energy loss in RET systems. If RET networks can be brought into close proximity with the ions of the UCNP, the output fluorophores of these networks can donate low energy excitons to the lanthanides via RET. These dopants can then convert multiple low energy excitons into a single high energy exciton that is relayed back to input fluorophores of the subsequent network. To demonstrate this underlying process, we designed and fabricated a proof-of-principle device called the UCNP RET relay, which uses the UCNP as a bridge to transfer energy from a NIR excited fluorophore to a visibly excited fluorophore. The NIR fluorophore represents the output of a potential upstream RET network, while the visible fluorophore represents the input of a potential downstream RET network.

3.3 RET Relay Design and Fabrication

The UCNP RET relay is composed of two organic fluorophores, Cyto 840 and ATTO 488, as well as a single $NaYF_4$ crystal doped with Yb^{3+} and Tm^{3+}. Figure 3.2 shows an overview of this device as well as the energy diagram for its corresponding transitions. Operation begins with the excitation of Cyto 840 at 810 nm. This avoids direct excitation of the other two relay components due to their low extinction coefficients at this wavelength. Having significant emission overlap with the UCNP's 980 nm excitation, Cyto 840 non-radiatively transfers its low energy excitons to the

nanoparticle's dopants. After three or more transfer events, the Tm^{3+} dopants reach highly excited states ($^1G_4$ and $^1D_2$) that have emission pathways resonant with ATTO 488's first excited singlet. Transfer then proceeds from the excited ions to ATTO 488. When designing the relay, Cyto 840 was chosen as the input chromophore for its long emission tail extending past 1000 nm. Tm^{3+} was chosen as the activator ion because it offers the bluest emission spectrum provided by UCNPs, and ATTO 488 was chosen as the output for its significant excitation overlap with the $NaYF_4$:Yb/Tm emission spectrum and its high quantum yield of 80% [14].

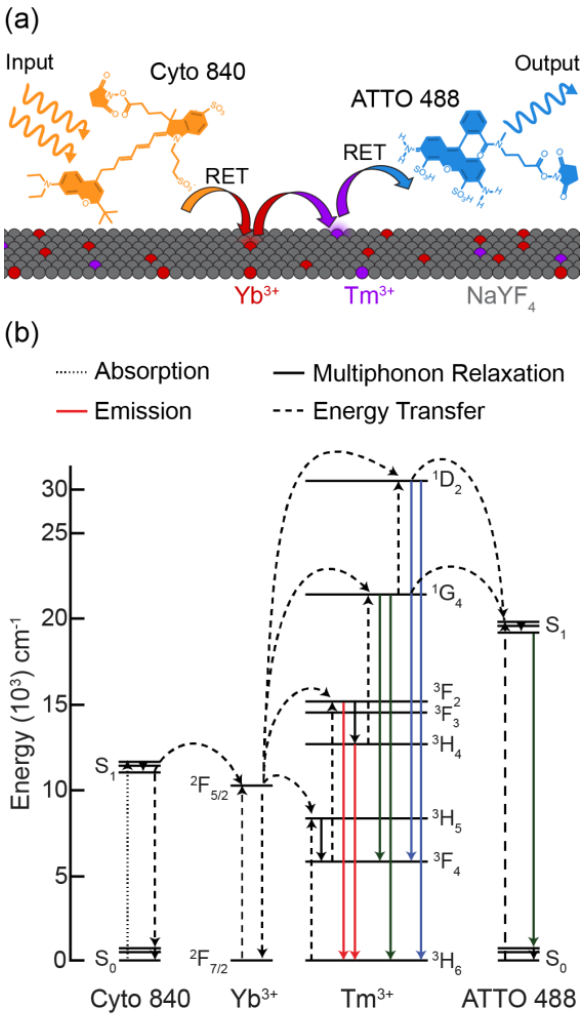

Figure 3.2: (a) Composition and operation of the RET relay. (b) Energy diagram depicting transfer pathways through the RET relay. Singlet states (S_0 and S_1) for the organic chromophores are based on the published excitation and emission maxima [14]. Their associated vibrational levels are conveyed as a closely packed set of three lines for visualization purposes only.

To fabricate the RET relay, fluorophores were directly adsorbed to the UCNPs while in solution. Although adsorption does not guarantee a well-ordered assembly of the device's components, covalent attachment methods found in the literature generally

target the particle's ligands rather than the dopants of the UCNP and therefore offer a similar level of disorganization regarding distances between the conjugated molecules and ions while simultaneously requiring more assembly steps [55, 56]. This adsorption procedure uses NHS ester modified versions of ATTO 488 and Cyto 840 suspended in dimethyl sulfoxide (DMSO) at high concentrations (10 μM – 3 mM) and UCNPs capped with oleic acid at a stock concentration of 10 mg/mL in chloroform. Assembly begins by adding 0.5 μL of each fluorophore stock to 25 μL of UCNP stock in a 300 μL RSA glass insert. The insert is placed inside an RSA glass autosampler vial, sealed with Parafilm, and vortexed for 10 seconds to ensure initial mixing of the two solvents. The sample is then sonicated for 2 hours at room temperature to further facilitate mixing and preemptively avoid aggregation. Afterwards, the volume is raised to a measurable level and the sample is sonicated for an additional 15 minutes to adequately mix in the additional solvent. Some of the experiments described in the following sections require negative controls in which certain relay components are omitted. In these cases, the omitted component is replaced with its respective solvent to keep the ratios of solvents consistent across all samples. Additional details regarding this assembly process and the parameters used for data collection can be found in Appendix A.1.1.

Successful adsorption of the fluorophores to the particles was confirmed in a few ways. The simplest method was colorimetric comparison of centrifuged free dye,

UCNPs, and UCNP-dye complexes. As shown in Figure 3.3, when mixed with either fluorophore, pelleted UCNPs have a colored tint that matches the color of the respective dye in solution. The UCNP-Cyto 840 pellet appears brownish in color, similar to free Cyto 840 suspended in chloroform while the UCNP-ATTO488 pellet appears reddish in color. Particles pelleted without adsorbed dye are naturally translucent, and each fluorophore by itself in chloroform does not precipitate or form a pellet when centrifuged at these concentrations.

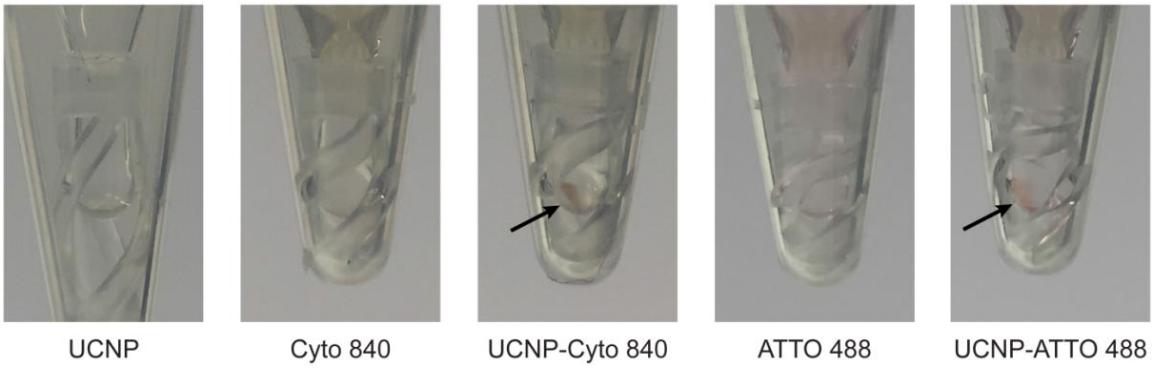

Figure 3.3: Images of pelleted UCNP-dye complexes after centrifuging at 10,000 rpm for 15 minutes. The only visible pellets (marked with arrows) are those containing both UCNPs and fluorophores.

In addition to these qualitative observations of dye-particle localization, we used time-resolved fluorescence anisotropy, which allows us to compare the rotational hindrance of free dye to that of adsorbed dye. Shown in Figure 3.4, without the UCNPs present, ATTO 488's anisotropy rapidly decays to zero, indicating that the free dye rotates without interference. When added to the particle, however, ATTO 488 exhibits a

long fluorescence anisotropy decay that remains nearly unchanged at the nanosecond timescale. This result strongly suggests that ATTO 488 is localized to the particle, as adsorption should introduce a much slower rotational component to the fluorescence anisotropy due to the difference in size between the particle and the dye.

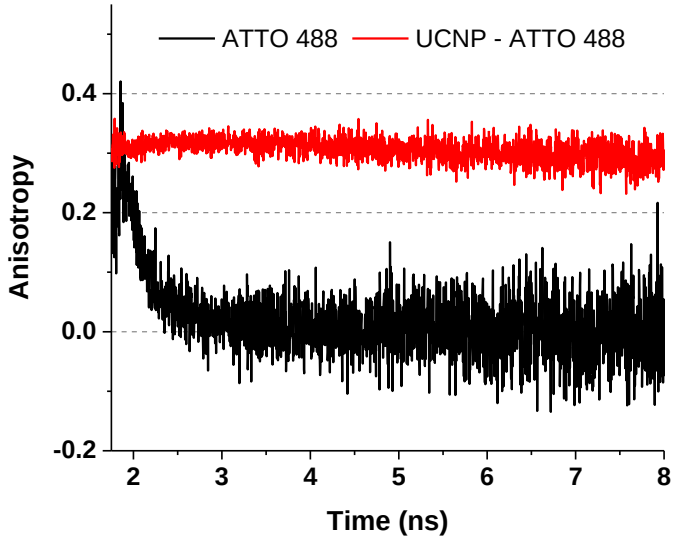

Figure 3.4: Time-resolved fluorescence anisotropy of free ATTO 488 and UCNP-ATTO 488 complexes. The quick decay of ATTO 488's fluorescence anisotropy indicates that it rotates unhindered, while the long decay of UCNP-ATTO 488 complexes suggests that the dye is adsorbed to the slowly rotating particle.

While taking these time-resolved measurements, we also unexpectedly found that the photon counts from the adsorbed dye were ten-fold higher than that of free dye (Figure 3.5). Further work is necessary to determine whether this is a fluorescent enhancement effect or if the free dye is more heavily quenched than the adsorbed dye due to full chloroform solvation.

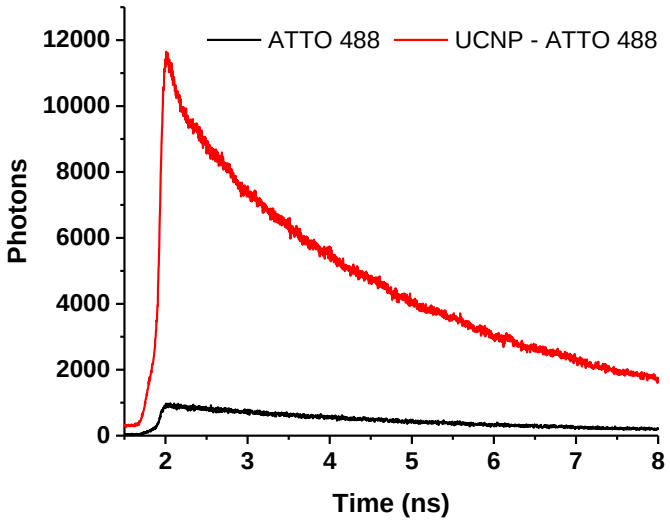

Figure 3.5: Time-correlated single photon counting (TCSPC) measurements of the fluorescence from free ATTO 488 and adsorbed ATTO 488, both at the same concentration. Adsorbed dye exhibits more than a ten-fold increase in peak counts.

3.4 UCNP-Cyto 840 Characterization

Once we established an assembly mechanism, each half of the relay, i.e., UCNP-Cyto 840 (first half) and UCNP-ATTO 488 (second half), was fabricated and tested independently. To demonstrate a fully functioning first half, the PL from a sample of UCNP-Cyto 840 was compared to two negative controls consisting of the individual constituents at the same concentrations (Figure 3.6). When excited at 810 nm, neither of the controls shows signs of emission. This ensures that the UCNPs are not directly excited at 810 nm and that Cyto 840's fluorescence does not bleed into the visible spectrum. Unlike the controls, UCNP-Cyto 840 complexes exhibit many of the emission

peaks typical of standard $NaYF_4$:Yb/Tm particles. This result confirms that the adsorbed Cyto 840 can transfer its energy to the particle's dopants and that this transfer is efficient enough to push Tm^{3+} to highly excited states.

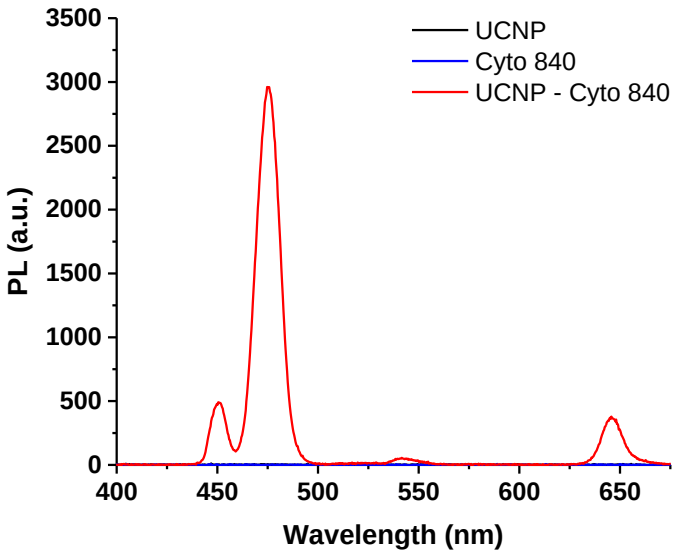

Figure 3.6: PL measurements of the first half of the relay and its individual components when excited at 810 nm. Emission from the UCNP-Cyto 840 complex confirms proper energy transfer through the first half of the relay.

Figure 3.7 compares the normalized emission spectra of UCNP-Cyto 840 when excited at 980 nm through the UCNP and at 810 nm through Cyto 840. Juxtaposition of these spectra reveals that the Tm^{3+} emission wavelengths remain the same, independent of the excitation source; however, the relative intensities of these emission lines change. Most notably, the 450 nm peak decreases by roughly 80%. This wavelength corresponds to the $^1D_2 \rightarrow {}^3F_4$ transition and requires at least four excitons from Cyto 840 [57]. The $^1G_4 \rightarrow {}^3H_6$ transition at 475 nm, however, only needs three transfer events and remains as the

most prominent peak. In addition, there are a few minor, but important, changes in the 500–600 nm emission region. When excited at 810 nm, the UCNP's 510 nm peak decreases almost entirely and a slight emission peak at 520 nm arises. These changes will be seen again when analyzing the full relay. Given that the excitation power density influences UCNP emission, this spectral change likely originates from the exciton flux supplied by Cyto 840 being lower than the 980 nm photon flux directly exciting the particle [58, 59]. This conclusion is simultaneously supported by the need for longer integration times and higher laser powers when exciting the particles at 810 nm (see Appendix A.1.1 for details). Despite these spectral differences, the altered emission from the first half of the relay is still sufficient for exciting downstream ATTO 488 in the full relay, as the 475 nm peak has the largest overlap with ATTO 488's excitation spectrum.

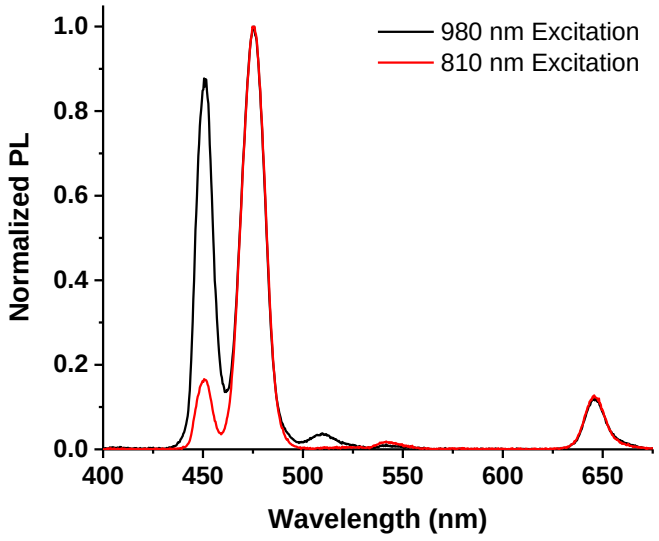

Figure 3.7: Normalized emission spectra of UCNP-Cyto 840 complexes when excited at 980 nm and 810 nm.

To determine the optimal reaction coordinates for Cyto 840 adsorption, we varied the fluorophore assembly concentration while keeping the UCNP concentration constant. For each sample, we measured the emission spectrum of the complex when excited at 980 nm and at 810 nm. We then integrated the UCNP's 475 nm peak for each excitation case and examined these values, denoted by PL_{810} and PL_{980}, as a function of the dye concentration. PL_{810} evaluates the performance of the first half of the relay since a higher value implies better energy transfer from Cyto 840 to the UCNP. PL_{980}, on the other hand, reveals any secondary effects Cyto 840 has on the particle's emission when directly excited.

The PL_{810} results are summarized in Figure 3.8. At low dye concentrations, energy transfer from Cyto 840 to the UCNP steadily increases. This trend agrees with the intuition that as more dye is adsorbed, there are more opportunities for transfer between the dye and the lanthanides near the particle's surface. PL_{810} reaches a maximum at ~2.3 μM and then decreases slowly across a wide concentration range. This result demonstrates that there is an optimal assembly concentration for the first half of the relay that maximizes the total energy transfer across the ensemble of devices. Above this point, there is a reduction in PL that is likely due to two mechanisms: inter-Cyto 840 quenching as a result of decreased distances between fluorophores at high surface densities and direct quenching of UCNP emission as described in the following analysis

of PL_{980} [53]. It's worth noting that this same trend was observed for other dye-sensitized UCNPs [53, 54].

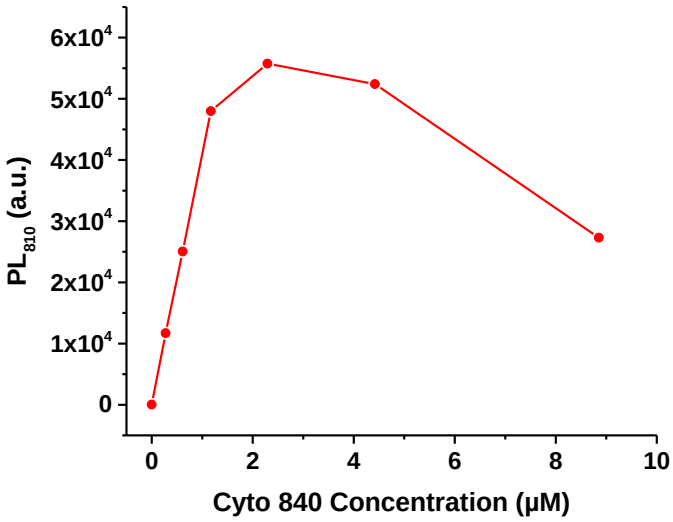

Figure 3.8: Integrated UCNP PL from UCNP-Cyto 840 complexes as a function of the Cyto 840 assembly concentration.

Direct excitation of the UCNP-Cyto 840 complexes at 980 nm reveals that, in addition to transferring energy to the particles, Cyto 840 also quenches the particle's emission. Figure 3.9 shows the emission for each UCNP-Cyto 840 complex when directly excited. As the Cyto 840 concentration increases, UCNP emission consistently decreases. This effect is observed nearly equally across all peaks, indicating that it is either the result of contact quenching or a resonant energy transfer process with the Yb^{3+} dopants that affects all downstream emission peaks uniformly. Although this result is not ideal, it does not prohibit the first half of the relay from working properly, as demonstrated by

the PL_{810} results. Future relay designs should explore the use of other NIR absorbing dyes to avoid this undesired effect.

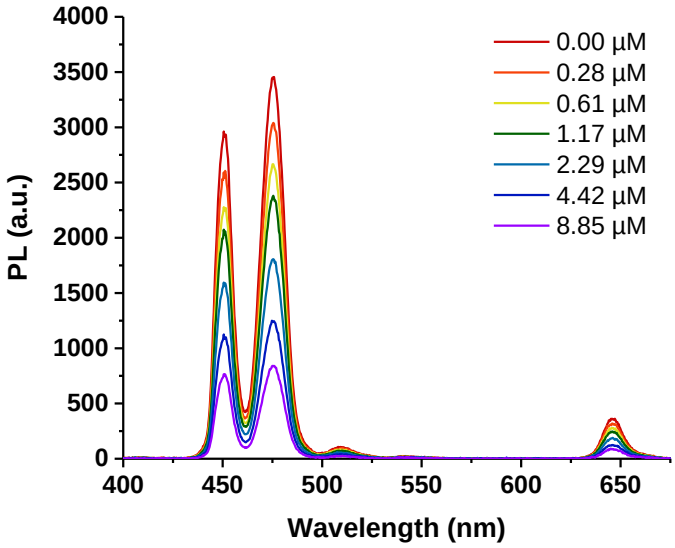

Figure 3.9: Emission spectra for UCNP-Cyto 840 complexes (assembled with different Cyto 840 concentrations) when the particles are directly excited at 980 nm.

In hopes of ascertaining the number of adsorbed Cyto 840 molecules per UCNP, and possibly the overall efficiency of this process, we attempted to remove remaining free dye from each sample using a variety of cleaning strategies. First, we tried pelleting and cleaning the complexes by centrifugation; however, this formed irreversible aggregates that could not be separated by extensive sonication or by the addition of common surfactants. Filtration of free dye by size exclusion also proved ineffective, simply due to the destructive nature of chloroform towards most centrifugal membrane materials. Inspired by other phase extraction techniques for removing free dye we tried an aqueous phase extraction method in which an immiscible layer of aqueous buffer was

added to the sample to extract free dye from the chloroform based on the dye's hydrophilicity [60]. This method successfully removed free dye from the chloroform, but it also created a white, gel-like emulsion of the complexes at the interface between solvents.

Without a non-destructive cleaning process, we could not determine the number of adsorbed fluorophores per particle or the overall efficiency of this energy transfer process. We did, however, find that the decreasing UCNP emission due to Cyto 840 loading can be accurately modeled by a combination of Langmuir adsorption and linear quenching per adsorbed dye. Fitting this model to our experimental results ultimately provides us with the fractional occupancy of adsorbed dye as a function of the dye concentration.

In this model, we first hypothesize that the dye adsorption is a Langmuir process (described in Appendix C). This requires that adsorption is a reversible reaction and reaches equilibrium by the time of measurement. These assumptions are corroborated by two observations. First, we find that much of the free dye remains in the supernatant after centrifugation of the assembled complexes, and second, we do not see any changes in PL from these complexes even hours after taking initial measurements. The first observation ensures that the adsorption reaction does not run to completion, and is

therefore likely to be in equilibrium. The latter indicates that the samples have reached equilibrium before measurements are taken.

Based on the assumptions above, we developed the slightly modified Langmuir model shown in Equation 3.1 to capture the normalized PL_{980} results from the Cyto 840 concentration bracket. In this equation θ_{cyto} is the fractional occupancy of Cyto 840, K_{cyto} is the equilibrium constant for the reversible adsorption process, [C] is the equilibrium concentration of Cyto 840, and q is a constant representing the quenching per fractional occupancy of the dye. In this model, we approximate the equilibrium concentration of Cyto 840 as the total concentration of Cyto 840, which is valid as long as the concentration of free dye is much greater than the concentration of adsorbed dye. Based on a 10 mg/mL stock concentration and the TEM measurements in Figure 3.10 , we estimate that the final particle molarity, i.e., roughly the adsorbed dye concentration, is ~11.4 nM,[1] approximately 10 to 1000 times lower than the total dye concentration.

$$\text{Normalized } PL_{980} = 1 - q\theta_{cyto} = 1 - \frac{qK_{cyto}[C]}{1 + K_{cyto}[C]} \qquad \text{Equation 3.1}$$

[1] To estimate the UCNP molarity, the volume of the particles was first calculated to be 56867 nm^3 using the mean height of 38 nm and mean edge length of 24 nm. Given that a hexagonal $NaYF_4$ host lattice has a density of 4.21 g/cm^3, each particle has a mass of 2.39×10^{-16} g [61]. This implies a final concentration of 11.45 nM.

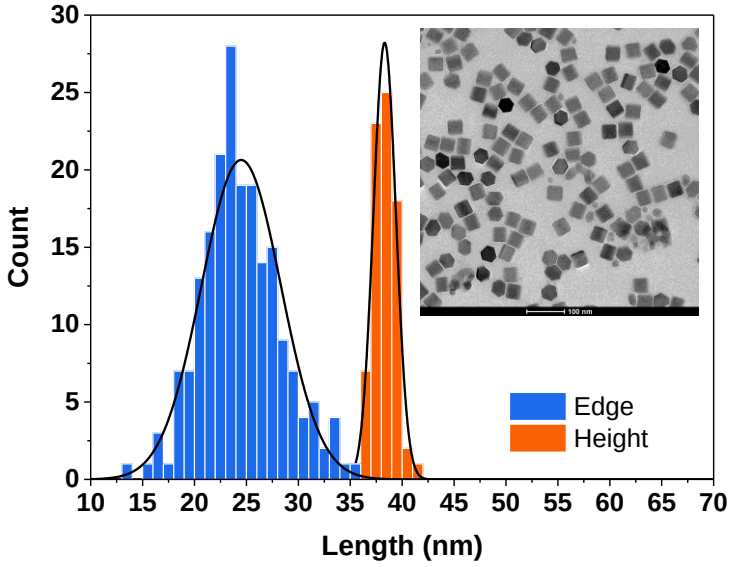

Figure 3.10: Edge length and height histograms taken from a TEM image (inset) of unmodified UNCPs.

To solve for the unknowns in Equation 3.1, we applied an unconstrained linear least squares fitting that resulted in K_{cyto} = 479335 and q = 0.94 with an R^2=0.99. Figure 3.11a plots the normalized PL_{980} data along with this best fit, showing that the model accurately captures the phenomenon. By solving for the equilibrium constant, K_{cyto}, we can also use Equation 3.1 to determine the fractional occupancy of Cyto 840 (θ_{cyto}) as a function of the dye concentration (Figure 3.11b). Based on the PL_{810} results in Figure 3.8, this relationship reveals that the performance of the first half of the relay peaks at roughly 52% of the total possible Cyto 840 occupancy.

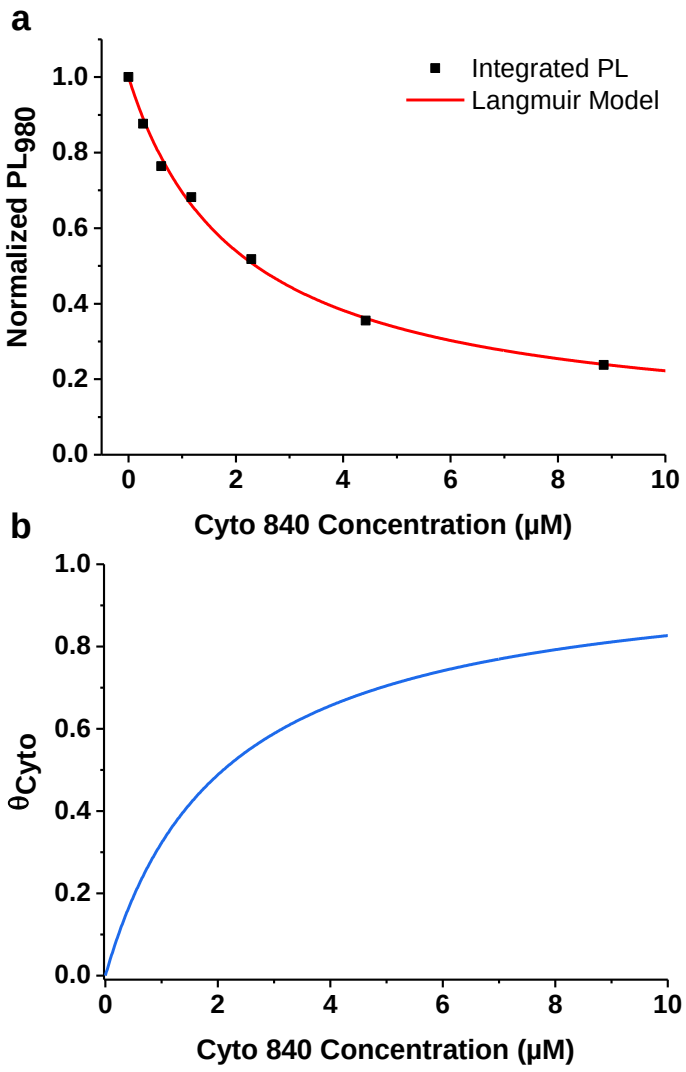

Figure 3.11: (a) Integrated and normalized UCNP PL from the Cyto 840 concentration bracket when exciting the UCNP directly at 980 nm. The red line represents the best fitting Langmuir model with parameters K_{eq} = 479335 and q = 0.94. (b) Fractional occupancy of adsorbed Cyto 840 (θ_{cyto}) as a function of the assembly concentration.

3.5 UCNP-ATTO 488 Characterization

The second half of the relay was characterized using a methodology similar to the first half. Transfer from the UCNP to ATTO 488 was first tested by exciting UCNP-ATTO 488 complexes at 980 nm and comparing the emission spectrum to controls consisting of only ATTO 488 and only UCNPs. The resulting emission spectra are shown in Figure 3.12. The ATTO 488 negative control did not have any detectable fluorescence. This ensures that any ATTO 488 emission detected in the other samples is not a result of direct multi-photon excitation. Both samples containing particles exhibited the standard UCNP emission spectrum. The UCNP-ATTO 488 sample, however, had increased PL around 525 nm, consistent with ATTO 488's standard emission spectrum and only slightly red-shifted from the published maximum at 523 nm, likely due to the organic solvents. Although slight, the additional PL in this region can be extracted from the total emission, as will be discussed in the following section, and strongly supports successful energy transfer from the lanthanides to ATTO 488.

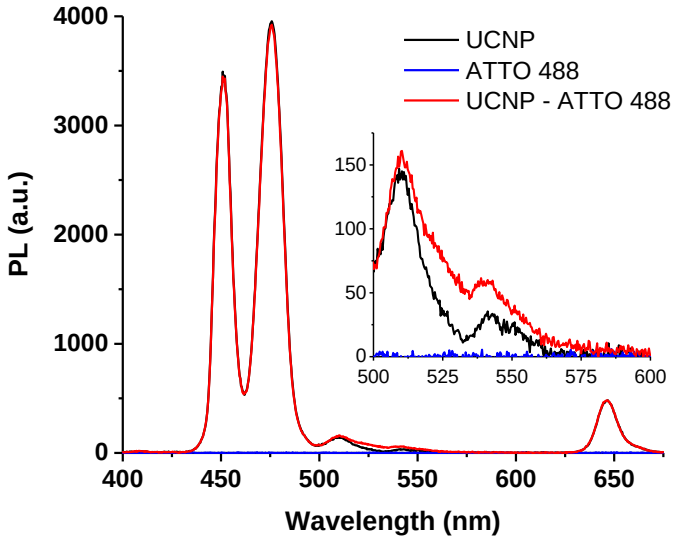

Figure 3.12: Emission spectra for the second half of the relay (UCNP-ATTO 488) and its negative controls. The inset focuses on the region where additional PL was detected due to ATTO 488 fluorescence.

Interestingly, a steady-state decrease in the donating UCNP emission peaks (at 450 nm and 475 nm) is not observed, which indicates that a large fraction of Tm^{3+} ions have difficulty transferring energy to ATTO 488. This result may stem from the difference in de-excitation pathways between ions at the surface and those buried slightly below. Surface ions are thought to be quenched by the vibrations of the organic ligands [46]. This theory is supported by the upconversion enhancement witnessed upon adding an un-doped $NaYF_4$ shell to UCNPs, thereby removing any interaction between the ligands and ions [62]. Given this information, ions buried slightly below the surface, and farther away from the dyes, are largely responsible for the emission from the particles. By offering an additional energy transfer route to the surface dopants, it's

possible that ATTO 488 pulls energy from these typically quenched ions and allows them to contribute to the overall emission without disturbing the typical UCNP PL spectrum. Additional work is required to confirm this hypothesis.

After detecting transfer from the particle to the dye, we bracketed the ATTO 488 concentration to find the optimal assembly coordinates. Each sample was excited at 980 nm. The visible emission was collected and normalized to the UCNP's off resonance emission peak at 650 nm since it cannot contribute to ATTO 488 excitation. Normalizing all samples allows for the UCNP emission to be subtracted uniformly from each spectrum, leaving only the ATTO 488 emission. The resulting spectra are shown in Figure 3.13 after smoothing with a third order, 20 nm Savitzky–Golay filter to remove noise.

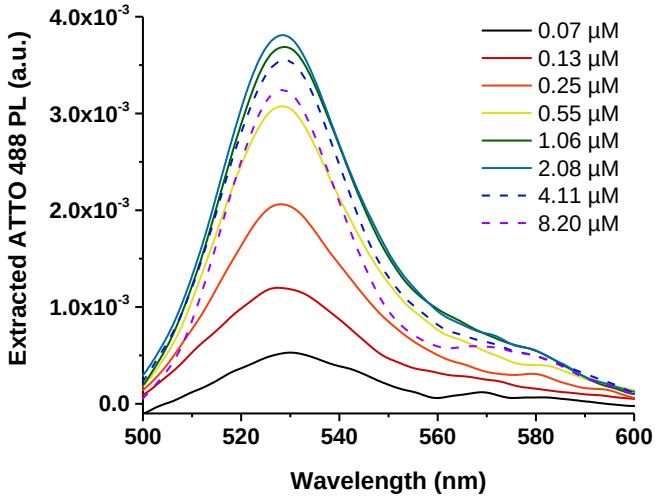

Figure 3.13: Extracted and smoothed ATTO 488 emission spectra for each sample in the concentration bracket. As the concentration increases, so does the ATTO 488 emission (solid lines). At high concentrations, this trend is reversed (dashed lines).

To assess the performance of the second half of the relay as a function of the ATTO 488 concentration, we integrated each of these spectra and plotted the fluorescence against the dye concentration (Figure 3.14). Similar to the Cyto 840 results, the ATTO 488 emission increases steeply at low concentrations and saturates at roughly 2 μM. Above this optimal concentration, the total emission gradually decreases. Close inspection of the extracted ATTO 488 spectra in Figure 3.13 shows that at these high concentrations the main emission peak centered around 525 nm decreases and a new secondary peak emerges at 575 nm. The appearance of this longer wavelength peak is characteristic of the formation of excimers [7], and is consistent with our previous hypothesis that the decrease in emission at high adsorption densities is largely due to inter-fluorophore interactions. It is also worth noting that the rate of this performance decrease is slightly lower for the second half of the relay than the first half. This is because, in addition to inter-fluorophore quenching, the first half also suffers from Cyto 840's direct quenching of the particle's emission, which we did not observe for ATTO 488.

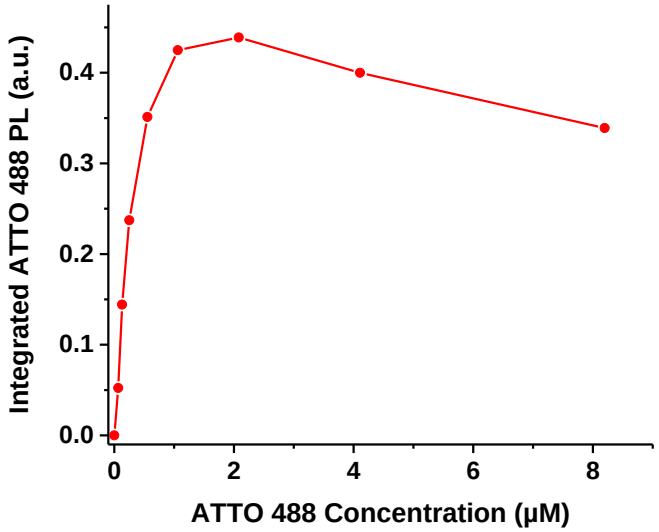

Figure 3.14: Integrated ATTO 488 PL for the second half of the relay as a function of the dye concentration.

Given that the Cyto 840 adsorption was accurately captured as a Langmuir process, we tested a similar model, summarized by Equation 3.2, on the initial portion of the ATTO 488 emission curve in Figure 3.14. In this model, θ_{at488} is the fractional occupancy of adsorbed ATTO 488, [A] is the ATTO 488 equilibrium concentration (and total dye concentration), K_{at488} is the adsorption equilibrium constant, and α represents the amount of ATTO 488 emission per fractional occupancy. As a first order approximation, the ATTO 488 emission is assumed to be linear with the factional occupancy. This approximation holds as long as the transfer efficiency between any adsorbed ATTO 488 molecule and its donating dopant is roughly the same for all adsorbed dyes, i.e., the efficiency does not change as a function of the surface coverage. Use of this linear transfer constant is supported by the uniform oleic acid ligand barrier

surrounding the particle that forces the fluorophores to all be nearly the same distance away from the surface, resulting in similar transfer efficiencies between fluorophores when averaged across an ensemble of constructs.

$$PL_{ATTO\ 488} = \alpha\theta_{at488} = \frac{\alpha K_{at488}[A]}{1 + K_{at488}[A]} \qquad \text{Equation 3.2}$$

We applied this model to the first six ATTO 488 concentrations to avoid the excimer effects noted earlier and found that a best fit with K_{at488} = 2409303 and α = 0.60 matches the data with an R^2 = 0.99. Figure 3.15a compares the integrated ATTO 488 emission to this best fit. Just as with Cyto 840, this model allows us to plot the fractional occupancy as a function of the ATTO 488 concentration (Figure 3.15b) and determine that the optimal ATTO 488 occupancy is roughly 83%. This fractional occupancy value is much larger than that of Cyto 840, but it is important to remember that the total number of adsorption sites likely varies between these two dyes due to differences in size, shape, and charge distributions of the fluorophores.

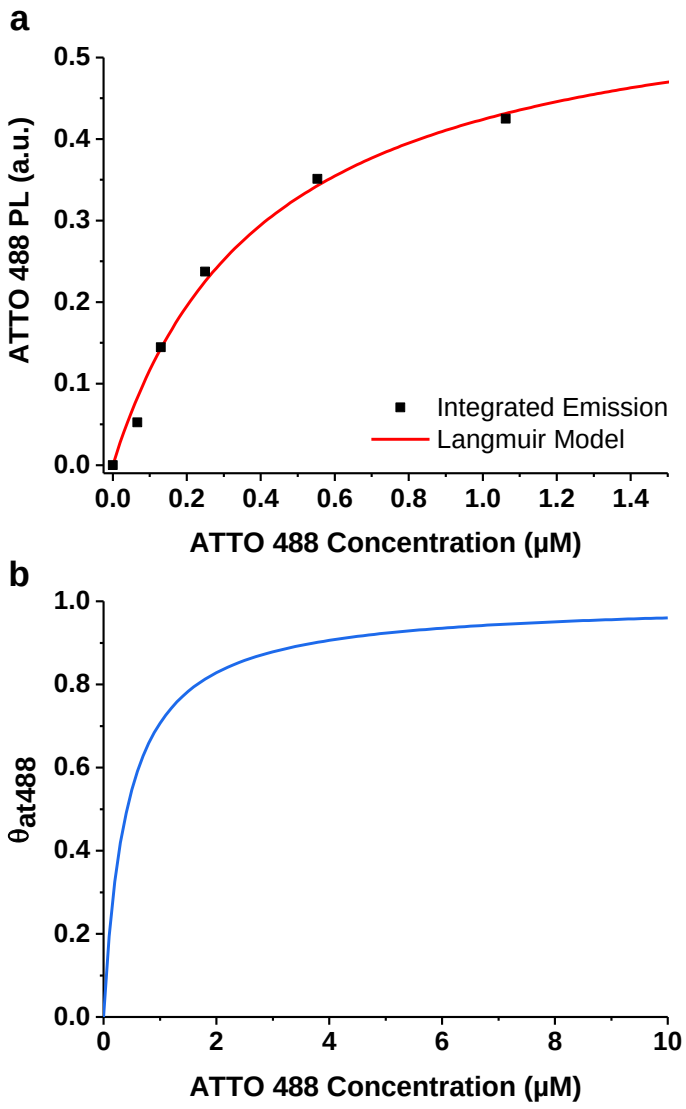

Figure 3.15: (a) Integrated ATTO 488 emission due to energy transfer from the UCNPs when excited at 980 nm. The red curve represents the best Langmuir fit with K_{at488} = 2409303 and α = 0.60. (b) ATTO 488 fractional occupancy as a function of the dye concentration.

3.6 Full Relay Characterization

After confirming that the individual halves function properly, the full RET relay was evaluated by assembling the entire construct following the same procedure used earlier but now adding both dyes. The constructs were then excited at 810 nm and the resulting PL was compared to a UCNP-Cyto 840 control. When comparing these two spectra, any additional PL detected in the ATTO 488 emission region around 525 nm supports successful transfer throughout the entire assembly. The results of this experiment, illustrated by Figure 3.16a, show that the relay's main Tm^{3+} emission peak at 475 nm is notably lower than its associated UCNP-Cyto 840 control, suggesting that ATTO 488 competes with Cyto 840 for adsorption spots. Competition lowers the Cyto 840 occupancy and therefore decreases the UCNP emission. Despite this decrease, PL in the ATTO 488 emission region increases, as demonstrated by the inset of Figure 3.16a. It is worth noting that the emission in this region is slightly different than the emission from the UCNP-ATTO488 samples in Figure 3.12, simply due to the altered UCNP emission spectrum resulting from Cyto 840 transfer rather than direct excitation (explained earlier in Section 3.4).

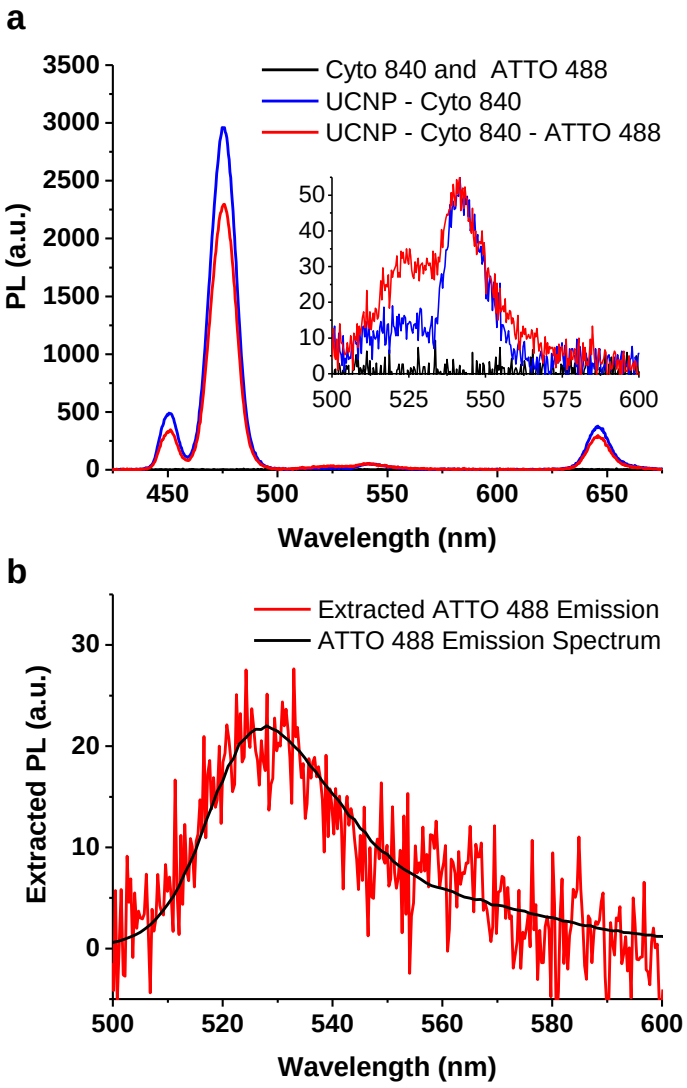

Figure 3.16: (a) Emission from the RET relay compared to a dye only control and the respective UCNP-Cyto 840 construct assembled at the same working conditions (analyzed earlier). The inset graph shows the increase in relay emission around 525 nm. (b) Extracted ATTO 488 emission from the relay in (a) with the ATTO 488 emission spectrum overlaid for comparison.

The ATTO 488 fluorescence from the relay sample in Figure 3.16a can be extracted by normalizing the UCNP-Cyto 840 control to the relay's 650 nm peak (again because it does not interact with any of the fluorophores) and then subtracting the UCNP PL. The remaining fluorescence, shown in Figure 3.16b, resembles the expected ATTO 488 emission spectrum, verifying that the RET relay successfully converts low energy excitons donated by Cyto 840 into high energy excitons accepted, and subsequently fluoresced, by ATTO 488.

To better understand the competitive nature of dye adsorption and to probe the relay performance as a function of the individual dye concentrations, we assembled nine different relays using three Cyto 840 concentrations and three ATTO 488 concentrations. The relays were excited at 810 nm and their emission spectra were compared to the corresponding UCNP-Cyto 840 complex assembled at the same Cyto 840 concentration. We extracted the ATTO 488 emission from each sample by subtracting the scaled controls, i.e. UCNP emission, and integrating the remaining PL between 500 nm and 600 nm. Figure 3.17 summarizes the results of this survey.

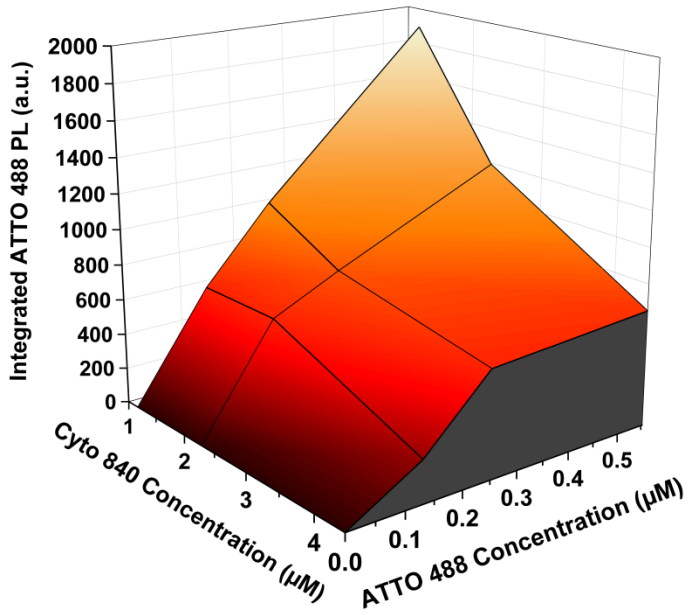

Figure 3.17: Extracted and integrated ATTO 488 PL for the nine different RET relays and their UCNP-Cyto 840 controls (ATTO 488 concentration = 0 μM).

All nine relay configurations contained measurable ATTO 488 emission, demonstrating the robustness of the relay assembly procedure against different dye concentrations. Across the survey, we observe a few important trends that further illustrate the competitive nature of assembly. When the Cyto 840 concentration is kept constant and the ATTO 488 concentration is raised, the ATTO 488 emission increases. The span of this increase depends on the Cyto 840 concentration. If the Cyto 840 concentration is high, it is difficult for ATTO 488 to compete for adsorption spots, leading to a lower maximum ATTO 488 emission. Conversely, at low Cyto 840 concentrations, ATTO 488 more effectively competes with the other dye, resulting in more adsorbed ATTO 488 and therefore a much higher emission maximum. For this

survey, we specifically chose higher Cyto 840 concentrations than the ATTO 488 concentrations to ensure that the throughput from the first half of the relay was sufficient for exciting ATTO 488 and providing extractable ATTO 488 emission. If the Cyto 840 concentration was further lowered to the point where ATTO 488 becomes the dominant dye, this trend would likely be reversed. ATTO 488 would then outcompete Cyto 840 and transfer from Cyto 840 to the particle's dopants would become the limiting factor in exciton throughput.

3.7 Summary and Future Challenges

We have designed and demonstrated a composite nanostructure, known as the RET relay, capable of converting many low energy excitons into a single high energy exciton. To fabricate the relay, we developed a simple assembly procedure in which both dyes are adsorbed to the nanoparticles. We demonstrated that this adsorption can be modeled as a Langmuir process, and that there is a fractional occupancy for each dye that maximizes energy transfer to or from the particle. Most importantly, we provided significant evidence that the relay operates as designed. Excitation of the NIR input fluorophore produces visible emission from the output fluorophore.

Despite this success, a variety of technical challenges remain before this proof-of-concept device can be fully integrated into RET systems. First, the current version of the RET relay is assembled in a solvent mixture composed of chloroform and DMSO. Given

DNA's preference for aqueous environments, the relay must be transferred to a buffer that is compatible with the self-assembly of DNA nanostructures. While there are techniques for transferring UCNPs into aqueous solutions, e.g. coating them with a silica shell or hydrophilic ligands, these protocols have yet to be tested with the current relay assembly procedure [55, 62-64]. In addition to transferring buffers, the relay must be coated with functional groups that enable the attachment of DNA. Without this functionalization, it will be difficult to bring RET networks into close proximity with the relay fluorophores and utilize the device's energy restoration.

Even if these integration challenges can be overcome, the RET relay still suffers from substantial exciton loss, which may weaken its utility in large-scale RET networks. The relay requires at least three low energy excitons to create a high energy exciton, and although we do not know the overall transfer efficiency of the relay, the results in Section 3.6 indicate that this throughput is low given the small amount of ATTO 488 fluorescence extracted from the device. Without a method for improving this efficiency, this throughput may render the relay impractical when placed between RET networks that already experience significant exciton loss.

To overcome this exciton loss, and the general exciton loss experienced by all RET networks, we began investigating methods for storing excitons with the intention of building capacitor-like devices that could accumulate these carriers over time. These

capacitive elements could then be embedded in RET systems at locations where the exciton loss falls below some observational threshold, and after sufficient accumulation from upstream networks, they could be discharged to supply excitons to downstream devices. While searching for a mechanism that would allow us to retain excitons for extended periods of time, however, we were introduced to the dark states of fluorescent molecules. Dark states are long-lived, non-fluorescent states of fluorophores, optically accessed by a photoinduced chemical reaction between the fluorophore and certain small molecules. Realizing that the unique properties of the dark state could be applied to RET logic, we shifted our focus from the design of a capacitive element to the development of an entirely new method of RET logic design that leverages this state to dynamically modulate RET networks. Ultimately, we found that this form of RET logic design overcomes both the exciton loss and energy loss experienced by RET systems, thereby rendering the exciton capacitor unnecessary. The remainder of this dissertation focuses on this new form of RET logic, beginning with the basic design principles of logic gates and cascades.

4. Pre-Charge Logic

In this chapter, we introduce a new style of RET logic design that overcomes both exciton loss and energy loss, and provides a variety of new logic gates for performing complex operations within a single RET network. This new method of RET logic design, called Pre-Charge Logic, leverages the dark states of fluorescent molecules, named accordingly for their lack of fluorescence, to modulate the flow of excitons by temporarily turning specific molecules off.

We begin this chapter with an overview of the dark state. We then propose various methods for harnessing this state so that it can be properly applied towards RET devices. Afterwards, we explain the design principles of PCL, demonstrating how the dark state can be exploited to construct a library of nonlinear RET logic gates including AND, OR, NAND, NOR, XOR, XNOR, PASS, NPASS. We show that these logic gates can be combined to implement complex Boolean functions using two different cascading techniques, one of which completely decouples the overall length of a RET circuit from both its exciton loss and its energy loss.

4.1 The Dark State

When excited in the presence of certain thiolated reducing agents, fluorophores may transition from their standard excited singlet state to a non-fluorescent dark state [65]. This dark state has a number of unique properties that can be applied towards the

construction of novel RET devices. First, as indicated by its name, a fluorophore in the dark state cannot fluoresce; nor, can it accept excitons [66]. Thus, similar to saturation (see Section 2.3.3), the dark state provides a method for temporarily switching off a fluorophore in a RET network.

Over time, dark fluorophores spontaneously return to their ground state. In contrast to the nanosecond lifetimes of fluorescent singlet states, however, dark states can persist for fractions of a second to hours depending on the molecular pathways involved [65]. This long lifetime can be exploited to retain state in RET systems for roughly 10^8 longer than typical fluorescence timescales [67]. It also implies that, in contrast to saturation, the dark state requires significantly less power to keep fluorophores inaccessible. If this long lifetime is undesirable, most dark fluorophores can be reset to their ground state by UV excitation, or by exciting an activator fluorophore positioned nearby [65, 68-71]. These mechanisms can be utilized to perform global and fluorophore-specific resets respectively when leveraging the dark state to build logic devices.

The dark transition is in general a low probability event, requiring many excitation cycles before occurring; however, the underlying mechanism responsible for inducing the dark state differs between fluorophores. One such mechanism is depicted in Figure 4.1a. In this particular case, the fluorophore spontaneously enters its triplet

state via intersystem crossing and is then reduced by the thiol group (SH) of the reducing agent (Figure 4.1b), i.e. the triplet state fluorophore accepts an additional electron. This particular pathway has been verified for a wide range of fluorophores covering most of the visible spectrum, each derived from the same base fluorophore, rhodamine [65, 72]. Fluorophores derived from other base structures follow alternative pathways to reach their dark state. Oxazine, for example, undergoes multiple reduction events [73], while certain fluorophores like cyanine, e.g. Cy5 and Cy7, undergo an entirely different reaction altogether [74]. Although this underlying mechanism can influence certain dark state characteristics, such as the yield and lifetime of this process, dark fluorophores tend to share the general set of properties described earlier. Thus, for the sake of simplicity, we will disregard the underlying dark state mechanism when discussing how this state can be applied to RET logic. When choosing specific fluorophores to implement these networks, their unique properties will be considered (as done in the experimental demonstration provided by Chapter 6).

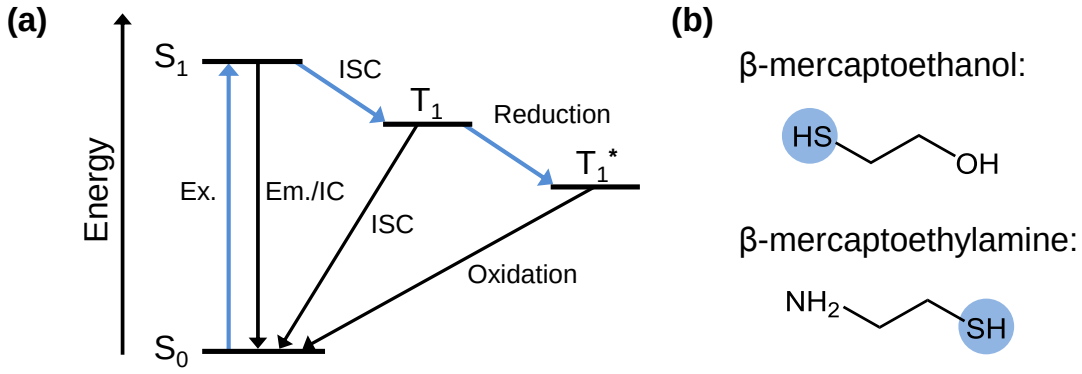

Figure 4.1: (a) A simplified Jablonski diagram showing the triplet reduction pathway responsible for certain dark states (redrawn from reference [65]). (b) Molecular structures of β-mercaptoethanol and β-mercaptoethylamine (MEA), two thiolated reducing agents commonly used for inducing the dark state. The thiol group is highlighted in both molecules.

There are two common methods for experimentally observing the dark state. The first method is to observe a change in its fluorescence as a function of time. As molecules enter the dark state, the fluorescence from a population of fluorophores decreases since the molecules in the dark state are unable to participate in the singlet transitions associated with fluorescence. Figure 4.2 demonstrates an example of this measurement for a ~15 μM sample of ATTO 488 when excited at 520 nm in the presence of 100 mM MEA. Over time, the population of dark state fluorophores increases, resulting in less ATTO 488 available for excitation and therefore decreasing fluorescence from the sample. For comparison, Figure 4.2 also shows the fluorescence from a control sample of ATTO 488 under the same excitation conditions but without the reducing agent present.

Without MEA, ATTO 488 cannot transition to the dark state and the sample's fluorescence remains nearly constant.

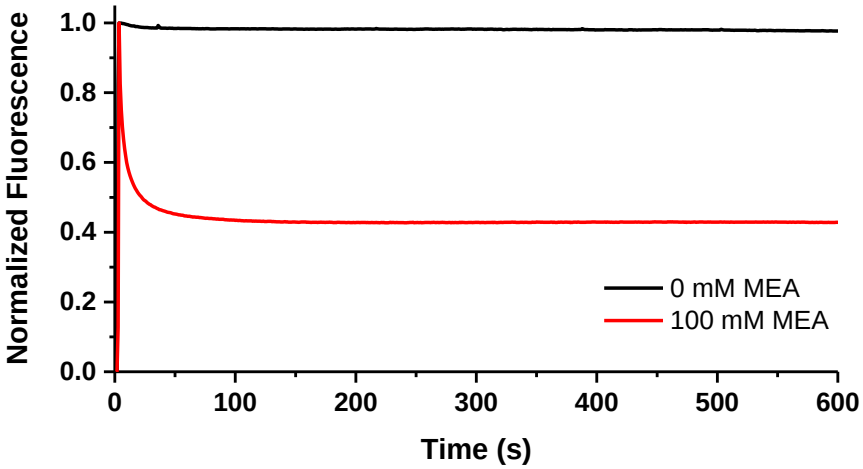

Figure 4.2. Fluorescence time traces of ATTO 488 in the presence and absence of MEA.

The second standard method for observing the dark state is to measure a change in absorbance. Molecules that have entered the dark state no longer exhibit their standard excitation peak in the visible spectrum. This forces the total sample's absorbance in this region to decrease. Furthermore, for fluorophores accessing their reduced triplet state, a new absorbance peak emerges in the UV region. Figure 4.3 demonstrates this change in absorbance for a sample of ATTO 532 in 1X PBS buffer with 100 mM MEA, before (black curve) and after (red curve) excitation. After excitation, the sample's primary 530 nm absorbance peak has decreased and a new peak at ~425 nm has appeared.

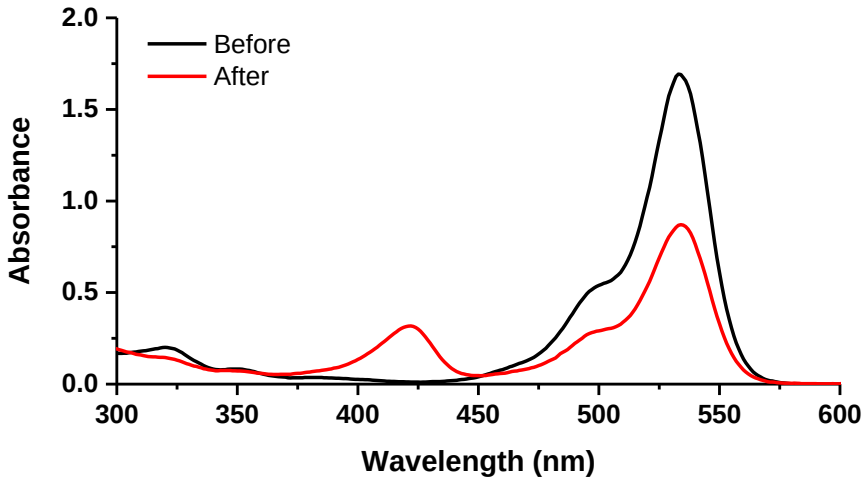

Figure 4.3: Changes in the absorbance of ATTO 532 due to dark state formation.

4.1.1 Localizing the Dark State

To apply the dark state properties described in the previous section to RET logic, we must be able to choose which fluorophores in a RET network can undergo a dark state transition. Certain portions of RET circuitry, such as wires and inputs, should never be subject to this modulation. If these components are turned off, the RET circuit will not function properly. We refer to the notion of limiting this dark transition to specific fluorophores, localization of the dark state.

The simplest method for localizing the dark state is to categorize fluorophores into susceptible and unsusceptible groups. RET devices that utilize the dark state can be constructed from the susceptible set, while wires and other static circuit elements can be constructed from the unsusceptible set. This categorization has already been

demonstrated for certain groups of dyes. For example, while studying the mechanism responsible for dark state transitions in cyanine derived fluorophores, Dempsey et al. noted that Cy3 does not undergo a dark transition even though the closely related Cy5 does [74]. In this case, the authors hypothesized that this difference was due to the length of each fluorophore's polymethine chain, which forms a complex with the thiolated reducing agent for Cy5 but may not be long enough to do so for Cy3.

For groups of fluorophores that have not yet been categorized, it may be possible to predict this categorization by assuming that triplet reduction is responsible for most dark state transitions and using the Rehm-Weller equation shown in Equation 4.1 [75]. This equation calculates the Gibbs free energy associated with photoinduced electron transfer based on the oxidation potential of the reducing agent (E_{ox}), the reduction potential of the fluorophore (E_{red}), the difference in energy between the fluorophore's excited state (the triplet state in this case) and its ground state, and the Coulombic interaction between the resulting products (often assumed to be 0 in water). For susceptible fluorophores, this reaction should be thermodynamically favorable ($\Delta G < 0$); otherwise, the fluorophore will be largely unsusceptible since the reaction will not proceed spontaneously. It's worth noting that a precise division between categories might be unnecessary. Certain fluorophores may have such a low dark transition rate,

that they can be pragmatically classified as unsusceptible despite their ability to enter the dark state.

$$\Delta G = E_{ox} - E_{red} - E_{0,0} + C \qquad \text{Equation 4.1}$$

Categorization simplifies the process of designing RET networks that leverage the dark state but it inherently places restrictions on which fluorophores can be used to build different portions of a RET system. If the dark state can instead be spatially controlled such that only fluorophores positioned at certain locations undergo a dark transition, these design constraints can be avoided.

All dark state transitions require some interaction between the fluorophore and the reducing agent. Based on this simple observation, we can reasonably hypothesize that if we control the diffusional volume of the reducing agent, we ensure that only fluorophores within its vicinity undergo a dark transition. One plausible method for achieving this spatial localization is illustrated in Figure 4.4. In this example, multiple thiol groups are placed within close proximity of a fluorophore by tethering them directly to the DNA helix rather than allowing them to freely diffuse in solution. Thus, they are constrained to inducing a dark transition in only the neighboring fluorophore. It's worth noting that a similar concept is routinely used in nucleic acid templated chemistry, whereby a DNA substrate positions different precursors relative to one another to induce a desired chemical reaction [76].

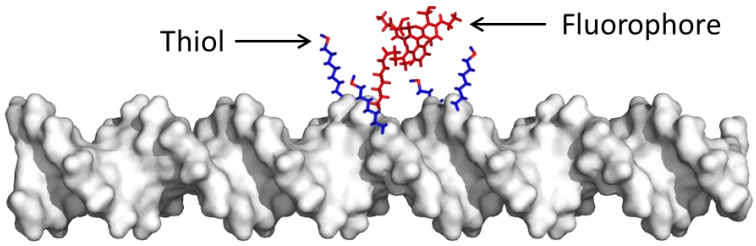

Figure 4.4: Illustration of one plausible method for spatially localizing the dark state. A fluorophore and multiple thiol groups are placed within close proximity of one another using a DNA helix, which restricts the interaction of the reducing agents to only their neighboring fluorophore.

We did experimentally test a simplified version of this localization scheme by placing a single thiol group directly next to ATTO 532, a fluorophore known to undergo a dark transition via the reduced triplet state (Figure 4.5a). When excited, we observed a greater decrease in the time-resolved fluorescence from the thiolated duplex than from a control duplex without the thiol group present (Figure 4.5b). However, the difference was slight and we did not witness a change in ATTO 532's absorbance spectrum. Although inconclusive, the difference in time-resolved fluorescence is encouraging and certainly warrants further investigation. We hypothesize that adding multiple thiol groups, as described above, may provide additional opportunities for the fluorophore-thiol interaction and therefore increase the likelihood of dark state formation.

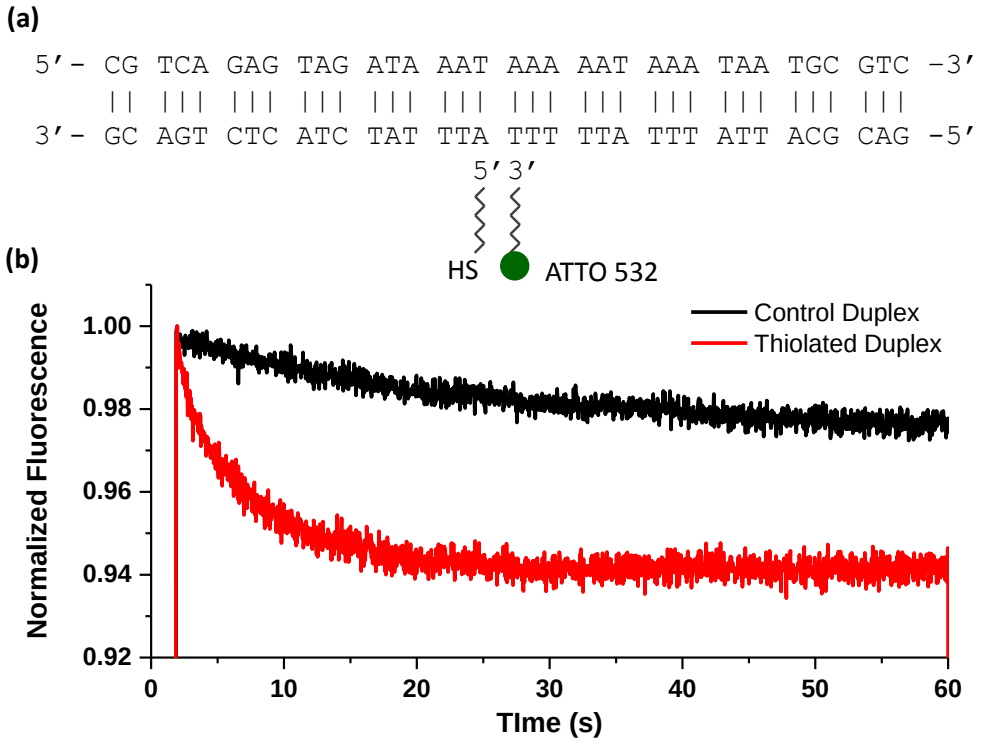

Figure 4.5: (a) Positioning of ATTO 532 and a thiol group on a DNA duplex used to test spatial localization of the dark state. (b) Normalized fluorescence time traces from ATTO 532 with and without the thiol group present.

If triplet reduction is responsible for the dark state, and the multi-thiol localization method in Figure 4.4 does not offer enough control over the electron-hole recombination rates for this reaction to proceed with reasonable efficiency, it may also be possible to design the sequence of the underlying DNA structure to alter the dynamics of this reaction. Guanine is easily oxidized and has been used to transport and trap holes along DNA duplexes [77-79]. This transport can potentially be exploited to move the hole away from the reduction reaction, thereby lowering the recombination rate and extending the lifetime of the dark state [80]. In fact, the direct reduction of

certain fluorophores' singlet states by guanine, and the use of guanine to transport and trap the resulting hole, have both been experimentally validated [81-83].

Spatial localization offers a variety of benefits over categorical localization. RET circuit designers only need to determine which fluorophores in a RET network should have the ability to undergo a dark transition, and attach the reducing agent nearby before the assembly process. Both static and dynamic portions of systems can be constructed with fluorophores known to undergo a dark transition, providing more flexibility during the RET network design process. Spatial localization also allows multiple copies of the same susceptible fluorophore to be embedded in a single RET network, with only certain instances of this fluorophore being modulated when excited.

4.1.2 Examples of the Dark State Applied to RET Networks

While spatial localization has yet to be demonstrated, categorical localization has been used to build a few simple RET devices that leverage the dark state (even if not explicitly described as categorical localization by the authors). The first example is a simple two-fluorophore system composed of only Cy3 and Cy5 tethered to the same end of a DNA duplex [69]. Using β-mercaptoethanol as the reducing agent, Cy5 is turned off by exciting the fluorophore at its primary excitation wavelength. Cy3 functions as an activator fluorophore. If it is excited while Cy5 resides in its dark state, Cy5 is forced back to its ground state, allowing it to fluoresce again until returning to its dark state. To

the best of our knowledge, the underlying activation mechanism provided by Cy3 is still unknown; yet, the mechanism is now commonly exploited in the field of super-resolution imaging [70, 71, 84]. With this fluorophore arrangement, fluorescence from Cy5 is effectively toggled on and off using two different wavelengths of light.

Exploiting both the dark state and activator fluorophores, Nishimura et al. constructed a three fluorophore device that functions much like an optical latch [67]. The latch consists of a single donor-acceptor pair with an activator fluorophore located near the acceptor. To read the latch, the donor is excited. If the acceptor fluoresces, then the output is a logical 1; otherwise, the output is a logical 0. The device is reset by placing the acceptor in the dark state. To set the latch, the activator is excited, which allows the acceptor to fluoresce again. This example demonstrates that the long lifetime of the dark state can be exploited to construct rewritable RET-based memory.

By combining two instances of the latch described above, Fuji et al. created a RET energy router, capable of directing excitons from a single donor to two different acceptors [66]. This device is composed of a central donor fluorophore located at the middle of a DNA duplex with two spectrally distinct acceptor-activator pairs at either end of the helix. Similar to the latch, the device is initialized by first placing both acceptors in the dark state. After initialization, the user can activate either of the two

acceptors by exciting the neighboring activator fluorophore. This allows the user to choose which of the two acceptors receives excitons from the central donor.

The examples above demonstrate the utility of the dark state for building RET networks that perform more complex operations than the basic circuit components described in Section 2.3. To the best of our knowledge, however, the dark state has yet to be applied towards the development of basic logic gates. In the following section, we describe a new style of RET logic design called Pre-Charge Logic, which exploits dark transitions to perform Boolean operations.

4.2 PCL Operation

To describe the basic operating principles and composition of PCL, we will use the AND gate depicted in Figure 4.6 as an example. This logic gate is composed of five distinct fluorophores. The blue fluorophore, labeled "eval", acts as the exciton source for the network and is excited to determine the computational result. The yellow fluorophore labeled "out" acts as the gate output. The green fluorophores running through the center of the device are called mediators, similar to the channel of the C-DEV described in Section 2.3.3. These molecules form a homo-RET wire connecting eval to out. Lastly, the orange and red fluorophores, labeled x_1 and x_2 respectively, are the inputs to the AND gate. These fluorophores are annotated with a "D", denoting that they can undergo a dark transition (using either categorical or spatial localization) while

the rest of the fluorophores cannot. Many PCL gates require a mixture of high and low transfer efficiencies. In the case of the AND gate, all transfer efficiencies should be high, except for the mediator-to-output transfer efficiency (as denoted by the line weights in the EFD of Figure 4.6). When simulating these logic gates in Chapter 5, we will explore the influence of these transfer efficiencies.

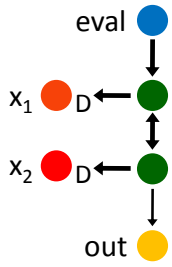

Figure 4.6: EFD for a PCL AND gate.

Inspired by CMOS domino logic, PCL operation is divided into two phases: a pre-charge phase in which the input conditions are established and an evaluation phase in which the output is assessed. During the pre-charge phase, inputs are applied by either an external light source or an upstream RET network that donates excitons to x_1 and/or x_2. If these inputs are true, after many excitation cycles, the input fluorophores transition to their dark states, making them inaccessible as RET acceptors. Once the inputs are set, the output is assessed by exciting eval with a low intensity source and monitoring the output. The duration of this evaluation phase should be kept short so as to correctly determine the output before inputs spontaneously return to ground or are accidentally placed in the dark state by the evaluation process. Determination of the

proper pre-charge and evaluation time scales depends on the excited and dark state lifetimes of the fluorophores used and are therefore explored in Chapter 6 when we experimentally demonstrate a PCL device.

Figure 4.7 illustrates the two-phase operation of the PCL AND gate when both inputs are true. During the pre-charge phase, both inputs are excited into their dark states. With these fluorophores temporarily removed, evaluation of the gate results in a high exciton flux from eval to out, and subsequently high output fluorescence interpreted as a logical 1. If either of the inputs is false, the associated input fluorophore would still be available as a RET acceptor. These acceptors would steal excitons from the mediators before reaching the output, resulting in a lower fluorescence signal interpreted as a logical 0. Over time, the device spontaneously resets. To force this reset, a UV source can be applied to the entire structure. Alternatively, exciting wavelength-multiplexed activator fluorophores positioned close to each input (not shown in Figure 4.7) would allow them to be reset individually.

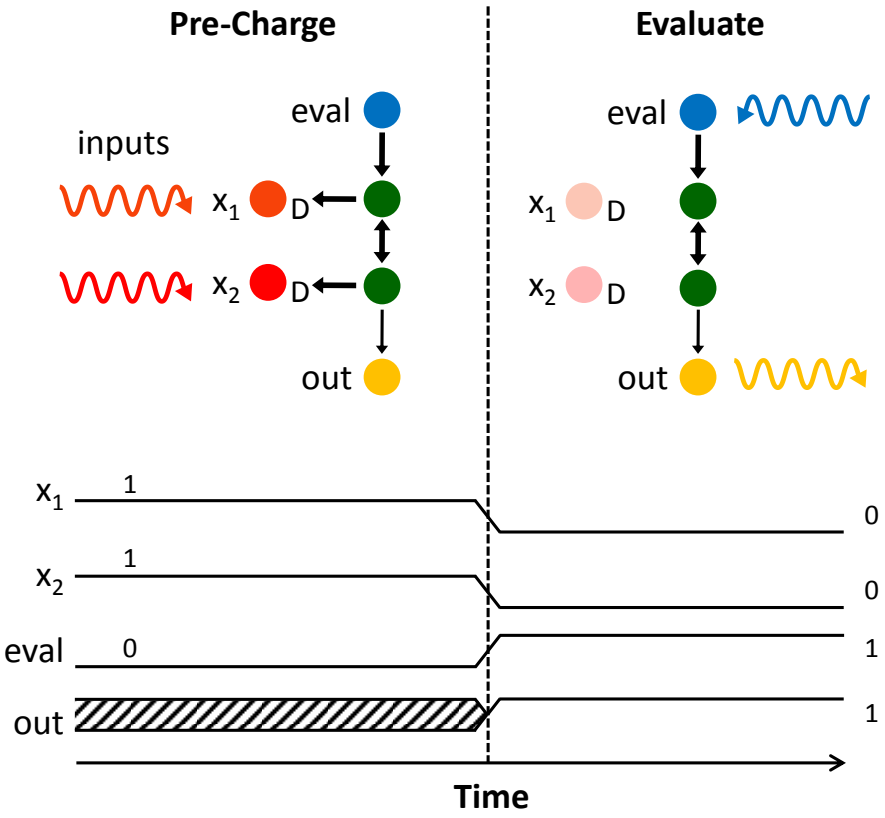

Figure 4.7: Two-phase operation of the PCL AND gate when both inputs, x_1 and x_2, are true. Note that the time scale may not accurately represent the ratio of the pre-charge and evaluation phase durations. Also, for the sake of simplicity, the time traces shown represent the binary interpretations of the output fluorescence, i.e. they are either above or below the 0-1 threshold.

4.3 A PCL Gate Library

The design concepts of the PCL AND gate can be extended to create a library of logic gates, shown in Figure 4.8.

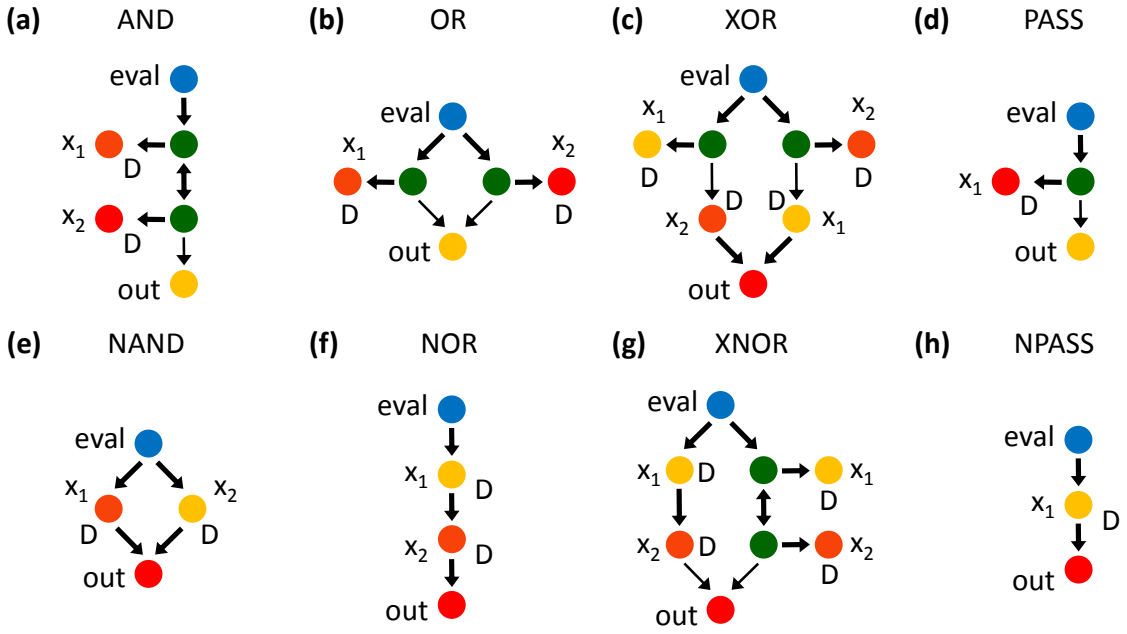

Figure 4.8: EFDs for (a) AND, (b) OR, (c) XOR, (d) PASS, (e) NAND, (f) NOR, (g) XNOR, and (h) NPASS PCL gates. These EFDs only include ideal RET pathways. When implemented with real fluorophores, there may be additional weak, undesirable RET paths between non-adjacent fluorophores.

The OR gate (Figure 4.8(b)) achieves its functionality by offering two independent exciton paths from eval to out. Each of these mediators has a corresponding input fluorophore that acts as a RET acceptor. Turning off either input removes that exciton sink, thereby increasing the output fluorescence above the 0-1 threshold. Comparing the OR and AND EFDs, similarities between PCL and standard

switch-based logic design become apparent; devices in series produce AND operations, and devices in parallel produce OR operations.

In addition to the similarities above, PCL also adheres to De Morgan's laws, requiring AND and OR to be transposed whenever either operation is inverted. Accordingly, the NAND and NOR gates in Figure 4.8 are modified versions of the OR and AND gates respectively. To achieve negation, mediators are directly replaced by their input fluorophores. This allows RET paths from eval to out to be switched off rather than enhanced through the removal of competitive pathways. For example, the NAND gate in Figure 4.8(e) has two parallel paths from eval to out, each composed of one input fluorophore. Both inputs must be removed for the output fluorescence to significantly drop. The PASS gate and the NPASS gate are simply one-input versions of AND and NOR respectively.

Close inspection of positive and negative gate pairs, e.g. AND/NAND and OR/NOR, reveals that positive literals are implemented as mediator-input pairs and negative literals are implemented as inline inputs. Applying these concepts, we constructed the XOR and XNOR gates in Figure 4.8(c) and Figure 4.8(g) by physically implementing each gate's sum-of-products representation. For instance, XOR consists of the minterms $x_1\overline{x_2}$ and $\overline{x_1}x_2$. The first minterm is constructed by placing an x_1 mediator-input pair in series with an inline x_2 input. Following the same rules, the second

minterm is simply the inverse of the first minterm. XOR is then fashioned by summing these two minterms as independent RET paths from eval to out.

It should be noted that during the pre-charge phase, gates using inline inputs may exhibit significant output fluorescence since their inputs are directly wired to the output. The two-phase operation of PCL, however, ensures that this fluorescence does not interfere with an accurate reading of the output since inputs are not excited during evaluation. There is one additional complexity for NOR and XNOR gates. While pre-charging, excitons may travel downstream and mistakenly reduce other input fluorophores due to their serial layout. If this does occur when implemented with real fluorophores, it can be remedied by applying inputs sequentially starting from the top and resetting all downstream inputs (using additional activator fluorophores) before applying the next input.

4.4 Simple PCL Cascades

Individual PCL gates can be cascaded to create more complex circuits. Cascades are formed by connecting multiple inputs to one or more mediator paths from eval to out. All inputs are applied simultaneously during the pre-charge phase and the evaluation phase follows as normal. By using the same mediator fluorophore throughout the circuit, the number of unique fluorophores required by a PCL cascade only scales with the number of inputs. This is a substantial improvement over the

spectral content of cascades formed by previous methods of RET logic design (assuming that the inputs and outputs of each logic gate are compatible), in which each logic gate requires a unique fluorophore for both its input and output.

Figure 4.9a shows the EFD for a serial PCL AND-OR cascade performing the logical operation out=$x_1x_2(x_3+x_4)$. PCL gates can also be combined in parallel, as illustrated by the EFD in Figure 4.9b, which performs the operation out=$x_1x_2+x_3x_4$. Note that the serial arrangement implements the product of the two logic gates while the parallel arrangement implements the sum of the two logic gates. Thus, the same design principles of individual PCL gates also apply to PCL cascades. Both of these cascades are simulated using CTMC models, described in Section 5.4.

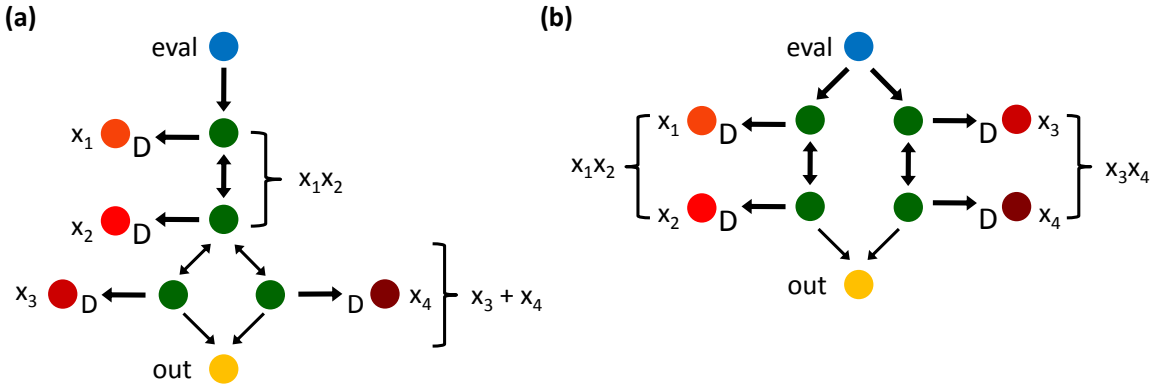

Figure 4.9: (a) PCL gates combined serially to implement out = $x_1x_2(x_3+x_4)$. (b) PCL gates combined in parallel to implement out = $x_1x_2+x_3x_4$.

4.5 Multi-Eval PCL Cascades

The simple PCL cascades described above allow for the evaluation of complex Boolean logic; however, if these cascades are made too long, the total transfer efficiency from eval to out will be very low. To avoid this exciton loss and create larger systems, we have developed a separate cascading technique, referred to as Mult-Eval PCL (MEPCL). MEPCL decouples a cascade's end-to-end transfer efficiency from its total length by breaking the circuit into smaller portions of logic that are evaluated serially, each by their own eval fluorophore. This ensures that every fluorophore in the cascade is a finite number of RET steps away from an exciton source, and that this number of steps can be intentionally designed to accommodate an acceptable amount of exciton loss.

To illustrate the concept of MEPCL, we will use the basic four AND gate cascade shown in Figure 4.10a. When implemented with the simple PCL cascading technique explained in the previous section, the equivalent cascade (Figure 4.10b) requires excitons to undergo at least six separate RET events from eval to out. Even if each of these events proceeds with 90% transfer efficiency, the total transfer efficiency for this cascade is below 55%.

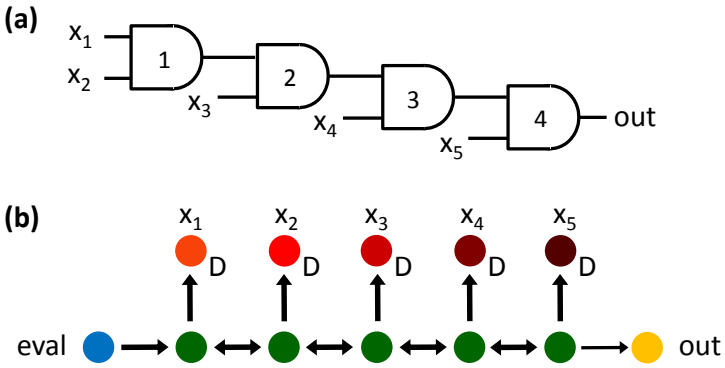

Figure 4.10: (a) A five input, four AND gate cascade where out =$x_1x_2x_3x_4x_5$. (b) A simple PCL cascade implementation of the circuit in (a).

MEPCL takes a more direct approach towards implementing this Boolean function. Instead of compressing the entire cascade into a single PCL gate, with one eval and one output, the MEPCL implementation wires individual AND gates together and evaluates them sequentially. The full EFD for this implementation is shown in Figure 4.11. For the sake of clarity, each AND gate in this EFD is encompassed by a dotted line and numbered according to the gate labels in Figure 4.10a. Similar to the conventional circuit schematic, the output of every AND gate, labeled out_n, serves as one of the inputs to the following AND gate. Each cascaded device has its own distinct eval fluorophore, labeled $eval_n$, which supplies excitons to only its local fluorophores, terminating at its respective output.

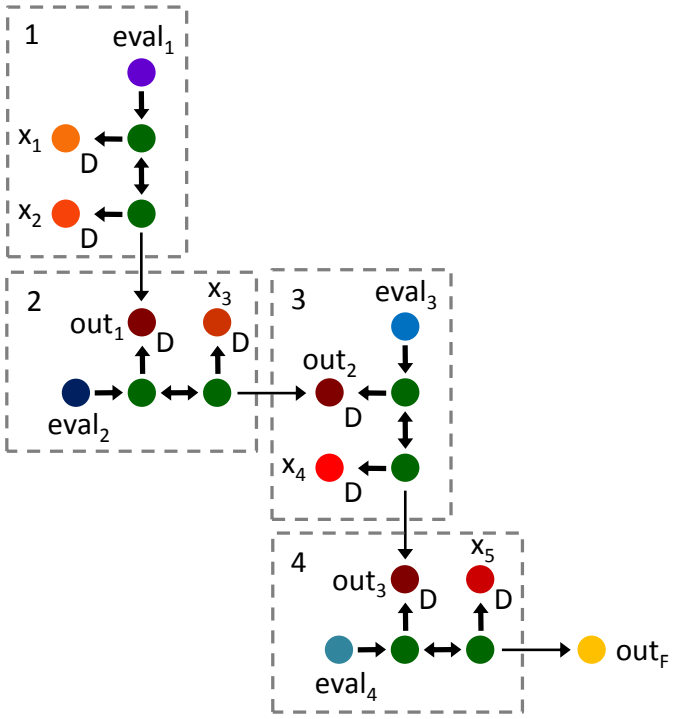

Figure 4.11: MEPCL implementation of the four AND gate cascade in Figure 4.10.

To illustrate how MEPCL works, Figure 4.12 shows the first two cycles of operation for the AND gate cascade, where both the pre-charge and evaluation of each logic gate are considered a single cycle. In the first cycle (Figure 4.12a), the inputs x_1 and x_2 are pre-charged and the first AND gate is evaluated by exciting $eval_1$. If both x_1 and x_2 are true, a high flux of excitons will traverse the mediators of this AND gate, reaching out_1 and placing this fluorophore in its dark state by the end of the evaluation period (the duration of which will depend on the actual implementation and is thus left as future work). If either x_1 or x_2 is false, out_1 will remain fluorescent. During the second cycle, the external inputs to the second AND gate are pre-charged (only x_3) and $eval_2$ is

evaluated.[1] Assuming that x_3 is true, and the previous AND gate was true, the second AND gate will also be true. Accordingly, out_2 will transition to its dark state during this evaluation period since there are no input fluorophores remaining to sink excitons (Figure 4.12b). If instead, the previous AND gate was false (Figure 4.12c), out_1 will still be available to steal excitons, leading the second AND gate to also be false. Operation continues in this serial fashion until the final output fluorophore, out_F, either fluoresces brightly (true) because all inputs were true or fluoresces weakly (false) because one or more inputs were false. Note that this final output fluorophore must be unique so that its fluorescence can be independently observed. The outputs for the first three AND gates, however, can all use the same fluorophore since they do not need to be externally addressed or observed.

[1] Input x_3 may be pre-charged during the evaluation phase of the first cycle. This strategy of overlapping pre-charge and evaluation phases can condense the total evaluation time.

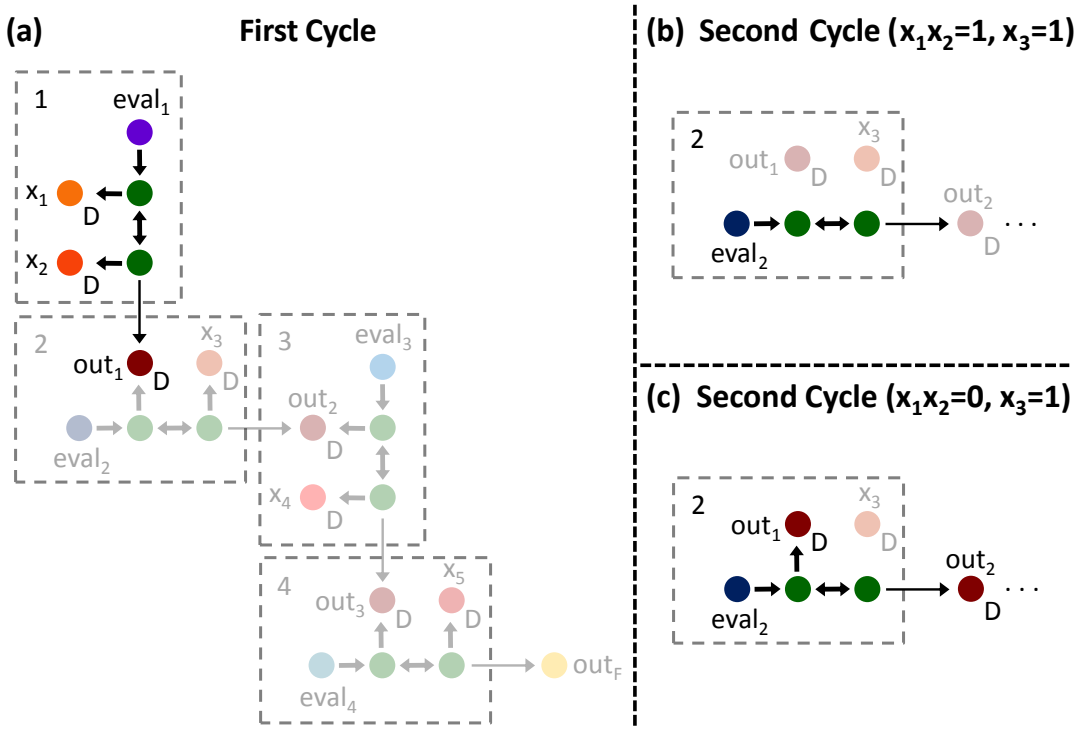

Figure 4.12: The first two cycles for the MEPCL cascade in Figure 4.11. (a) During the first cycle, the first AND gate is pre-charged and evaluated. (b) During the second cycle, x_3 is pre-charged and the second AND gate is evaluated. If x_1x_2 was true, out_1 is in its dark state, and out_2 will undergo a dark transition since x_3 is true. (c) If x_1x_2 was false, out_1 is still available to steal excitons, and out_2 will also remain fluorescent.

MEPCL ensures that excitons do not have to travel the entire length of a RET system to evaluate a complex function. In this AND gate example, the simple cascade (Figure 4.10b) requires excitons to undergo six consecutive RET events, while the MEPCL implementation only requires three consecutive transfer events through any subset of the circuit. Although this difference seems slight, exciton loss scales exponentially with the number of RET steps, and thus, the ability to limit this value regardless of the logic function makes it a powerful tool when building larger systems.

Of course, as illustrated by Figure 4.12, MEPCL trades this exciton loss for a longer computation time. The MEPCL implementation takes roughly four times longer than the simple cascade due to its four separate pre-charge and evaluation cycles. MEPCL should therefore only be used if the exciton loss for the simple cascade lowers the output fluorescence below the minimum observational limit. Interestingly, the simple cascading technique can be used in conjunction with MEPCL to balance a circuit's evaluation time and exciton loss. For instance, the EFD in Figure 4.12 performs only a single AND operation per cycle, however, if the exciton loss is not too high, small cascades can instead be embedded between sets of eval and out fluorophores to increase the computation per stage and lower the total number of cycles. Given the multi-stage nature of MEPCL, it may also be possible to pipeline instructions as long as the appropriate input fluorophores and internal nodes are reset back to their ground state before being pre-charged for the next set of input conditions.

In addition to addressing exciton loss, MEPCL demonstrates that PCL gates are inherently cascadable and do not suffer from increasing energy loss as a function of circuit depth. This is a result of spectral composition of PCL gates, in which input fluorophores are red-shifted from both eval and the mediators, allowing one logic gate's output to act as another logic gate's input. Note that this does not imply that MEPCL cascade lengths are decoupled from the number of unique fluorophores required. In

fact, comparing the two implementations of the AND gate cascade, it's clear that MEPCL designs actually require more distinct fluorophores than simple PCL cascades. In addition to scaling with the number of inputs, MEPCL uses a spectrally distinct eval fluorophore for each stage of evaluation.

It may be possible to overcome this limitation by using only two unique eval fluorophores and alternating them between consecutive stages in an MEPCL cascade. To demonstrate this concept and to provide a slightly more complex MECPL example, we will use the standard full adder circuit shown in Figure 4.13. Similar to the AND gate cascade, translation of the full adder into an MEPCL cascade requires the circuit to first be divided into stages, each of which is assigned an eval fluorophore. We will again embed only a single logic gate in each stage, which splits the full adder into three stages based on the longest path, C_{out}, which has three gate delays. Logic gates are arranged into these stages based on their proximity to their respective output. For example, even though the result of AND2 can be determined in stage one (since both of its inputs are externally applied) it is placed in stage two because it is two gates away from the carry-out, C_{out}. Notice that the sum signal, S, is produced during the second stage, while C_{out} is produced during the third stage. This will also be true for the MEPCL implementation. After partitioning the circuit, each stage is assigned an eval fluorophore. Using the

alternating eval technique, odd stages are assigned $eval_1$ and even stages are assigned $eval_2$.

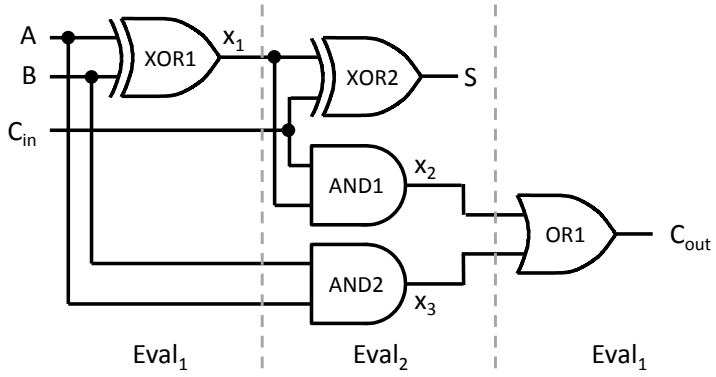

Figure 4.13: A standard full adder broken into three stages. When implemented with MEPCL, each stage is evaluated by the eval fluorophore indicated below the circuit.

Figure 4.14a and b show the corresponding MEPCL cascades for producing S and C_{out} respectively. Both cascades begin with an XOR gate that is evaluated by $eval_1$ and produces the intermediate output x_1. Note that the XOR gate has inline inputs A and B, and thus x_1 must be chosen such that it is more likely to enter the dark state than these inputs during its evaluation phase. Based on the schematic in Figure 4.13, to produce S, x_1 must be fed into a second XOR gate. Since the PCL XOR gate uses two instances of each input fluorophore, x_1 must be physically routed to both of these instances. Figure 4.14a depicts this using a red fluorophore labeled "r" that constructs a homo-RET wire from the first XOR gate to both inputs of the second XOR gate. This fluorophore must be unsusceptible to the dark state, and since it does not have to be externally addressed or observed, it may be reused throughout the design. The circuit for producing C_{out} does

not require these routing fluorophores since x_1 must only be connected to a single mediator in the subsequent AND gate. The C_{out} circuit also illustrates that multiple logic gates may be evaluated in parallel using separate copies of the same eval fluorophore. To generate internal signals x_2 and x_3, for example, both AND gates in the C_{out} circuit are evaluated during the second cycle using different instances of $eval_2$. These internal signals are then fed to the OR gate in stage three, which produces C_{out} on the third and final cycle.

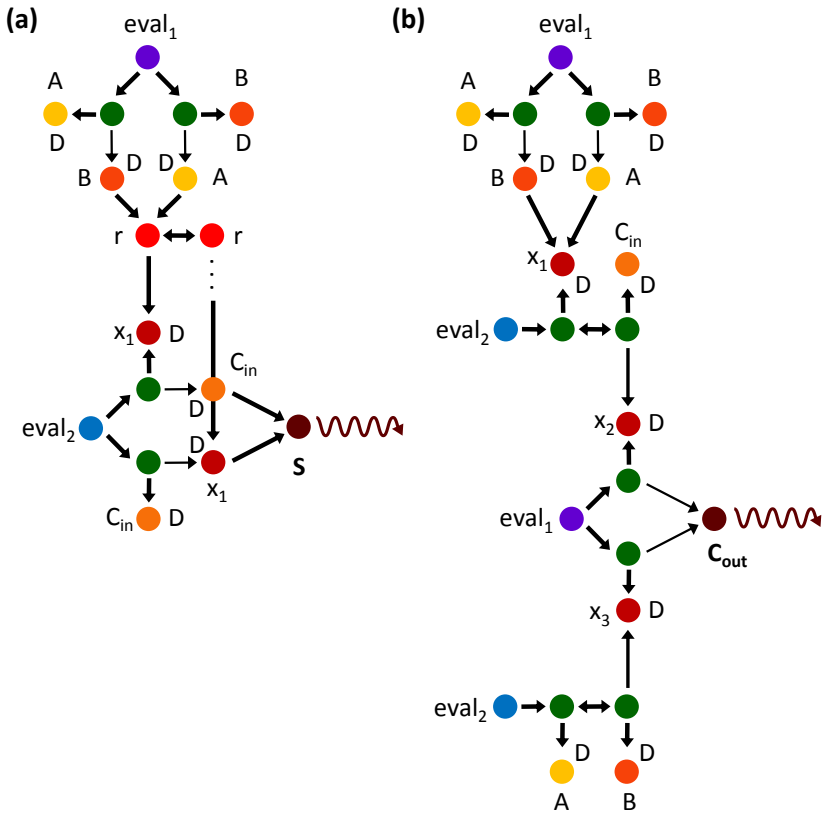

Figure 4.14: (a) Two stage MEPCL circuit producing the sum signal, S. (b) Three stage MEPCL circuit producing the carry-out signal, C_{out}. The final output of each circuit is highlighted with a photon symbol for clarity.

The alternating eval technique requires thorough characterization of the rise and fall times of each device to ensure that adjacent stages do not interfere with one another. For example, in the case of the C_{out} circuit in Figure 4.14b, when exciting $eval_1$ during the first cycle of operation, both copies of this fluorophore (in the XOR gate and the OR gate) will be simultaneously excited. During this cycle, the internal nodes x_2 and x_3 may inadvertently enter their dark states for a subset of the ensemble of MEPCL structures. This unintentional transition can lead to the incorrect evaluation of upstream logic if it does not decay quickly enough. If this alternating eval technique leads to significant interactions between adjacent stages of logic, the use of three distinct eval fluorophores should remedy this issue by ensuring that every MEPCL stage has a full cycle of rest before it must be used.

4.6 Summary

The dark state provides a method for dynamically modulating exciton flow in RET networks. Leveraging this concept, and the ability to localize the dark transition to specific fluorophores, we have developed a new style of RET logic design that offers a library of cascadable logic gates. We have shown two different strategies for cascading these logic gates to implement complex Boolean functions. The second technique, MEPCL, can completely decouple the length of a cascade from both its exciton loss and its energy loss, thereby providing a method for building scalable, complex RET systems.

Thus far, we have outlined the basic design principles of PCL. The remainder of this dissertation focuses on providing evidence that these logic gates function as described. The following chapter explores each PCL gate using CTMC modeling of the underlying RET networks. The results of these simulations corroborate the design rules proposed in this chapter. The subsequent chapter (Chapter 6) provides an experimental demonstration of the PASS gate. This includes its implementation, fabrication, and dynamic operation. These results show that PCL gates can be feasibly fabricated and operate as expected.

5. PCL Modeling

To ensure that the underlying design principles of PCL are sound, we have modeled the logic gates described in the previous chapter using continuous-time Markov chains. CTMCs capture the flow of excitons in RET networks, providing us with the probability of output fluorescence from each device as a function of the input conditions [85].

We begin this chapter with a brief overview of the CTMC representations of RET networks and the parameters used to simulate PCL, e.g. transfer efficiencies, lifetimes, etc. We then provide simulation results for each of the individual logic gates. We discuss how their performance can be improved by modifying the original EFDs proposed in Section 4.3 and how specific transfer efficiencies impact this performance. We conclude with simulations of simple PCL cascades to demonstrate that these networks also function as intended. MEPCL simulations are left as future work due to the inability of these simple models to capture their multi-cycle evaluation.

5.1 Individual PCL Gates

Similar to state machines, RET networks transition between a discrete set of states as a function of time. A simple donor-acceptor pair, for example, when occupied by a single exciton, may exist in, or converge to, any one of the following states shown in Figure 5.1a: excited donor, excited acceptor, donor fluoresces, acceptor fluoresces, donor

non-radiatively decays, and acceptor non-radiatively decays. Transitions between these states depend on the rates of radiative decay, non-radiative decay, and RET between the fluorophores. As pointed out by Wang et al., the time evolution of this state diagram can be accurately described as a continuous-time Markov chain [10]. The solution to this CTMC tells us the probability that the RET network exists in any one of these discrete states as a function of time. Figure 5.1b, for instance, shows the probabilities of the donor and acceptor undergoing radiative and non-radiative decay. Over time, each of these probabilities saturates to a final value, which represents the probability that the exciton ultimately chooses that pathway. The sum of these probabilities converges to one given their exciton consuming nature.

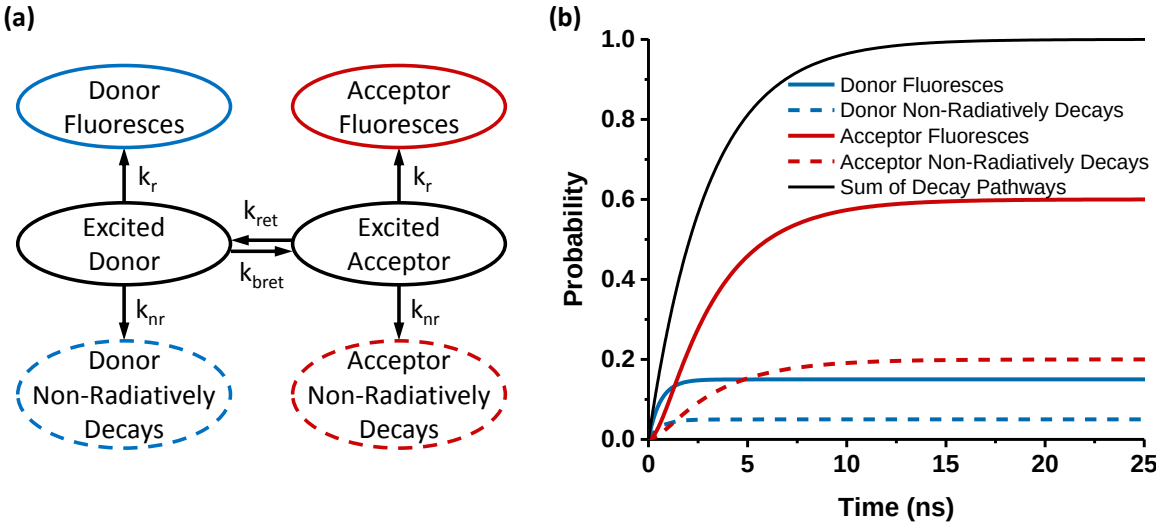

Figure 5.1: (a) A state diagram for a simple donor-acceptor pair. (b) An example of a CTMC solution for the diagram in (a) showing the probability of radiative and non-radiative decay from both the donor and acceptor ($k_r = 2.50e^8\ s^{-1}$, $k_{nr} = 8.33e^7$, $k_{ret} = 1.33e^9$, and $k_{bret} = 0$).

Applying this concept to PCL, we simulated the logic gates in Section 4.3 using CTMC models of each underlying RET network. The solutions to these CTMCs provide us with the probability of fluorescence from every fluorophore in the network. By comparing the output molecule's fluorescence probability for each set of input conditions, we can ensure that input conditions that result in a logical 1 output have a higher probability of producing output fluorescence than input conditions that result in a logical 0 output, i.e. that every device performs the proper Boolean operation.

To test the design principles of PCL without focusing on the implementation of each logic gate, i.e. fluorophore assignments, fluorophore coordinates, etc., we first established the transition rate matrices for these devices based on the following assumptions. Transfer efficiencies were set to conservative values achievable by real systems: 10% and 90% for low and high values respectively. For the sake of simplicity, all fluorophores were assumed to have a lifetime of 3 ns and a quantum yield of 75%. Using Equation 5.1, we calculated the rate of RET between each fluorophore. This equation relates the transfer efficiency (Φ_T) and the donor lifetime (τ_D) to the RET transfer rate (k_{RET}). We also calculated the rates of radiative (k_r) and non-radiative (k_{nr}) decay for each fluorophore using Equation 5.2 and Equation 5.3 respectively, where Φ_F and τ are the fluorophore's quantum yield and lifetime respectively. After establishing the transition rate matrices, we numerically solved each CTMC starting with an initially

excited eval and monitoring the probability of output fluorescence from each device. To test various input conditions, transfer rates into and out of dark fluorophores were set to zero (thereby removing them from the network), and the CTMC was re-solved.

$$k_{RET} = \frac{\Phi_T}{\tau_D(1 - \Phi_T)} \quad \text{Equation 5.1}$$

$$k_r = \frac{\Phi_F}{\tau} \quad \text{Equation 5.2}$$

$$k_{nr} = \frac{1}{\tau} - k_r \quad \text{Equation 5.3}$$

Figure 5.2 summarizes the CTMC results by plotting the probability of output fluorescence (P(F)) for every input condition. For each PCL gate, the probability of fluorescence is much higher for expected logical 1 outputs than for expected logical 0 outputs, confirming that every device performs the correct operation. The results also demonstrate the nonlinearity of PCL gates. The AND gate, for example, has a minimum on/off ratio of ~5.5 compared to the value of ~1.8 for its linear counterpart (in Section 2.3.3). This value can be even further improved using methods described in the Section 5.2. Gates that only rely on inline inputs to turn certain RET pathways off, e.g. NAND, NOR, and NPASS, exhibit infinite on/off ratios due to their complete removal of RET pathways when outputting a logical 0. When physically implemented, these on/off ratios will take on finite values determined by either undesirable RET pathways, e.g. direct

transfer from eval to out, or simply by noise, e.g. ambient light or the detector's dark current.

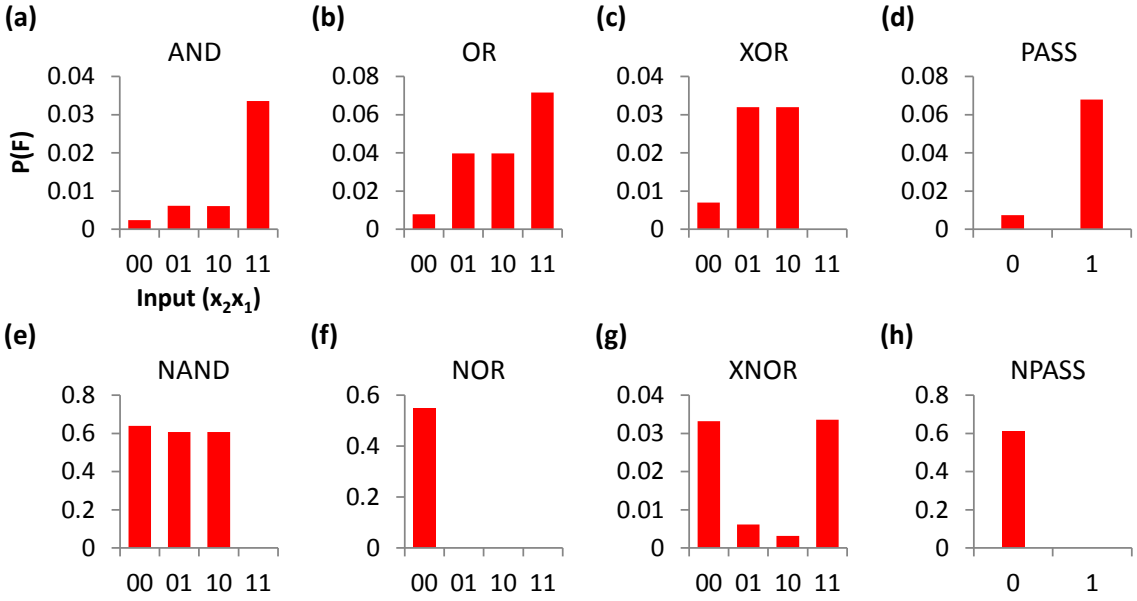

Figure 5.2: Output fluorescence probabilities for all input combinations of the (a) AND, (b) OR, (c) XOR, (d) PASS, (e) NAND, (f) NOR, (g) XNOR, and (h) NPASS PCL gates.

It should be noted that the results of these simulations do not depend on the fluorescence lifetime chosen earlier. Although this parameter influences the transition rates in each CTMC, when applied to all fluorophores, it merely changes the time required for the probability of each state to saturate. Similarly, increasing the quantum yield increases the absolute probabilities shown in Figure 5.2, but it does not change the relative on/off ratios of each device, i.e. the output fluorescence scales uniformly for all input conditions.

5.2 Gate Optimizations

The performance of PCL gates using mediator-input pairs, e.g. AND, OR, and PASS, can be improved by modifying the basic designs simulated above. Similar to the C-DEV (see Section 2.3.3), the on/off ratios of these gates depend nonlinearly on the number of mediator-input pairs between eval and out. With each additional pair, the probability that an exciton makes it from eval to out diminishes exponentially due to their serial layout. To demonstrate this concept, we varied the number of mediator-input pairs from 1 to 10 in both the PASS gate and in each parallel path of the OR gate (Figure 5.3a and b). Using the transfer efficiency, lifetime, and quantum yield parameters assumed earlier, we extracted the on and off fluorescence probabilities from each EFD. When measuring the on state fluorescence values for the OR gate, which produces a logical 1 under three different input conditions, we used the worst case condition in which only one input is applied.

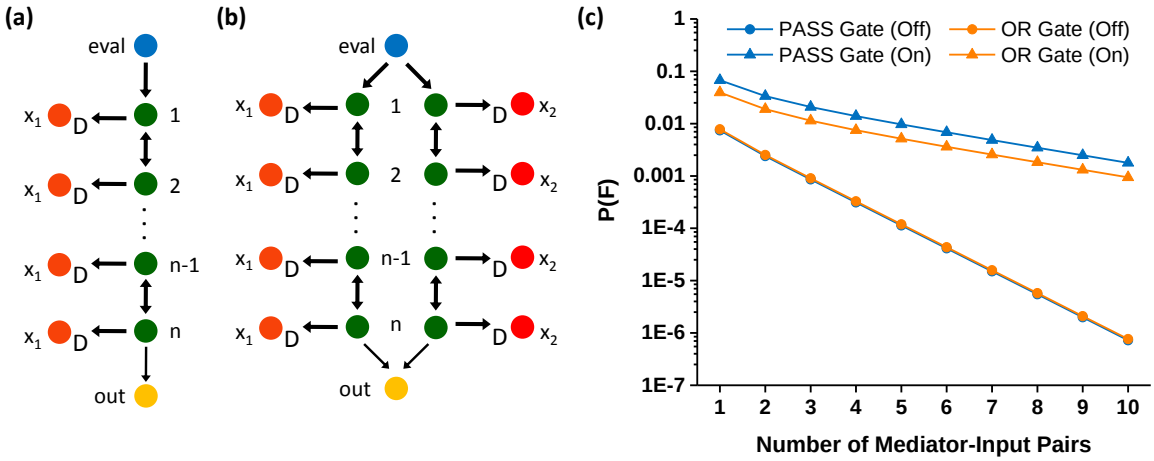

Figure 5.3: (a) A PASS gate with *n* mediator-input pairs. (b) An OR gate with *n* mediator-input pairs. (c) Output fluorescence probabilities from the on and off states of the PASS gate and OR gate as a function of the number of mediator-input pairs.

The results in Figure 5.3c indicate that as the number of mediator-input pairs increases, both the on and off fluorescence probabilities decrease. This agrees with the intuition that the end-to-end transfer efficiency of both devices should decrease exponentially with length, and therefore so should the probability of output fluorescence. The on state fluorescence, however, decreases at a substantially slower rate than the off state fluorescence due to the removal of the input fluorophores and their associated absorbing states. Thus, the overall on/off ratio increases, as shown in Figure 5.4. A PASS gate with five additional mediator-input pairs, for example, exhibits an ~18 fold improvement over the basic one mediator-input design. This improvement, of course, must be weighed against the increasing exciton loss. Designers should choose

logic gates with the highest on/off ratios possible that still produce an acceptable amount of on state fluorescence.

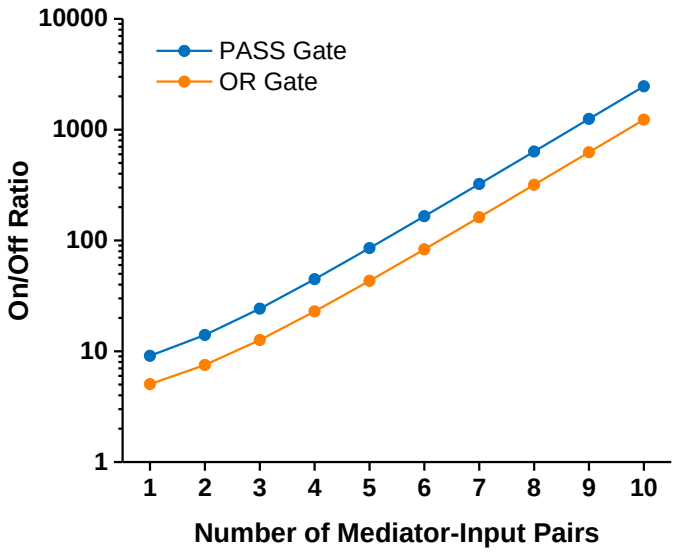

Figure 5.4: The on/off ratio for PASS and OR gates as a function of the number of mediator-input pairs.

The performance of PCL gates using mediator-input pairs also strongly depends on the mediator-to-input and the mediator-to-output transfer efficiencies, which have thus far only been set to 90% and 10% respectively. Transfer from the mediator to the input should be as high as possible so that input fluorophores can efficiently steal excitons. Conversely, transfer from the mediator to the output, or any downstream fluorophore, should be kept as low as possible (while still providing observable output fluorescence) to avoid interfering with this exciton sinking process.

Figure 5.5 illustrates the effects of this design space on the on/off ratio for a PASS gate with only a single mediator-input pair. In this example, the eval-to-mediator

transfer efficiency was set to 90% while the mediator-to-input and mediator-to-output efficiencies were varied. Even with only a single mediator-input pair, the on/off ratio approaches 100 for designs with high mediator-to-input (99%) and low mediator-to-output efficiencies (1%). This is more than an order of magnitude greater than the basic design proposed. Similar to adding additional mediator-input pairs, however, lowering the mediator-to-output efficiency will decrease the on state fluorescence and thus, this exciton loss must be considered when choosing the appropriate design.

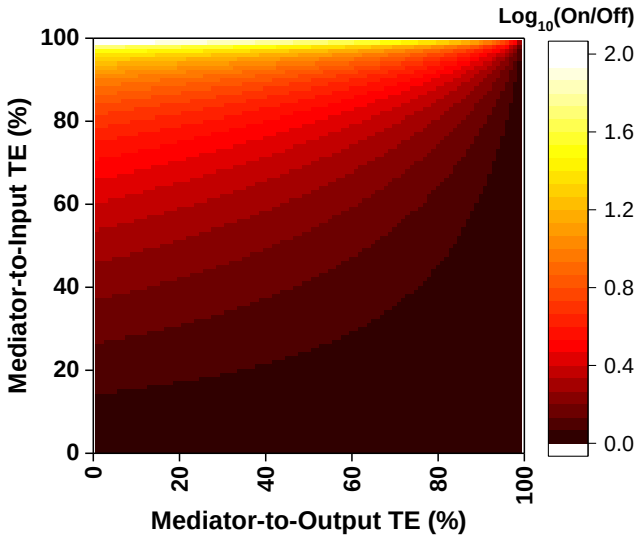

Figure 5.5: The on/off ratio for a PASS gate with a single mediator-input pair as a function of both the mediator-to-input and mediator-to-output transfer efficiencies.

5.3 Additional Fluorophore Interactions

The PCL EFDs modeled thus far are simple. Fluorophore interactions are limited to only those necessary for performing the intended Boolean operation. When

implemented with real fluorophores, however, some of these devices may exhibit additional RET pathways due to the proximities of each molecule and their spectral overlap with one another. To demonstrate the effects of some of these pathways, we will use the modified PASS gate EFD shown in Figure 5.6. In this diagram, the original RET pathways of the PASS gate are depicted in black, while the new pathways are highlighted with three different colors. These three additional RET paths are eval-to-input, eval-to-out, and out-to-input transitions. Each of these paths involves a blue-shifted donor and a red-shifted acceptor, and may therefore occur in a real system simply due to the spectral overlap requirements of RET. The efficiency of these transitions will ultimately depend on the fluorophores chosen and their spatial coordinates.

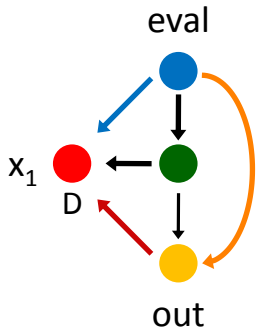

Figure 5.6: A PASS gate EFD illustrating additional RET pathways (in color) that may be present when implemented with real fluorophores. Original PASS gate pathways are shown in black.

To observe the effects of these additional pathways, we set the transfer efficiencies in the original PASS gate EFD to the values assumed earlier (90% and 10%

for high and low values respectively). We then varied the transfer efficiency of each new pathway independently. For each EFD, we extracted the on/off ratio, which is shown in Figure 5.7.

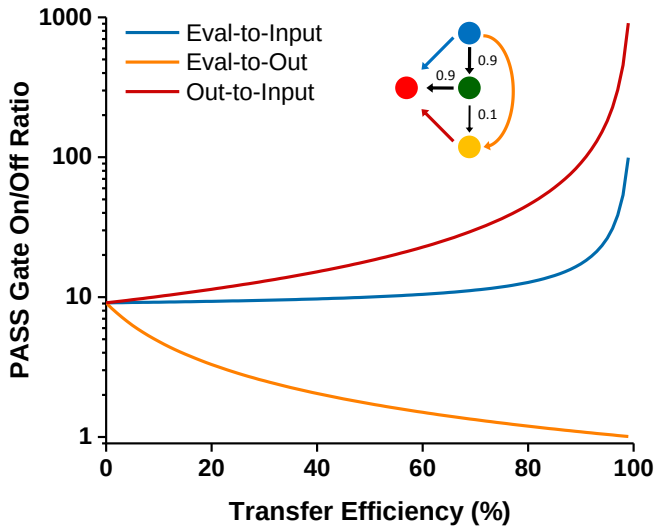

Figure 5.7: The dependence of the PASS gate's on/off ratio on the additional RET pathways shown in Figure 5.6. The static values of the original PASS gate EFD are shown in the inset.

These results reveal a number of interesting trends. The eval-to-out path decreases the performance of the PASS gate as the efficiency of this transition increases. This pathway allows excitons to skip the mediator altogether, bypassing the input fluorophore and increasing the output fluorescence from both the on and off state. As it becomes the dominating pathway, the on and off fluorescence probabilities asymptotically approach the same value, resulting in an on/off ratio of one. The performance of all PCL gates will be negatively affected by this transition, and thus

interactions between these two fluorophores should be minimized. Ideally, eval and out will be spectrally and spatially separated enough such that this transition is easily avoided.

The two remaining RET pathways in Figure 5.7, eval-to-input and out-to-input, have the opposite effect of eval-to-out. These transitions enhance the performance of the PASS gate by providing additional exciton stealing opportunities in the off state, which lowers the off state fluorescence without affecting the on state fluorescence. This trend applies to all PCL gates using mediator-input pairs to sink excitons. It's also worth noting that when implemented with real fluorophores, the out-to-input pathway is more likely to occur than the eval-to-input pathway. This is because the eval and output fluorophores have a larger spectral separation simply based on the EFD of the PASS gate.

5.4 Simple PCL Cascade Results

Given that individual PCL gates function as intended, we now turn our attention towards verifying the design principles of simple PCL cascades (described in Section 4.4). Using this cascading technique, individual PCL gates are connected to one another by one or more chains of mediators wired to a single pair of eval and out fluorophores. Figure 5.8a depicts one such example, which implements the function $out=x_1x_2(x_3+x_4)$ by serially cascading an AND and an OR gate. To demonstrate that this PCL cascade

performs the intended function, and that its performance depends on the transfer efficiencies explored earlier, we modeled this EFD using two sets of high and low transfer efficiencies: 90%, 10% and 95%, 5%. Figure 5.8b shows the normalized output fluorescence probabilities from each of these models. Both implementations function as designed, with input conditions 0111 ($x_4x_3x_2x_1$), 1011, and 1111 resulting in a significantly higher probability of fluorescence than all other input conditions. The 95%/5% model outperforms the 90%/10% model by offering lower relative logical 0 outputs. Just as with individual logic gates, PCL cascade performance improves when the transfer efficiencies of exciton sinking pathways are much higher than the other competing pathways.

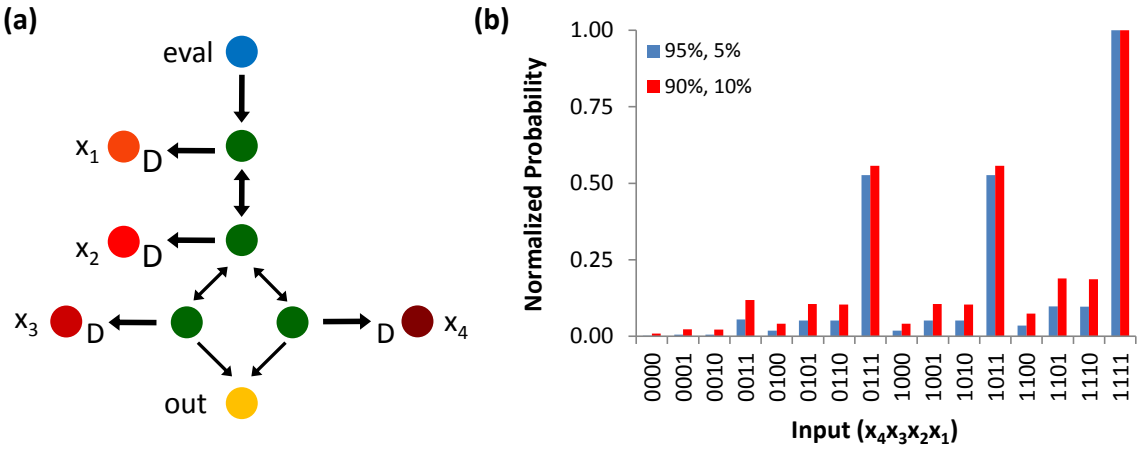

Figure 5.8: (a) A serial PCL cascade implementing out=$x_1x_2(x_3+x_4)$). (b) Normalized output fluorescence probabilities from the cascade in (a) for all input conditions based on two different transfer efficiency models.

In addition to simulating this serial cascade, we have also modeled the simple parallel cascade shown in Figure 5.9a. This structure places two AND gates in parallel

such that out=$x_1x_2+x_3x_4$. The results of this CTMC simulation are shown in Figure 5.9b using the same sets of transfer efficiencies described above. Every input condition belonging to the implicants XX11 and 11XX have a significantly higher output fluorescence probability than the other input conditions. Similar to the first cascade, the relative ratio of logical 1 and logical 0 outputs is higher for the 95%/5% model than the 90%/10% model.

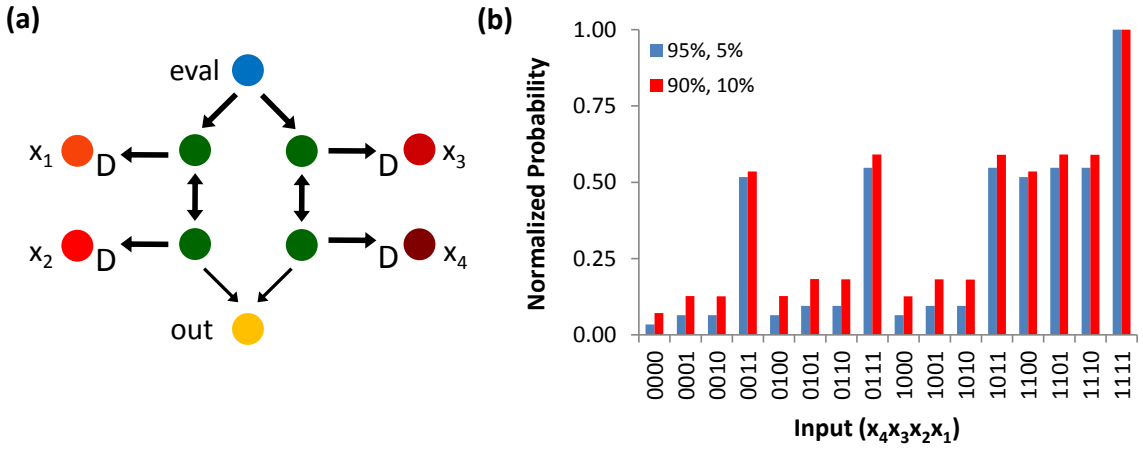

Figure 5.9: (a) A parallel PCL cascade implementing out=$x_1x_2+x_3x_4$. (b) Normalized output fluorescence probabilities from the cascade in (a) for all input conditions based on two different transfer efficiency models.

Each simple PCL cascade acts as a single RET network, which allows it to be accurately described by a basic CTMC model. The multi-stage evaluations used by MEPCL cascades, however, require independent RET networks to interact with one another at the proper times. Thus, in order to evaluate MEPCL, an appropriate model must be developed that accounts for time required for ensembles of logic gates to

transition between different states. Given that this requires thorough characterization of real PCL gates implemented with commercially available fluorophores, we leave MEPCL simulations as future work.

5.5 Summary and Future Work

Using CTMC models we have demonstrated that the underlying design principles of the PCL work as proposed. We have shown that simple modifications to the original EFDs can drastically improve the on/off ratios of these devices, albeit for slightly lower exciton throughputs. We have explored how the various transfer efficiencies in these RET networks affect PCL device performance, which provides insight regarding the implementation of these devices in the future. Lastly, we have shown that simple PCL cascades perform their intended functions, confirming that PCL can be used to implement complex Boolean logic.

The most pressing future work regarding PCL simulations is to verify the operation of MEPCL cascades. Although we have shown that the individual components function properly, the multi-cycle evaluation required by MEPCL must be explored by a model that captures the rise and fall times from ensembles of devices. That will allow for an exploration of the timing requirements for this cascading technique based on the interactions of individual logic gates.

In addition to modeling MEPCL cascades, we leave the evaluation of PCL devices under multi-exciton conditions as future work. As explained in Section 5.1, the simple CTMC models used throughout this chapter describe the probability of fluorescence from each EFD based on a single exciton transitioning through the RET network. To capture the presence of multiple excitons, the simple state diagrams must be modified to include additional multi-exciton states and their associated transitions. Alternatively, if the networks are kept small, as is the case for single PCL gates, multi-exciton effects might be studied using the Simulation of Chromophore Interactions using Monte Carlo methods and Markov chains Model (SCIMM) [29].

With the design principles of PCL validated by simulation, the next step towards building large-scale systems is to confirm that these logic gates can be feasibly implemented. The following chapter supports this with experimental evidence of a working PASS gate.

6. PCL PASS Gate Demonstration

The simulation results in the previous chapter indicate that PCL gates function as intended. These simulations, however, assume that the proposed EFDs can be feasibly implemented and that the input fluorophores successfully transition into and out of their dark states when assembled on the underlying DNA nanostructure. To confirm that these assumptions are valid, we now provide an experimental demonstration of the PCL PASS gate, chosen as a proof-of-concept device for its adherence to PCL operating principles with a minimal set of design requirements.

We begin this chapter with a short review of the PASS gate and its operating principles. We then describe the design and layout of our particular implementation on the DNA cross motif described in Section 2.3.4. Using steady-state fluorescence measurements from an ensemble of PASS gates, we determine the maximum on/off ratio of this particular implementation. We then use time-resolved fluorescence to demonstrate the pass gate's ability to dynamically toggle between states, characterizing the associated rise and fall times of these transitions. While there is certainly room for improvement in its implementation, the PASS gate provides substantial evidence that the operating principles of PCL gates are valid.

6.1 Gate Design and Layout

Originally described in Section 4.3, the PCL PASS gate consists of four unique fluorophores: eval, mediator, input, and out. Given its single input fluorophore, this logic gate exists in one of two states: off or on. In the off state (Figure 6.1a), the input fluorophore acts as a RET acceptor, stealing excitons as they propagate from eval to out. This results in weak output fluorescence, interpreted as a logical 0. In the on state (Figure 6.1b), the input fluorophore is placed in its dark state, allowing excitons to flow unhindered from eval to out. Accordingly, the on state is characterized by high output fluorescence, interpreted as a logical 1. The pass gate can be reversibly toggled between these two states. To transition from off to on (low-to-high), the input fluorophore is directly excited by a high intensity source until it enters its dark state. To transition from on to off (high-to-low), this direct excitation is removed and the input fluorophore spontaneously returns to it ground state. As mentioned in Section 4.1, this transition can be forced by UV illumination (although not demonstrated in this chapter) if constructed with the proper fluorophores.

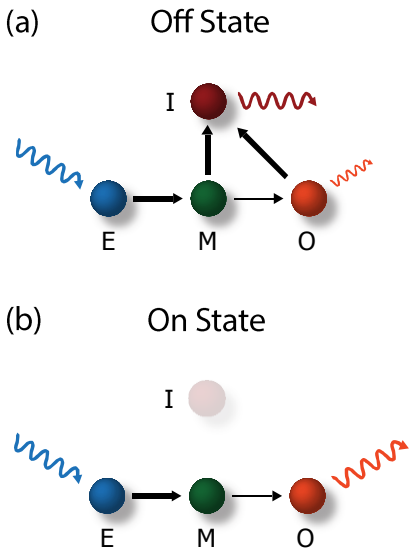

Figure 6.1: EFDs for the (a) off state and (b) on state of the pass gate, consisting of the eval (E), mediator (M), out (O), and input (I) fluorophores.

The EFD in Figure 6.1 uses the fewest number of fluorophores for implementing the PASS gate and was chosen accordingly for the experiments described in this chapter. Notice that we have included transfer from the output to the input, given its ability to substantially increase the on/off ratio for this simple implementation (see Section 5.3). As mentioned in Section 5.2, the nonlinear response of this device can also be greatly improved by increasing the number of mediator-input fluorophore pairs between eval and out; however, for the sake of starting with a simple experimental demonstration, we have opted to only use a single pair.

Correct operation of the PASS gate heavily depends on the proper choice of fluorophores for each terminal of the device. In addition to forming a hetero-RET wire, the eval, mediator, and output fluorophores must be chosen such that they are strongly,

if not completely, resistant to a dark transition when excited in the presence of the desired reducing agent (MEA for these experiments). If this condition is not satisfied, these molecules may spontaneously enter a dark state after receiving an exciton and disrupt the proper operation of the logic gate. To ensure this localization of the dark state, we chose Cy2, Cy3, and Texas Red (TR) as eval, mediator, and output respectively. Given their use as activator fluorophores in buffers containing thiolated reducing agents, both Cy2 and Cy3 have been indirectly characterized as generally resistant to dark transitions [66, 67]. While TR has been studied to a lesser extent in this context, we hypothesized that it would also remain fluorescent in the presence of MEA due to its characterization as a weak photoinduced electron acceptor and the evidence that reduction by MEA is responsible for many dark state transitions [65, 75, 86].

In contrast to the other three fluorophores, the input fluorophore must be susceptible to entering a dark state. Ideally, this transition is a low probability event, e.g. a reduced triplet or a process with a similarly low yield [65]. This ensures that the fluorophore undergoes many excitation cycles before successfully entering its dark state. If this requirement is not met, excitons starting at eval and traveling into the input fluorophore may unintentionally toggle the PASS gate on. This will still happen occasionally given the probabilistic nature of the device; however, it can largely be avoided for an ensemble of devices if the transition probability and the evaluation

intensity are kept low. When choosing an input fluorophore, we also intentionally avoided dyes that require an oxygen scavenging system to access their dark state [74, 87]. These systems complicate the buffer, and the necessity of an oxygen-free microenvironment places restrictions on the computational domains compatible with RET logic. In addition to these dark state requirements, the excitation spectrum of the input fluorophore must be red-shifted with respect to all other fluorophores comprising the device. This allows the input to act as an acceptor to both the mediator and output, providing more exciton stealing opportunities and lowering the total output fluorescence from the off state. It also ensures that when the input is directly excited during the low-to-high transition, these excitons do not travel into the output fluorophore and contribute to the output fluorescence (making it more difficult to experimentally observe this transition). Based on these requirements, we chose ATTO 680 (AT680) as the input.

After selecting suitable fluorophores, we mapped the locations of each molecule to conjugation sites on the DNA nanostructure shown in the subset of Figure 6.2. This particular motif was originally designed with the intention of forming aperiodic, hierarchically assembled DNA lattices for computational systems, making it a reasonable first choice as the PASS gate's substrate [40, 41]. Before settling on the design depicted in Figure 6.2, a variety of fluorophore layouts were considered. Each design

was evaluated using a custom layout tool (described in Appendix B.2), which estimated the transfer rates between fluorophores based on their published fluorescence properties and their intermolecular distances (assuming an orientation factor of 2/3 for all RET pairs). These transfer rates, along with the radiative and non-radiative decay rates, were then translated into a CTMC, which was numerically solved to obtain the probability of output fluorescence [10]. To simulate the on and off states, two separate CTMCs were evaluated for each layout, one with the input present and one without (much like the simulations described in the previous chapter). Only designs in which adjacent fluorophores were spaced at least 1.5 nm apart were considered so as to avoid contact quenching and/or operation outside of the Förster region.

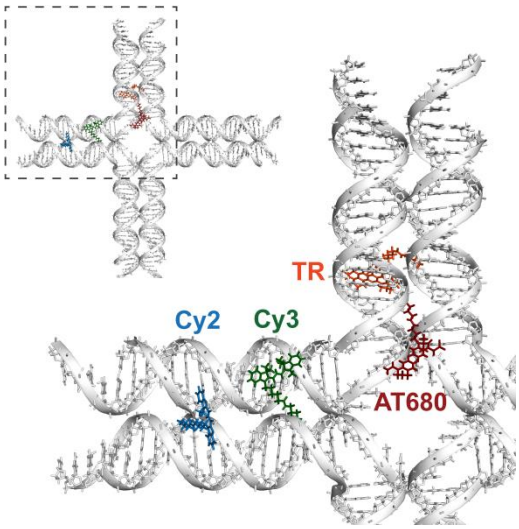

Figure 6.2: Layout of the pass gate on a DNA nanostructure. Fluorophores are arranged in the top left corner of the nanostructure, shown in its entirety in the inset. Note, this diagram is meant for visualization purposes only and does not accurately depict the orientation of the fluorophores after assembly.

When comparing designs, we primarily sought to optimize the on/off ratio of the PASS gate. Devices with high on/off ratios exhibit large changes in output fluorescence when transitioning between states, making it easier for us to confirm working operation of the PASS gate. Furthermore, the numerator and denominator of this metric have important implications when cascading these devices to build more complex systems in the future. Devices with higher on state fluorescence can form longer RET cascades since the output exciton flux can withstand a greater number of downstream transfer events before diminishing below an observational threshold. Devices with lower off state fluorescence are less likely to incorrectly evaluate downstream logic since this fluorescence should ideally be null. It should be noted that our layout tool only provides a rough estimation of this on/off ratio since it cannot predict the exact location or dipole orientation of each fluorophore, both of which significantly influence the on/off ratio due to the device's nonlinear dependence on certain transfer efficiencies. Thus, this tool and the estimations it provided were merely used to guide our design process.

6.2 Fabrication and Static Analysis

To fabricate the PASS gate, fluorophores were conjugated to their respective strands and purified using HPLC (see Appendices A.2.3-A.2.5 for details). Labeled strands were mixed with the remaining unlabeled strands of the DNA cross motif and the structures were annealed from 96°C to 4°C at a concentration of 1 uM in a 1X TAE

buffer containing 12.5 mM Mg^{++} to facilitate assembly. To verify that both states of the PASS gate function as designed, two separate versions of the device were constructed: one containing all four fluorophores and one without the input fluorophore. MEA was not added to either sample. The first structure represents a device permanently stuck in the off state since the input fluorophore cannot transition to its dark state without the reducing agent present. Conversely, the second structure represents a device permanently stuck in the on state since the input fluorophore is not included and therefore cannot steal excitons.

Figure 6.3 shows the fluorescence spectrum from each structure when the eval fluorophores (Cy2) are directly excited at 450 nm. Both spectra contain fluorescence peaks from all constituent fluorophores, confirming that excitons are properly routed through each RET network and that the structures assembled correctly. A qualitative comparison of the two spectra shows that the emission from the output region (at 610 nm from TR) is greater from the on state than the off state, validating the design principles of the device. Furthermore, the lower output fluorescence from the off state is accompanied by the appearance of an AT680 fluorescence peak centered at 700 nm. This confirms that the input (AT680) is indeed stealing excitons and is responsible for the spectral differences. Interestingly, we do not observe any quenching of the mediator (Cy3) by the presence of the input. Although this result is unexpected given the

proximity of these two dyes, it does not prevent proper operation of the PASS gate since our design relies more heavily on the input fluorophore quenching the output than the mediator. We believe that this lack of transfer may be due to the relative orientations of the dyes. Additional work is required to test this hypothesis.

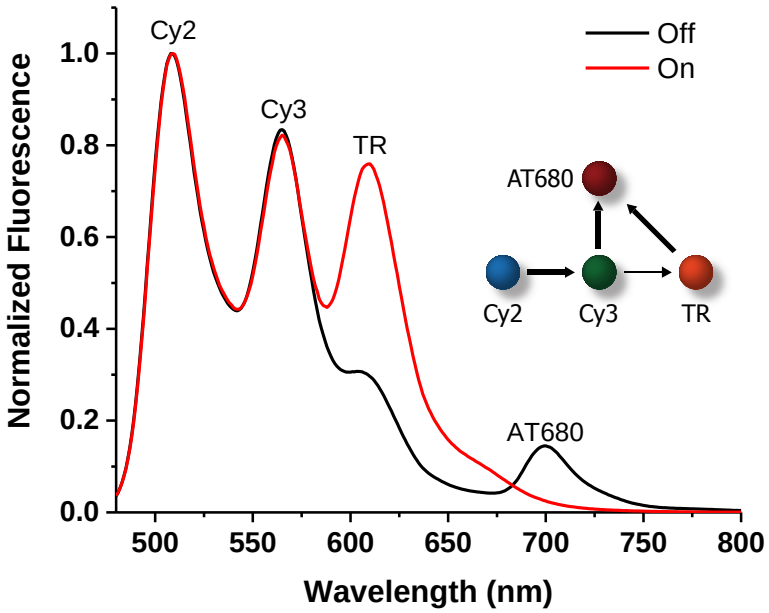

Figure 6.3: Fluorescence spectrum of the PASS gate assembled with (Off) and without (On) the input fluorophore when excited at 450 nm.

A quantitative comparison of the spectra in Figure 6.3 at 610 nm indicates that the on/off ratio for the PASS gate is ~2.6. This value, however, is misconstrued by the mediator's fluorescence overlap with the output's emission, illustrated below in Figure 6.4.

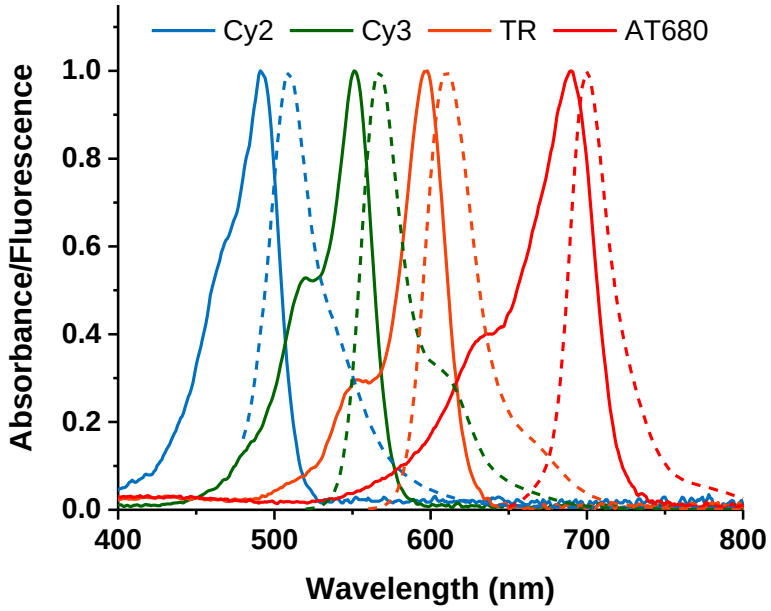

Figure 6.4: Absorption (solid lines) and emission spectra (dotted lines) for Cy2, Cy3, TR, and AT680.

To extract the actual on/off ratio for this device, we determined the contributions from each fluorophore using a linear least squares fitting of the sum of the individual spectra to the normalized total fluorescence. This decomposition, shown in Figure 6.5, reveals that the output's fluorescence contribution in the on and off state is 0.52 and 0.06 respectively, indicating that the actual on/off ratio for this device is ~8.7 even though it cannot be directly observed.

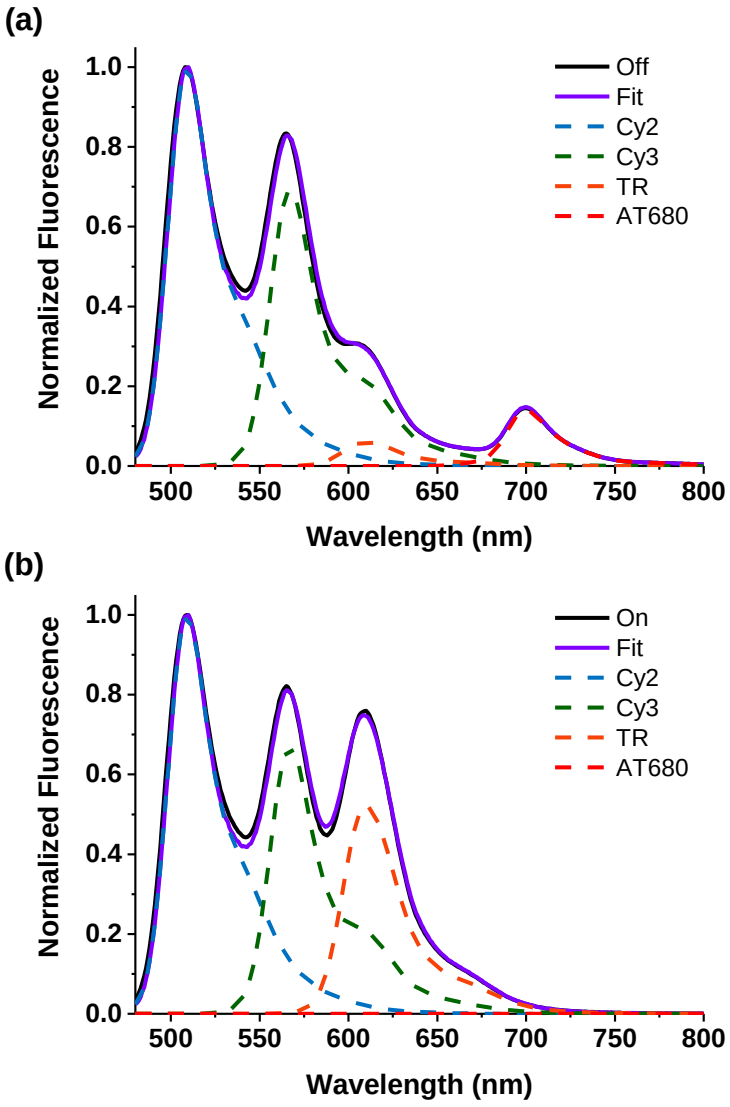

Figure 6.5: (a) Fluorescence decomposition of the off state. The fluorescence coefficients for Cy2, Cy3, TR, and AT680 are 1.00, 0.69, 0.06, and 0.14 respectively. (b) Fluorescence decomposition of the on state. The fluorescence coefficients for Cy2, Cy3, TR, and AT680 are 1.00, 0.67, 0.52, and 0.00 respectively.

Working operation of the on and off states was further corroborated by TCSPC measurements. Eval was excited in each sample at 490 nm and emission from the spectral region of the output was collected at 610 nm. The resulting time-resolved fluorescence in Figure 6.6a is a multi-exponential, again due to the mediator's fluorescence overlap with the output. Both samples contain a short and long lifetime component, which can reasonably be attributed to Cy3 and TR respectively given the large difference in these dyes' lifetimes (typically 1.5–1.8 ns for Cy3 and 3.2–3.6 ns for TR) [88]. A simple comparison of these measurements clearly shows that fluorescence in this spectral region is more heavily quenched in the off state than the on state. Furthermore, if we divide the total number of photons collected during the individual TCSPC measurements of each state (Figure 6.6b), we find that the observable on/off ratio is ~2.4, which agrees with the steady-state fluorescence results.

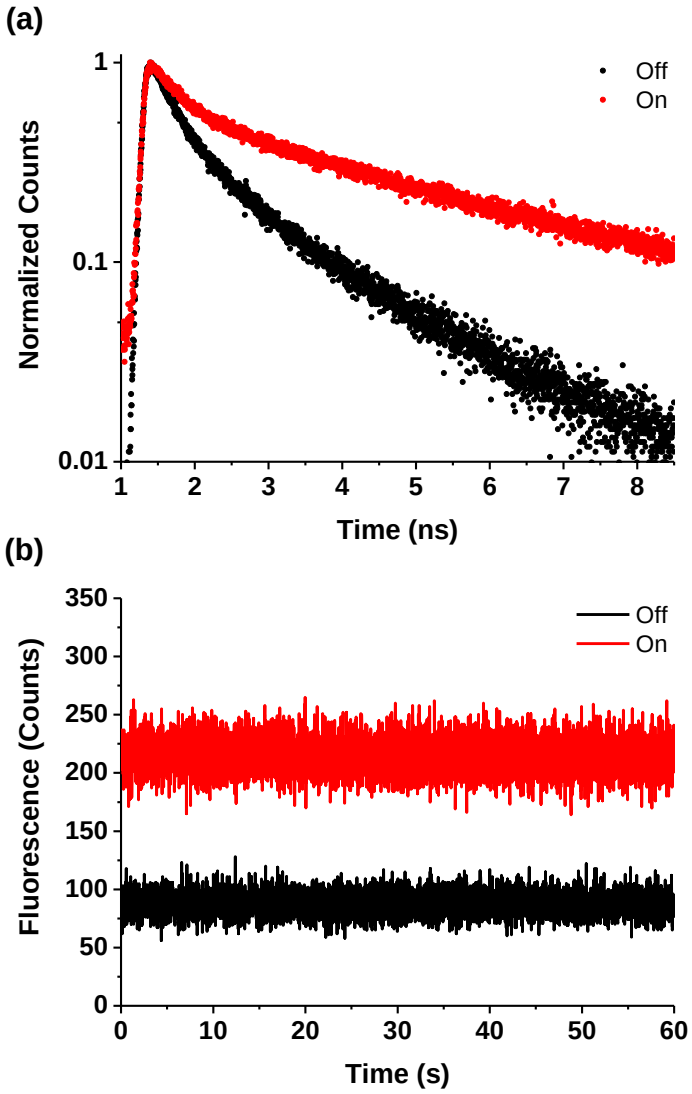

Figure 6.6: (a) Normalized TCSPC measurements from the output's spectral region (610 nm) when the permanently on and off states are excited at 490 nm. (b) Fluorescence time traces recorded during the TCSPC measurements in (a).

6.3 Dynamic Analysis

After ensuring that the individual states of the PASS gate function correctly, we tested the device's ability to dynamically transition between states. MEA was added to the PASS gate's buffer at a concentration of ~100 mM. The device was then excited at 490 nm and the output fluorescence was monitored at 610 nm. To toggle the device on and off, the sample was irradiated with a 670 nm laser that directly excites the input fluorophore. This excitation source was manually shuttered at ~1 minute intervals to observe consecutive transitions between the on and off states. To verify that successful switching of the PASS gate depends on the input fluorophore's dark transition, we compared the resulting fluorescence time trace to that of a control PASS gate sample at the same concentration but without MEA present.

As shown in Figure 6.7, when the MEA-containing sample is excited at 670 nm, fluorescence from the output region increases by ~16%. When this excitation is removed, input fluorophores return to their ground state and fluorescence from the output region decreases back to its original level, albeit at a slightly different final value due to fluctuations in the 490 nm laser power. The control sample does not exhibit any change in output fluorescence when irradiated at 670 nm, indicating that the MEA, and therefore AT680's dark state, is responsible for the switch-like behavior. This result also

eliminates saturation as a possible modulation mechanism since saturation of the input fluorophore would elicit a switching response from the control sample.

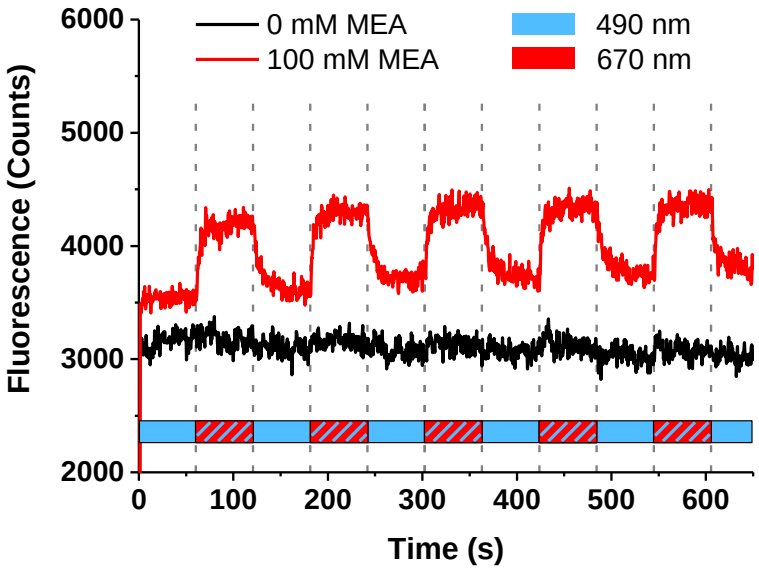

Figure 6.7: Output fluorescence from the PASS gate with and without MEA present while toggling the device on and off with 670 nm irradiation. Eval is constantly excited at 490 nm and fluorescence from the output is monitored at 610 nm.

In addition to this control, we verified that extra 670 nm scatter due to the MEA is not responsible for the increase in fluorescence signal. Although trivial and unlikely, this must be ruled out since the extra scatter would only be present when the output fluorescence is expected to rise, thereby potentially generating a false positive. We tested this by subjecting each buffer (1X TAE Mg^{++} with and without 100 mM MEA) to the same 490 nm and 670 nm excitation conditions and measuring the resulting scatter. Figure 6.8 demonstrates that although there is some additional scatter due to the 670 nm beam (20 or fewer counts per 0.5 second time bin), this scatter is not influenced by the

presence of MEA. Furthermore, Figure 6.8 illustrates that a change due to scatter is instantaneous, while the change in fluorescence from the PASS gate has a clear rise and fall time.

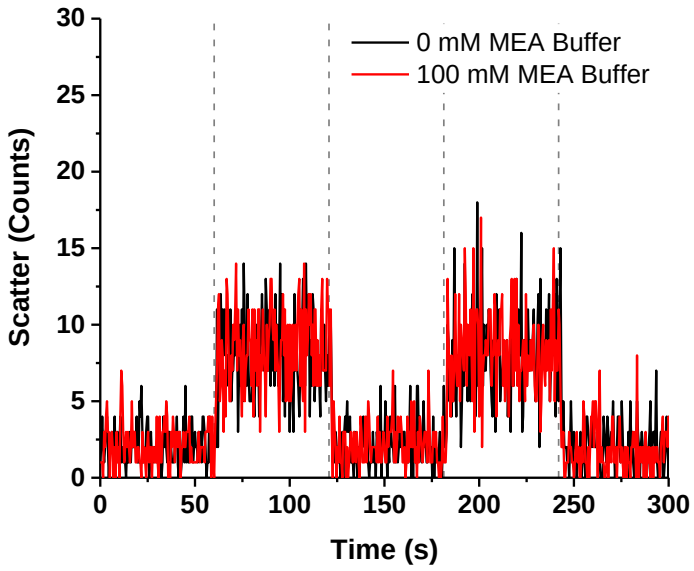

Figure 6.8: Scatter recorded from buffers with and without MEA when the 670 nm excitation source is toggled on and off during continual irradiation at 490 nm. The scatter is monitored at 610 nm.

An analysis of the first five switching events for five different PASS gate samples indicates that the maximum observable dynamic on/off ratio is 1.16 ± 0.02 (standard deviation) given our current switching conditions. We determined this on/off ratio for each switching cycle by dividing the average on state fluorescence by the average off state fluorescence using the 10 consecutive data points preceding each transition (labeled $\Delta t_{on/off}$ in Figure 6.11). This on/off ratio, however, depends on the 670 nm excitation intensity. To demonstrate this, we varied the driving current for the 670 nm

laser diode from 500 mA to 800 mA (the driving current used in the previous measurements) in increments of 100 mA. Two fluorescence time traces were recorded for each current setting and the two measurements were averaged to reduce the noise. As shown in Figure 6.9, increasing the input excitation intensity increases the on/off ratio. This observation agrees with the intuition that the leveling-off of the on state fluorescence represents an equilibrium between the creation and destruction of dark input fluorophores, the former of which is a function of the excitation intensity [65, 72]. It also implies that there may be a simple route towards increasing the dynamic on/off ratio in the future, as the beam width of our gate excitation was intentionally designed to overfill our sample volume, ensuring full illumination and avoiding multi-beam alignment issues (see Section A.3.2 for a diagram of the optical setup).

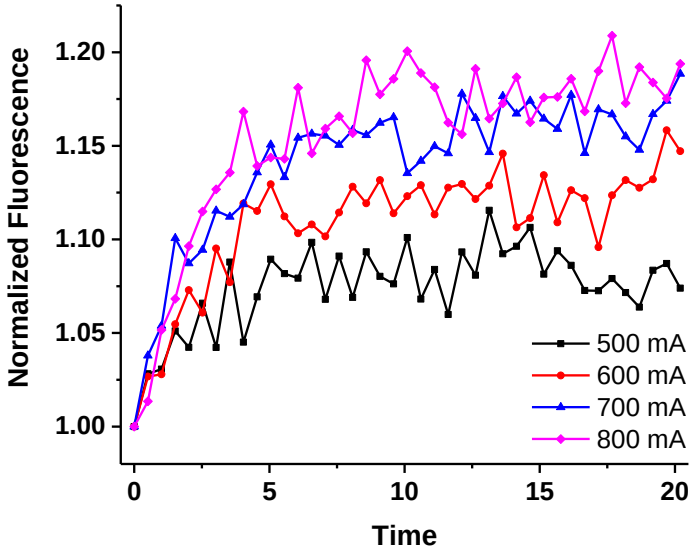

Figure 6.9: The on/off ratio's dependence on the input excitation intensity.

Unsurprisingly, continual operation of the PASS gate results in a decrease in the dynamic on/off ratio (Figure 6.10). This is likely due to a combination of photoinduced processes including, but not limited to, photobleaching, accumulation of dark input fluorophores throughout the evaluation, and dimerization of thiyl radicals depleting the concentration of the reducing species. Further experimentation is required to determine which of these factors (and what others) pose the greatest challenge to improving device performance.

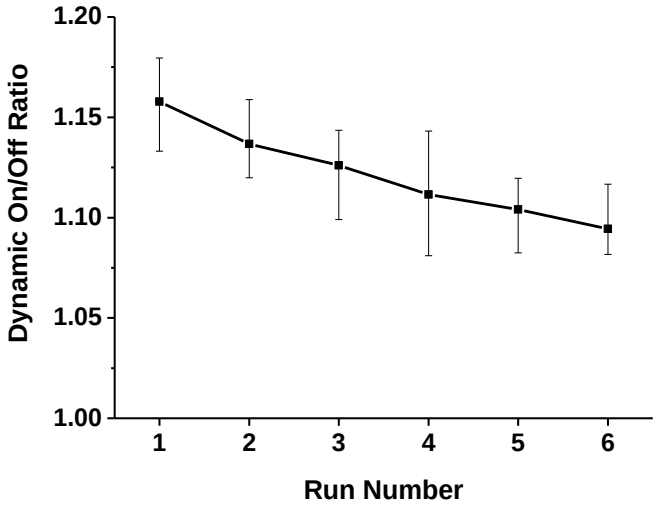

Figure 6.10: Decrease in the pass gate's dynamic on/off ratio after consecutive switching experiments. During each run, the pass gate is toggled on and off five times. The error bars represent the minimum and maximum on/off values for those five switching events.

In addition to characterizing the on/off ratio, we estimated the mean rise and fall times for the PASS gate. This was determined by finding the time at which the PASS gate's output fluorescence exceeds 90% or falls below 10% of the difference between the

average on and off state fluorescence values for each switching cycle. Since noise occasionally forces the signal to prematurely rise above or sink below these 10% and 90% values, we also calculated the rise and fall times for smoothed versions of the signal using a simple moving average and a second order Savitzky-Golay filter, each with a window length of 15 points. These signals are shown in Figure 6.11.

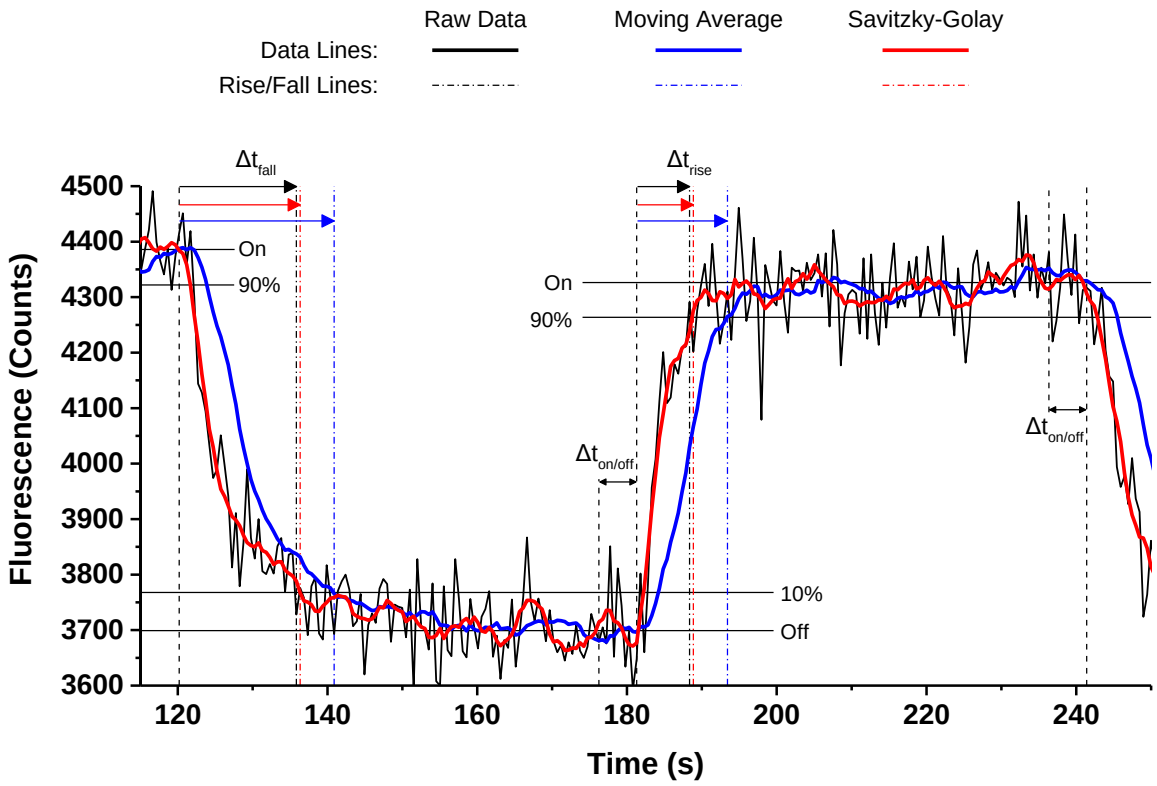

Figure 6.11: Depiction of the on/off ratio, rise time, and fall time analysis for a single switching event. The average on and off state fluorescence values, and their 10% and 90% values, are labeled with solid lines. Transitions times are illustrated with dotted lines, and the rise and fall times associated with each signal are denoted as Δt_{rise} and Δt_{fall} respectively (color coded according to their corresponding signal).

As expected, the moving average lags behind the original signal, leading to elongated transition times. The Savitzky-Golay signal, on the other hand, closely follows the raw data. The average rise and fall times are summarized in Table 6.1. It should be noted that the manual shuttering of the 670 nm beam can introduce up to a 1.5 second delay, leading to a general overestimation of the transition times, and thus, an overall conservative evaluation of our device.

Table 6.1: Mean rise and fall times extracted from the raw data, moving average, and Savitzky-Golay filtered PASS gate fluorescence signals.

	Raw Data	**Moving Average**	**Savitzky-Golay**
Rise Time	7.5 s	15.9 s	11.1 s
Fall Time	10.4 s	24.2 s	18.0 s

Based on these rise and fall times, we can make reasonable estimates regarding the time scale for PCL's two-phase operation. The pre-charge phase will be roughly equal to the rise time, i.e. ~12 seconds, in order to allow an ensemble of devices to reach their logical 1 value. In the future, this duration can be shortened. The rise time for PCL devices depends on the rate at which the input fluorophores transition into their dark state. Previous research suggests that this transition rate depends linearly on the input excitation intensity and can therefore be quadratically improved by simply focusing the

input beam, e.g. shrinking the focal point's radius by a factor of four will increase the intensity, and transition rate, by a factor of 16 [65].

As for the evaluation duration, this phase must be kept much shorter than the fall time (<<18 s). This ensures that the logical 1 output is captured before the output fluorescence decays below a 0-1 threshold. For example, based on Figure 6.11, this period should be restricted to the first few seconds directly following the pre-charge phase. This phase (and the associated fall time) can be shortened by irradiating the input fluorophores with UV light, which forces them back to ground at a rate that also depends linearly on the intensity. Alternatively, this phase can be lengthened by choosing fluorophores with longer dark state lifetimes or by lowering the oxygen content in the buffer. In buffers completely devoid of oxygen, certain dark fluorophore states can persist for hours [65].

It's also worth noting that even without any further improvement, the rise and fall times of this device are roughly an order of magnitude faster than other forms of molecular-scale computing used in similar, biologically relevant environments. For example, DNA-based logic gates, which perform Boolean operations based on the interactions of individual strands of DNA, often have transition times on the order of several minutes or longer [89].

6.4 Summary and Future Work

We have experimentally demonstrated a working PCL PASS gate that modulates the flow of excitons by exploiting the dark states of fluorescent molecules. Our particular implementation has an observable on/off ratio between 2.4 and 2.6 and a maximum on/off ratio of ~8.7. Given our current switching conditions, we find that the dynamic on/off ratio for this PASS gate is only ~1.16. A full exploration of the experimental switching conditions, however, may significantly improve the dynamic performance of this device, as well as future PCL devices. Such parameters include the reducing agent concentration, reducing agent species, pH, ratio of input to eval excitation intensity, fluorophore layout, and even the fluorophore choices. Given this vast design space, these investigations are left as future work.

PCL offers a route towards building complex, scalable RET systems. By experimentally demonstrating a working PASS gate, this chapter has provided substantial evidence that these logic gates can be realistically implemented. While there are many PCL gates that must still be demonstrated, all of these devices share the same underlying principles as the PASS gate, and thus, these too are likely to function as proposed.

7. Future Research Directions

In the previous chapters, we focused on outlining any remaining work regarding PCL. While it is imperative that those concepts be explored to further validate and expand upon PCL, there are a variety of other challenges regarding large-scale RET system design that have not been addressed by this dissertation (simply because they are outside the scope of this thesis). In this chapter, we briefly discuss a few of these areas in hopes of defining potential research directions for those interested in advancing the field of RET logic.

As discussed in Section 2.3.1, all RET systems require uniquely addressable inputs and outputs. This implies that distinct, non-overlapping regions of the visible spectrum must be reserved for exciting each input and for monitoring the emission from each output. Most fluorophores, however, have relatively broad excitation and emission spectra, often spanning 50–100 nm each. This leads to significant spectral overlap between fluorophores in real RET systems (as experimentally shown in Section 6.2 when performing a spectral decomposition on the PASS gate's on and off states), which places practical limits on the maximum number of inputs and outputs in order to avoid excitation or emission crosstalk. To expand the number of inputs and outputs, methods for synthesizing fluorophores with narrower excitation and emission spectra must be explored. Alternatively, it may be possible to spatially retain addressability by ensuring

that different excitation beams (or photodetectors for outputs) only illuminate (or monitor) subsections of a RET circuit rather than the entire system. Excitation spot sizes will, of course, always be diffraction limited, and thus, this solution only applies to very large RET systems in which any inputs with overlapping excitation spectra (or outputs with overlapping emission spectra) can be placed far apart.

In addition to these spectral challenges, after many excitation cycles, fluorophores typically undergo a destructive process known as photobleaching, which irreversibly eliminates the molecule's ability to fluoresce. The number of excitation cycles that a fluorophore can endure before photobleaching depends on the fluorophore itself, as well as its microenvironment, with certain molecules in the solvent, such as dissolved oxygen, playing a dominant role in the destructive process [90]. Due to photobleaching, RET systems can only survive a finite number of computational operations before ceasing to function properly. To address this, methods for increasing the longevity of fluorophores must be investigated. One such method is to protect the fluorophores from molecular oxygen and other reactive species by encapsulating them in certain materials, e.g. coating them with a silica shell. This additional layer of material provides a protective barrier between the molecule and the solvent, and has been shown to lower the rate of photobleaching [91, 92]. Applying this concept to RET circuits, one can imagine encapsulating an entire RET network, including both the fluorophores and

the DNA substrate. This encapsulation process and its effect on the resulting RET network must still be studied, e.g. structural deformations, changes in the fluorophores' properties, etc. The longevity of these circuits may also be improved by substituting the fluorophores with inorganic nanoparticles such as quantum dots since these nanoparticles can also participate in RET but are significantly more photostable than organic fluorophores [93].

Lastly, in order to design more complex RET systems, strategies for accurately predicting fluorophore positions and orientations on DNA nanostructures must be developed. While a variety of tools have been created to help design RET networks, these tools typically only capture the governing principles of RET and lack any predictive capabilities regarding the effects of the assembly process [94]. For instance, when designing a RET device we often assume that fluorophores are able to freely rotate in all directions, allowing us to use the rotational average of 2/3 as the orientation factor for each RET pair; however, once assembled, fluorophores may be rotationally hindered, taking on only a small range of orientations, which leads to a drastically different average value. The lack of a predictive simulator generally forces designers to troubleshoot RET devices post-assembly, by first characterizing the device to determine any unexpected issues and then fixing these problems in subsequent iterations of the device. Molecular dynamics (MD) simulations may be able to accurately predict certain

interactions for nanostructures and fluorophores with well-established molecular models; however, given the complexity and time required by these simulations, MD is unlikely to provide a realistic solution for designing large-scale RET systems. A more suitable method for addressing this issue may be to intentionally design the underlying DNA substrate such that we can reasonably predict its influence on the attached fluorophores. For example, when conjugated to the end of a DNA duplex, certain fluorophores prefer to stack on top of the helix, parallel to the bases of the duplex, rather than sit alongside the DNA duplex [95]. Exploiting this information, it may be possible to design a structure in which all of the fluorophore conjugation sites are placed at the ends of DNA helices, thereby allowing the circuit designer to reasonably predict the angle of each fluorophore relative to the substrate.

The challenges discussed in this chapter provide additional opportunities for improving both the size and complexity of RET systems. Although we have provided a few potential solutions, these examples are not meant to be exhaustive, but to instead provide readers with reasonable starting points and spur the development of alternative solutions. Improvements in any of these areas are likely to have significant impacts on both RET logic design, and more broadly, the study of fluorescence, RET, and DNA nanotechnology.

8. Dissertation Summary

Resonance energy transfer (RET) logic provides a method for building integrated molecular circuits that perform computation in domains incompatible with silicon-based systems. Using DNA self-assembly as a bottom-up fabrication strategy, networks of fluorescent molecules are arranged into spatial configurations that perform Boolean operations similar to conventional digital logic. Photons supplied as external inputs generate excitons that traverse these networks according to engineered RET pathways. Upon reaching designated output fluorophores, these excitons are fluoresced from the RET network, relaying the results of the computation back to the user.

Based on these principles, a variety of basic logic elements have been demonstrated; however, current methods for designing RET circuits suffer from two forms of signal loss that restrict both the size and topology of larger systems. These forms of signal degradation are exciton loss and energy loss. Exciton loss lowers the overall output fluorescence from RET circuits and increases exponentially with circuit length, placing practical limitations on the depth of a RET network. Energy loss forces the outputs of RET circuits to be lower in energy than the inputs, making it difficult to cascade devices or build systems with feedback. In this dissertation, we have explored methods for overcoming both of these limitations in an effort to build scalable RET circuits capable of performing more complex Boolean operations.

To address the energy loss in RET systems, we developed the RET relay, composed of near-infrared (NIR) and visibly excited fluorophores adsorbed to an upconverting nanoparticle (UCNP). The NIR fluorophore serves as the input to this device, donating low energy excitons to the UCNP when excited. After receiving many of these excitons, the UCNP reaches a highly excited state from which it transfers a single, high energy exciton to the visible fluorophore. Thus, when placed between RET networks, the relay can convert the low energy output from an upstream network into the high energy input required by a downstream network.

To demonstrate working operation of the relay, we characterized each half of the device, showing successful energy transfer both to and from the particle. We then provided evidence of the energy restoration performed by the full relay by exciting the NIR fluorophore and extracting output fluorescence from the visible fluorophore. Despite this success, the integration of this proof-of-concept device into RET circuitry remains a challenge. It is currently assembled in organic solvents that are unsuitable for the fabrication of RET circuits and methods for transferring it into an aqueous buffer compatible with DNA self-assembly have yet to be explored. More importantly, the relay suffers from substantial exciton loss, which may limit its applicability in large-scale systems.

Given these challenges, we developed an alternative form of RET logic design, called Pre-Charge Logic (PCL), which exploits the dark states of fluorescent molecules to dynamically modulate the flow of excitons. Leveraging this concept, we created a library of logic gates, which currently includes AND, OR, NAND, NOR, XOR, XNOR, PASS, and NPASS. These logic gates can be cascaded to perform more complex Boolean operations than previously achievable by any single RET system. Furthermore, by dividing PCL cascades into stages and evaluating these sequentially, we showed that this form of logic can theoretically decouple the length of a RET circuit from both its exciton loss and its energy loss, thereby providing a route towards building scalable RET systems.

To validate the design principles of PCL, we simulated each logic gate using continuous-time Markov chain models of the underlying fluorophore networks. These simulations show that every device performs the correct Boolean operation, and that the performance of these logic gates can be improved by making slight modifications to their original Exciton Flow Diagrams (EFDs) and by tuning certain transfer efficiencies within each network. We also modeled simple PCL cascades, showing that they function as expected and adhere to the same design principles that influence the performance of individual logic gates. Multi-Eval PCL (MEPCL) cascade simulations were left as future

work given their need for a more complex model capable of capturing the interactions of different logic gates.

In addition to simulating PCL, we experimentally demonstrated a working PASS gate. We translated the EFD of this device into a set of commercially available fluorophores. We then mapped the locations of these molecules to conjugation sites on a DNA nanostructure and assembled two different versions of the PASS gate, one with the input fluorophore present and one without. By taking steady-state and time-resolved fluorescence measurements of these two static networks, we confirmed that the individual states of the PASS gate function properly. We then validated the dynamic modulation of this logic gate by toggling the input fluorophore on and off and observing the change in output fluorescence. While there are still a variety of experimental parameters left to be optimized, this demonstration shows that PCL gates can be feasibly fabricated and operate as designed.

PCL presents a realistic path forward towards overcoming the limitations of signal loss in RET systems. The simulations provided by this dissertation corroborate the design principles of this technology, and the experimental evidence suggests that these devices are realistically achievable. As PCL continues to be explored both theoretically and experimentally, it may enable the construction of complex, scalable integrated molecular circuits.

Appendix A. Experimental Setup

A.1 Materials and Methods

The following section provides the experimental details regarding the RET relay and PASS gate experiments.

A.1.1 UCNP RET Relay

Relay Fabrication. UCNPs were purchased from Mesolight LLC at stock concentration of 10 mg mL^{-1} in chloroform. ATTO 488 and Cyto 840 were purchased from Sigma-Aldrich and Cyto Diagnostics, respectively, both with NHS ester modifications. Relays were fabricated by adding each dye (0.5 μL) suspended in DMSO to the UCNP stock (25 μL) in a 300 μL reduced surface activity (RSA) glass insert. The insert was then placed in an RSA glass autosampler vial, sealed with Parafilm, and vortexed for 10 s to ensure initial mixing. The sample was then sonicated for 2 hours at room temperature. Afterward, additional chloroform (125 μL) was added to the sample in order to raise the volume for measurement purposes. Lastly, the sample was sonicated for another 15 minutes to adequately mix in the new solvent and reach equilibrium. When synthesizing controls in which certain relay components were omitted, the omitted component was replaced with its respective solvent in order to keep the ratios of solvents consistent across all samples. For example, when testing each half of the relay, the other dye was replaced with pure DMSO (0.5 μL) and when testing

free dyes, the UCNPs were replaced with chloroform (25 μL). All measurements used the same batch of UCNPs from Mesolight.

Photoluminescence Measurements. Photoluminescence measurements were taken with the optical setup shown in Appendix A.3.1. When taking these measurements, 100 μL of sample was loaded into a Thorlabs fused quartz cuvette sealed with a PTFE stopper to prevent evaporation. Prior to use, cuvettes were cleaned with 10% acetic acid and rinsed thoroughly with ddH20. Samples were excited at 980 nm with an M9-980-0250 laser diode purchased from Thorlabs driven with 250 mA and kept at 25°C. Similarly, 810 nm excitation was achieved with an L808P1WJ laser diode purchased from Thorlabs and driven with 1900 mA at 25°C. These excitation sources were focused into the center of the cuvette with a 1 inch, f=25.4 mm lens also purchased from Thorlabs. Photoluminescence was collected at 90° through a 750 nm low pass filter by fiber optic cable and recorded with an Ocean Optics S200 Spectrometer. The integration times were 700 ms and 5s for 980 nm and 810 nm excitation respectively, except for the results in figures comparing spectra taken at 810 nm excitation. These measurements were integrated for 9s to optimize the SNR for visualization purposes.

Time-Resolved Measurements. Time domain measurements were taken with the custom TCSPC setup shown in Appendix A.3.2. Using an 80 MHz pulsed NKT supercontinuum laser as the excitation source, collimated white light was filtered with a

Crystal Technologies visible acousto-optical tunable filter (AOTF). The excitation was then focused into the center of the cuvettes mentioned above and fluorescence was collected at 90° through an emission monochromator. Once filtered, the emitted light was focused onto an ID100 single photon avalanche detector (SPAD) manufactured by ID Quantique. Single photon events from this detector were recorded by an SPC-130 synced to the clock of the NKT laser. When taking anisotropy measurements, wave plates and polarizers were placed in the excitation and emission paths respectively, allowing for all four polarization permutations to be collected for each sample.

TEM Measurements. TEM measurements were taken with an FEI Tecnai G2 Twin at 160 kV accelerating voltage. Grids were prepared by pipetting 1.5-2.0 μL of ~1 mg/mL relay or unmodified UCNPs onto formvar stabilized 200 mesh Cu carbon coated grids purchased from Fisher Scientific. The solvent was allowed to evaporate for ~2 minutes in the fume hood before storage. Measurements were performed the following day.

A.1.2 PASS Gate

DNA and Fluorophores. All DNA strands were purchased from Integrated DNA Technologies in lyophilized form. The standard, unmodified cross motif consists of the following DNA Sequences (from 5′ to 3′):

Arm 1.1: gttatcggcgtgtggttgcataatac

Arm 1.2: caatcacggatgagtagtgggctcagtcggacattc

Arm 1.3: cctcgtcggtagaacggtggaagcctccggtcgtgc

Arm 1.4: ttcaactgttcgtggcgctatattgt

Shell A1: atgcaacctgcctggcaagactccagaggactactcatccgt

Shell A2: tccgactgagccctgctaggatcgacttcactggaccgttctaccga

Shell A3: accggaggcttcctgtacggcagaactccgttggacgaacag

Shell A4: atagcgcctgatcgcaacgcctacgatggacacgccg

Core A: aggcaccatcgtaggttttcgttgcgatcaccaacggagttttttctgccgtacaccagtgaagt ttttcgatcctagcacctctggagtttttcttgcc

Amino-modified strands for assembling the PASS gate fluorophores are the following (where the /iUniAmM/ is IDT code for the internal Uni-LinkTM amino-modifier):

Arm 1.4 – Eval: ttcaactgttcg/iUniAmM/tggcgctatattgt

Shell A3 – Mediator: accggaggcttcctgtacggcagaact/iUniAmM/ccgttggacgaacag

Shell A1 – Output: atgcaacctgcct/iUniAmM/ggcaagactccagaggactactcatccgt

Shell A4 – Input: atagcgcctgatcgcaacgcct/iUniAmM/acgatggacacgccg

Standard tile strands were resuspended in 1X TAE and amino-modified strands were resuspended in 100 mM sodium tetraborate (buffer recipe in Appendix A.2.2) to avoid free amine groups during conjugation. TAE was purchased from Life Technologies at 50X and diluted accordingly. Cy2 was custom synthesized by Lumiprobe to have a single NHS ester group. NHS ester modified Cy3 and AT680 were purchased from Sigma Aldrich. NHS ester modified Texas Red-X was purchased from Life Technologies. All fluorophores were resuspended in DMSO and stored at -80°C prior to conjugation.

Conjugation and Purification. Fluorophores were conjugated to their respective strands by adding 20-60 fold excess dye and shaking for 18 hours at 1000 rpm (see Appendix A.2.3). Free dye was removed using Micro Bio-Spin P-6 Gel disposable chromatography columns purchased from Bio-Rad (see Appendix A.2.4). Labeled strands were then separated and extracted by an Agilent 1260 Infinity HPLC equipped with a 2.1 x 150 mm, 8 μm column (PL1912-3803) and an automated fraction collector (see Appendix A.2.5). Labeled fractions were desalted and buffer exchanged into 1X TAE by vacufuging the fraction, re-suspending the pellet in 1X TAE, and running the resuspension through another 1X TAE loaded P-6 disposable chromatography column.

DNA Nanostructure Assembly. DNA tiles were assembled in 1X TAE with 12.5 mM Mg^{++} (recipe in Appendix A.2.1). Tiles were annealed by raising the temperature to 96°C and cooling them to 4°C over the course of 5 hours. Tiles were then stored at 4°C overnight and measured the following day.

Absorbance and Fluorescence Measurements. Absorbance data was recorded with a NanoDrop 2000c spectrophotometer. Fluorescence measurements were taken using a FluoroMax-3 spectrofluorometer with the excitation and emission monochromators set to a 5 nm spectral bandwidth. Data was recorded in 1 nm increments with a 0.5 s integration time. The excitation wavelength was set to 450 nm, 500 nm, 540 nm, and 600 nm for Cy2, Cy3, TR, and AT680 fluorescence measurements respectively.

Time-Resolved measurements. Time-resolved fluorescence was recorded with the custom optical setup shown in Appendix A.3.2. The eval fluorophore was excited by an 80 MHz pulsed NKT supercontinuum laser filtered by a Crystal Technologies visible AOTF. The input fluorophore was excited by an SLD1332V 670 nm laser diode purchased from Thorlabs, driven with 800 mA (unless otherwise specified) and temperature controlled to 24 °C. Fluorescence was collected at 90° from a cuvette containing 60 μL of sample. This emission was filtered through a monochromator to select the observational wavelength. An additional 650 nm low pass filter was placed

between the cuvette holder and the monochromator to reduce 670 nm scatter. Fluorescence was focused onto an ID Quantique ID100 SPAD connected to either a Stanford Research Systems SR400 Photon Counter (controlled with the custom software in Appendix B.1) to collect time trace data (0.5 s bin widths) or an SPC-130 to collect TCSPC data (3.05 ps bin widths).

MEA Buffer Preparation. MEA was purchased from Sigma Aldrich. MEA buffer was prepared by first making a 650 mM MEA stock solution in 1X TAE with 12.5 mM Mg^{++} (recipe in Appendix A.2.1), adjusted to a pH of ~7.0 with acetic acid. To reach a final ~100 mM MEA concentration, 10 uL of pH adjusted MEA solution was added to 55 uL of PASS gate sample already suspended in 1X TAE, Mg^{++} buffer.

A.2 Buffer Recipes and Protocols

The following section provides the buffer recipes and general protocols used in the experimental sections of this dissertation.

A.2.1 10X TAE with Mg^{++}

Procedure for making 40 mL of 10X TAE with 125 mM Mg^{++}:

1. Weigh out 1.072 grams of magnesium acetate tetrahydrate into a 50 mL falcon tube. If the actual amount weighed differs from this target value, adjust the final total buffer volume accordingly (m_w = 214.45 g/mol). For instance, if 0.95 g is measured, the final volume will instead be:

$$\frac{0.95\ \text{g}}{1} \times \frac{\text{mol}}{214.45\ \text{g}} \times \frac{\text{L}}{125 \times 10^{-3}\ \text{mol}} = 35.439\ \text{mL}$$

2. Add 8 mL of 50X TAE and 22 mL of water to the magnesium acetate. Vortex until dissolved.
3. Add 500 uL of acetic acid to the TAE solution and vortex for 10 seconds.
4. Measure the pH. The target pH is 7.5. At this point, it should still be above 8.
5. Repeat step 3 and 4 until the pH reaches 7.5. Be sure to reduce the amount of acetic acid added as the pH begins to change.
6. Once the buffer has been pH balanced, add the remaining water to raise the volume to the adjusted final volume calculated in step 1.
7. To remove any aggregates, run the 10X TAE through a 0.2 μm membrane filter.

To make 40 mL of 1X TAE with 12.5 mM Mg^{++}, add 4 mL of this 10X solution to 36 mL of water.

A.2.2 100 mM NaTB

Procedure for making 40 mL of 100 mM NaTB buffer:

1. Weigh out 1.525 grams of sodium tetraborate decahydrate into a 50 mL falcon tube. If the actual amount weighed differs from this target value, adjust the final total buffer volume accordingly (m_w = 381.37 g/mol). For instance, if 1.355 g is measured, the final NaTB volume will instead be:

$$\frac{1.355\ \text{g}}{1} \times \frac{\text{mol}}{381.37\ \text{g}} \times \frac{\text{L}}{100 \times 10^{-3}\ \text{mol}} = 35.530\ \text{mL}$$

2. Weigh out 0.3997 grams of sodium hydroxide (NaOH) to make 10 mL of 1 M NaOH. Again, if the actual amount weighed differs from this target value, adjust the volume accordingly (m_w = 39.97 g/mol).
3. Add 10 mL (or adjusted volume) to the NaOH. Vortex until dissolved.
4. Add 25 mL of water to the NaTB. Vortex until mostly dissolved. Without adjusting the pH, it will be difficult to fully dissolve.
5. Add 1 mL of 1 M NaOH to the NaTB solution. Vortex for 10 seconds.
6. Check the pH of the NaTB solution. The target pH is 8.3. At this point it should still be below 7.
7. Repeat steps 5 and 6 until the pH reaches 8.3. Be sure to reduce the amount of NaOH added as the pH begins to change.
8. Once the buffer has been pH balanced, add the remaining water to raise the volume to the adjusted final volume calculated in step 1.
9. To remove any aggregates, run the NaTB buffer through a 0.2 μm membrane filter.

A.2.3 DNA-Fluorophore Conjugation (NHS Ester – Amine Reaction)

Procedure for conjugating an NHS ester modified fluorophore to amino-modified DNA strand:

1. Measure the concentrations of your dye and DNA samples using absorbance measurements of each and the Beer-Lambert law.
2. Make sure that your DNA sample is suspended in an amine free buffer, such as NaTB; otherwise, the buffer will outcompete the amino-modified DNA strands in the desired reaction.
3. Calculate the volume of dye to add to your DNA sample. To increase the conjugation yield, it is generally recommended that excess dye be added. Try starting with 5x-10x additional dye. For example, if the dye concentration is 3 mM and you would like to label a 50 uL sample of 25 uM DNA, a 5-fold excess would mean adding 2.1 uL of dye solution to the 50 uL of DNA solution:

$$\frac{5 \times 50\ \text{uL} \times 25\ \text{uM}}{3\ \text{mM}} \approx 2.1\ \text{uL}$$

   If you find that the conjugation yield is unacceptably low after the reaction, try increasing the amount of excess dye. Conversely, if the yield is suitable but it is difficult to remove all of the free dye post-conjugation, try lowering the amount of excess dye.
4. Add the dye volume calculated in the previous step to the DNA aliquot.
5. Cover the sample to avoid exposure to light.
6. Shake for 18 hours.
7. Filter the remaining free dye using the procedure in Appendix A.2.4.

A.2.4 Free Dye Filtration

Procedure for removing free dye after conjugation using Micro Bio-Spin P-6 chromatography columns (based on the manufacturer's protocol with slight modifications):

1. Remove a column from the fridge.
2. Flip the column upside down multiple times to ensure that the gel has not settled.
3. Break the cap off of the bottom of the column and allow excess buffer to drain for 2 minutes into a separate micotube. Keep this buffer as a baseline if you plan on measuring the absorbance of the final product without performing a buffer exchange.
4. Place the column in a fresh microtube and centrifuge the column at 1000g for 2 minutes.
5. Discard the collected buffer.
6. If performing a buffer exchange, do the following:
    a. Place the column in a new microtube.
    b. Add 500 uL of the desired buffer to the column.
    c. Centrifuge the column at 1000g for 1 minute.
    d. Discard the collected buffer.
    e. Repeat a-d four more times
    f. Place the column in a new microtube and centrifuge at 1000g for 1 additional minute to ensure that the extra buffer has been removed.
7. Place the column in a new microtube, labeled appropriately based on the final sample
8. Add 20-75 μL of the sample directly to the top of the column.
9. Centrifuge the column at 1000g for 4 minutes.
10. The purified sample is at the bottom of the microtube. Keep this sample and discard the column.

A.2.5 Separation of Labeled and Unlabeled DNA By HPLC

Buffers and settings used when separating labeled DNA from unlabeled DNA with an Agilent 1260 Infinity HPLC (adapted from a previous procedure developed by members of the Duke Self-Assembled Systems Group):

Buffer Solutions:

Column:	PL1912-3803: 2.1 x 150 mm, 8 μm
Mobile Phase A:	0.1 M TEAA
Mobile Phase B:	0.1 M TEAA in 50% Acetonitrile (ACN), 50% Water
Mobile Phase C:	7:1 ACN:Water

General Procedure:

1. Turn on all components of the 1260 Infinity.
2. Ensure that each of these components are set accordingly:
   i. **Sampler:** Set up an injection with a volume dictated by your sample (maximum of 100 μL). Use a needle wash. By default, the needle wash location is set to Vial 1. This vial should contain 500 μl of 0.1 M TEAA.
   ii. **Quaternary Pump:** Set the flow rate to 0.200 mL/minute. Set the maximum pressure to 100 bar. Start the pump with 100% C to initially flush the column.
   iii. **Column:** Set the temperature of the left side of the column to 60°C.
   iv. **DAD:** Set the observation wavelengths for DNA to 260 nm and 280 nm. Add signals for each fluorophore, aiming for their absorption wavelengths while avoiding their emission regions. Set the reference wavelengths to values outside of the absorption and emission bands of each fluorophore.
   v. **Fraction Collector:** Set the peak threshold to 100 and the type of fraction collection to peak-based.
3. Allow 100% C to flush the column for 15 minutes.
4. While flushing the column, set up the sample method using the timetable below.
5. Allow 90% A, 10% B to flush the column for 15 minutes.
6. Fill the first three columns of the fraction collector's sample tray with empty autosampler vials.

7. Load your sample into a low volume autosampler vial. Note that the maximum volume is 100 μL. Place this vial in the Infinity 1260's sampler at the location specified when setting up the injection in step 2.
8. Run the sample using the method established in step 4.
9. After the run has finished, remove and label each of the collected fractions.
10. Repeat steps 6-9 for all samples of interest.
11. Shut down each component of the instrument. If the column will not be used for an extended period of time, store the column according to the manufacturer's protocol.

Timetable:

Time (Minutes)	Mobile Phase A (%)	Mobile Phase B (%)	Mobile Phase C (%)
0.00	90.0	10.0	0.0
70.00	40.0	60.0	0.0
70.01	90.0	10.0	0.0
75.00	90.0	10.0	0.0
75.01	0.0	0.0	100.0
90.00	0.0	0.0	100.0
90.01	90.0	10.0	0.0
105.0	90.0	10.0	0.0

A.3 Custom Instrumentation

The following diagrams provide an overview of the custom optical setups used in the experimental sections of this dissertation.

A.3.1 Photoluminescence Setup

Diagram of the optical setup designed for measuring the UCNP RET relay:

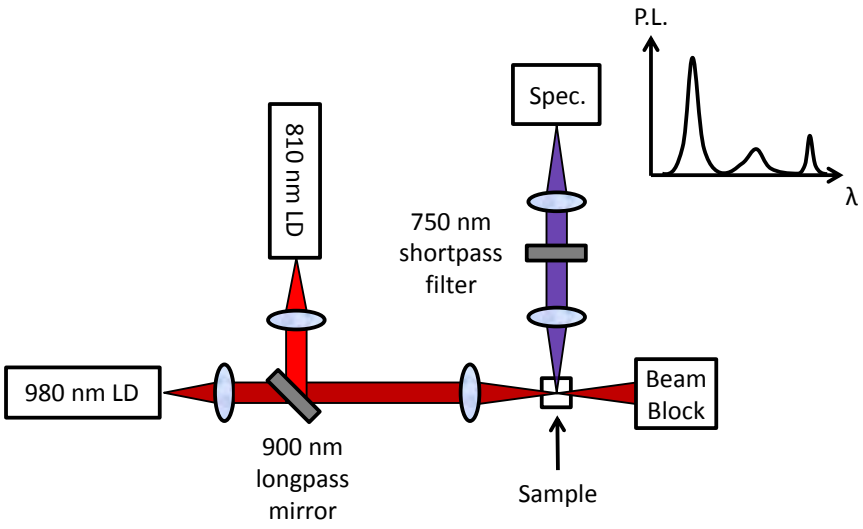

A.3.2 Time-Resolved Fluorescence Setup

Diagram of the optical setup designed for taking time-resolved fluorescence measurements of both the UNCP RET relay and the PASS gate.

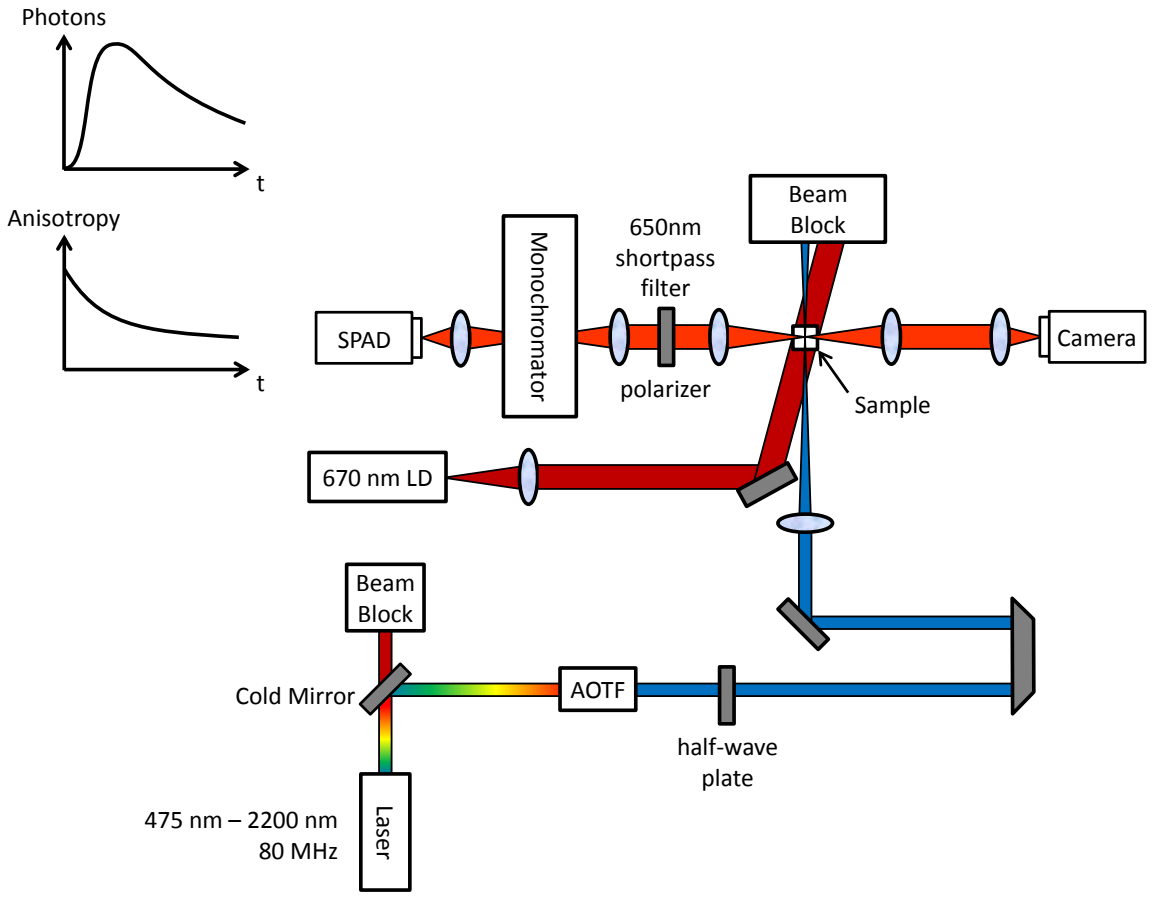

Appendix B. Custom Software

The following section describes custom software developed during this research.

B.1 SR400 Photon Counter

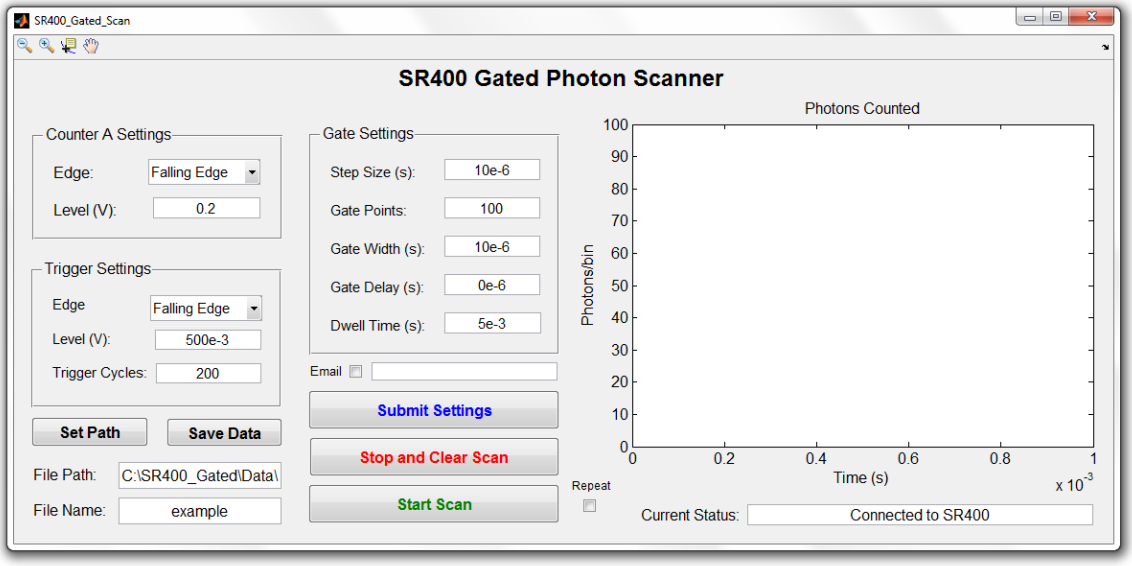

To operate the Stanford Research Systems SR400 Photon Counter, we developed a custom MATLAB tool to communicate with the instrument via RS-232. This software allows the user to remotely set the counter edge, counter level, trigger edge, trigger level, gate step size, gate width, and gate delay. Completed scans are plotted in the figure window on the right side of the GUI. Data can be saved to a .txt containing the scan settings followed by a list of time bins and their corresponding photon counts.

This software can be found at http://www.craiglaboda.com/software.

B.2 RET Logic Layout Tool

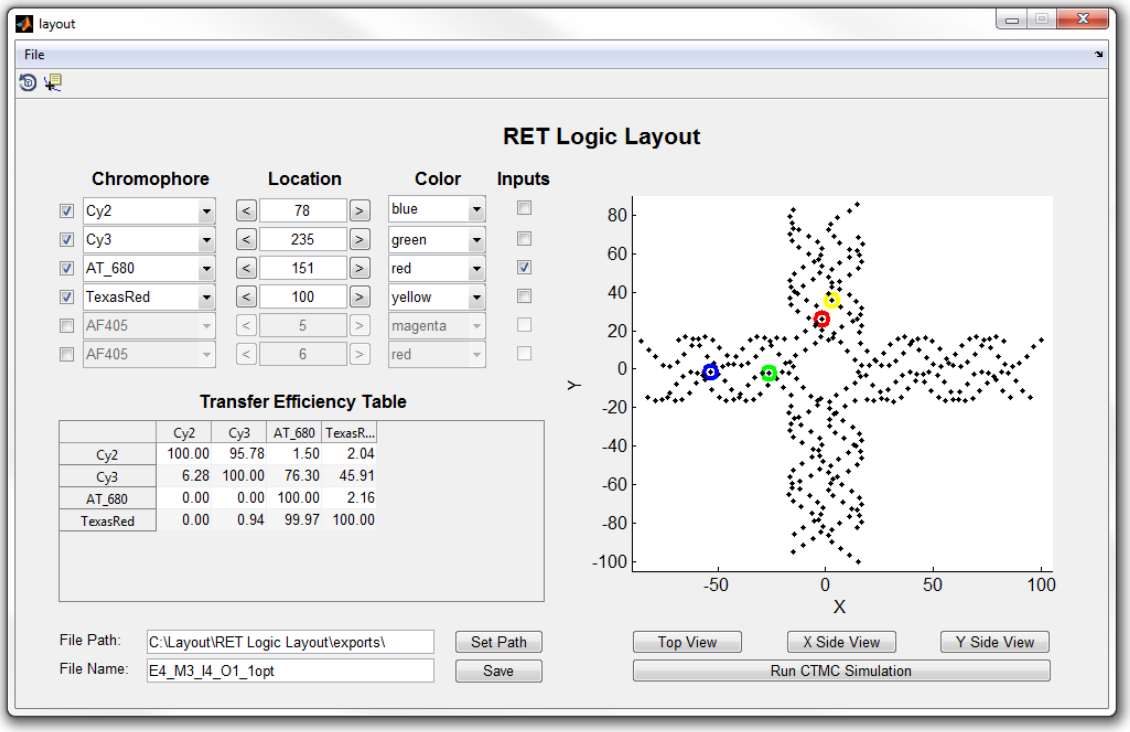

The RET Logic Layout Tool was developed to help with the design and layout of PCL gates on the DNA cross motif. Fluorophores are selected from drop-down menus on the left side of the GUI, which are populated by a local database. The user then positions these fluorophores based on available conjugation sites that were extracted from a PDB model of the DNA tile by incrementing or decrementing their location numbers. Based on the three-dimensional coordinates of these locations and the characterization of each fluorophore provided by the database, the transfer efficiency

table in the bottom left corner of the GUI is updated in real time, allowing the user to gain intuition regarding the design space.

The RET Logic Layout Tool also allows the user to run a CTMC simulation of the design. Fluorophores that will be toggled between their dark and fluorescent states are considered "Inputs" and are marked accordingly using the box directly to the right of their designated color. To run the corresponding CTMC simulations, the user clicks the button on the bottom right hand side of the GUI. This runs two CTMC simulations: one in which all fluorophores are present (off state) and one in which the input fluorophores are removed (on state). The tool then provides the CTMC solution to the user along with on/off ratio for the device.

This software can be found at http://www.craiglaboda.com/software.

Appendix C. Langmuir Adsorption

The Langmuir adsorption model is a first principle, rate equation based adsorption model developed by Irving Langmuir in the early 1900s. By assuming that the adsorption is a reversible process, the Langmuir model relates the equilibrium constant of adsorption to the fractional amount of adsorbate on a surface. Although originally developed to describe how an ideal gas adsorbs to a surface, this model has also been shown to capture the adsorption process of fluorescent molecules to nanoparticles [96].

The following derivation of the Langmuir adsorption model can be found in reference [97]. This derivation first assumes that the adsorption reaction occurs between an adsorbate and set of identical adsorption sites distributed across a surface. This reaction is captured by the reversible chemical equation below, where D represents the dye molecules (adsorbate), S represents the available binding sites, and D_{ad} represents the adsorbed dye:

$$D + S \rightleftarrows D_{ad}$$

The equilibrium constant for this reaction can be written as follows, where brackets around a species denote the concentration of that species:

$$K_{eq} = \frac{[D_{ad}]}{[D][S]}$$

The total concentration of adsorption sites, $[S_0]$, can be defined as the sum of the remaining available sites (S) and adsorbed dye molecules (D_{ad}):

$$[S_0] = [S] + [D_{ad}]$$

Rearranging the adsorption equilibrium constant and plugging this into the total site equation results in the following relationship:

$$[S_0] = \frac{[D_{ad}]\left(1 + K_{eq}[D]\right)}{K_{eq}[D]}$$

Lastly, the fractional occupancy of the adsorbed dye, θ, is considered to be the concentration of adsorbed dye divided by the total concentration of adsorption sites:

$$\theta = \frac{[D_{ad}]}{[S_0]}$$

Plugging the expression for θ back into the total site equation reveals the following relationship:

$$\theta = \frac{K_{eq}[D]}{1 + K_{eq}[D]}$$

This result shows that the fractional occupancy of an adsorbate, θ, is related to the equilibrium constant of the adsorption reaction and the equilibrium concentration of the adsorbate.

This derivation makes a few important assumptions. As mentioned earlier, every adsorption site is considered to be identical. It also assumes that there is only a single uniform layer of these adsorption sites available on the surface, as the equations above

cannot accurately capture the stacking of adsorbates. Lastly, it is assumed that neighboring adsorbed molecules do not interact with one another, i.e. they can be considered independent.

References

[1] C. Pistol, C. Dwyer, and A. R. Lebeck, "Nanoscale Optical Computing Using Resonance Energy Transfer Logic," *IEEE Micro,* vol. 28, no. 6, 2008, pp. 7-18.

[2] C. Dwyer, A. Rallapalli, M. Mottaghi, and S. Wang, "DNA Self-Assembled Nanostructures for Resonance Energy Transfer Circuits," in *Nanophotonic Information Physics*, Nano-Optics and Nanophotonics, Springer Berlin Heidelberg, 2014, pp. 41-65.

[3] C. LaBoda, H. Duschl, and C. L. Dwyer, "DNA-Enabled Integrated Molecular Systems for Computation and Sensing," *Accounts of Chemical Research,* vol. 47, no. 6, 2014, pp. 1816-1824.

[4] C. Pistol, V. Mao, V. Thusu, A. R. Lebeck, and C. Dwyer, "Encoded Multichromophore Response for Simultaneous Label-Free Detection," *Small,* vol. 6, no. 7, 2010, pp. 843-850.

[5] C. Pistol, W. Chongchitmate, C. Dwyer, and A. R. Lebeck, "Architectural Implications of Nanoscale Integrated Sensing and Computing," *Proceedings of the 14th International Conference on Architectural Support for Programming Languages and Operating Systems (ASPLOS 09)*, 2009, pp. 13-24.

[6] J. Elbaz, P. Yin, and C. A. Voigt, "Genetic encoding of DNA nanostructures and their self-assembly in living bacteria," *Nature Communications,* vol. 7, 2016, pp. 1-11.

[7] B. Valeur, *Molecular Fluorescence: Principles and Applications*, Wiley-VCH, 2002.

[8] C. D. LaBoda, and C. L. Dwyer, "Upconverting Nanoparticle Relays for Resonance Energy Transfer Networks," *Advanced Functional Materials,* vol. 26, no. 17, 2016, pp. 2866-2874.

[9] F. Wang, and X. G. Liu, "Recent advances in the chemistry of lanthanide-doped upconversion nanocrystals," *Chemical Society Reviews,* vol. 38, no. 4, 2009, pp. 976-989.

[10] S. Wang, A. R. Lebeck, and C. Dwyer, "Nanoscale Resonance Energy Transfer-Based Devices for Probabilistic Computing," *IEEE Micro,* vol. 35, no. 5, 2015, pp. 72-84.

[11] R. L. Liboff, "Chapter 12.2 One-Electron Atoms," in *Introductory Quantum Mechanics*, Addison-Wesley, 2003.

[12] T. Förster, "Energy migration and fluorescence," *Journal of Biomedical Optics,* vol. 17, no. 1, 2012, pp. 1-10.

[13] T. Förster, "Intermolecular energy migration and fluorescence," in *Biological Physics*, American Institute of Physics, 1993, pp. 148-160.

[14] "ATTO-TEC Fluorescent Labels and Dyes Catalogue," Available: https://www.atto-tec.com.

[15] I. Medintz, and N. Hildebrandt, *FRET-Förster Resonance Energy Transfer: From Theory to Applications*, Wiley-VCH, 2013.

[16] S. Sindbert, S. Kalinin, N. Hien, A. Kienzler, L. Clima, W. Bannwarth, B. Appel, S. Muller, and C. A. M. Seidel, "Accurate Distance Determination of Nucleic Acids via Forster Resonance Energy Transfer: Implications of Dye Linker Length and Rigidity," *Journal of the American Chemical Society,* vol. 133, no. 8, 2011, pp. 2463-2480.

[17] M. Heilemann, P. Tinnefeld, G. S. Mosteiro, M. Garcia-Parajo, N. F. Van Hulst, and M. Sauer, "Multistep energy transfer in single molecular photonic wires," *Journal of the American Chemical Society,* vol. 126, no. 21, 2004, pp. 6514-6515.

[18] K. Boeneman, D. E. Prasuhn, J. B. Blanco-Canosa, P. E. Dawson, J. S. Melinger, M. Ancona, M. H. Stewart, K. Susumu, A. Huston, and I. L. Medintz, "Self-Assembled Quantum Dot-Sensitized Multivalent DNA Photonic Wires," *Journal of the American Chemical Society,* vol. 132, no. 51, 2010, pp. 18177-18190.

[19] C. M. Spillmann, S. Buckhout-White, E. Oh, E. R. Goldman, M. G. Ancona, and I. L. Medintz, "Extending FRET cascades on linear DNA photonic wires," *Chemical Communications,* vol. 50, no. 55, 2014, pp. 7246-7249.

[20] S. Vyawahare, S. Eyal, K. D. Mathews, and S. R. Quake, "Nanometer-scale Fluorescence Resonance Optical Waveguides," *Nano Letters,* vol. 4, no. 6, 2004, pp. 1035-1039.

[21] J. K. Hannestad, P. Sandin, and B. Albinsson, "Self-Assembled DNA Photonic Wire for Long-Range Energy Transfer," *Journal of the American Chemical Society,* vol. 130, no. 47, 2008, pp. 15889-15895.

[22] J. K. Hannestad, S. R. Gerrard, T. Brown, and B. Albinsson, "Self-Assembled DNA-Based Fluorescence Waveguide with Selectable Output," *Small,* vol. 7, no. 22, 2011, pp. 3178-3185.

[23] W. Su, M. Schuster, C. R. Bagshaw, U. Rant, and G. A. Burley, "Site-Specific Assembly of DNA-Based Photonic Wires by Using Programmable Polyamides," *Angewandte Chemie-International Edition,* vol. 50, no. 12, 2011, pp. 2712-2715.

[24] S. A. Díaz, S. Buckhout-White, M. G. Ancona, C. M. Spillmann, E. R. Goldman, J. S. Melinger, and I. L. Medintz, "Extending DNA-Based Molecular Photonic Wires with Homogeneous Förster Resonance Energy Transfer," *Advanced Optical Materials,* vol. 4, no. 3, 2016, pp. 399-412.

[25] C. Dwyer, A. R. Lebeck, and C. Pistol, "Energy Transfer Logic on DNA Nanostructures: Enabling Molecular-Scale Amorphous Computing," *Proceedings of the 4th Workshop on Non-Silicon Computing (NSC4)*, 2007, pp. 33-40.

[26] J. Pang, A. R. Lebeck, and C. Dwyer, "Modeling and simulation of a nanoscale optical computing system," *Journal of Parallel and Distributed Computing,* vol. 74, no. 6, 2014, pp. 2470-2483.

[27] M. Beutler, K. Makrogianneli, R. J. Vermeij, M. Keppler, T. Ng, T. M. Jovin, and R. Heintzmann, "satFRET: estimation of Forster resonance energy transfer by acceptor saturation," *European Biophysics Journal with Biophysics Letters,* vol. 38, no. 1, 2008, pp. 69-82.

[28] V. Thusu, "Self-Assembled Resonance Energy Transfer Devices," Ph.D. Thesis, Electrical and Computer Engineering, Duke University, 2013.

[29] A. Rallapalli, "Resonance Energy Transfer-Based Molecular Switch Designed Using a Systematic Design Process Based on Monte Carlo Methods and Markov Chains," Ph.D. Thesis, Electrical and Computer Engineering, Duke University, 2016.

[30] C. Dwyer, and A. Lebeck, *Introduction to DNA Self-Assembled Computer Design*, Artech House, Inc., 2007.

[31] P. W. K. Rothemund, "Folding DNA to create nanoscale shapes and patterns," *Nature,* vol. 440, no. 7082, 2006, pp. 297-302.

[32] S. M. Douglas, H. Dietz, T. Liedl, B. Hogberg, F. Graf, and W. M. Shih, "Self-assembly of DNA into nanoscale three-dimensional shapes," *Nature,* vol. 459, no. 7245, 2009, pp. 414-418.

[33] H. Dietz, S. M. Douglas, and W. M. Shih, "Folding DNA into Twisted and Curved Nanoscale Shapes," *Science,* vol. 325, no. 5941, 2009, pp. 725-730.

[34] B. Wei, M. J. Dai, and P. Yin, "Complex shapes self-assembled from single-stranded DNA tiles," *Nature,* vol. 485, no. 7400, 2012, pp. 623-627.

[35] V. Linko, and H. Dietz, "The enabled state of DNA nanotechnology," *Current Opinion in Biotechnology,* vol. 24, no. 4, 2013, pp. 555-561.

[36] R. Carlson, "The changing economics of DNA synthesis," *Nature Biotechnology,* vol. 27, no. 12, 2009, pp. 1091-1094.

[37] A. D. Bates, and A. Maxwell, *DNA Topology*, IRL Press at Oxford University Press, 1993.

[38] M. van Dijk, and A. Bonvin, "3D-DART: a DNA structure modelling server," *Nucleic Acids Research,* vol. 37, no. suppl_2, 2009, pp. W235-W239.

[39] H. Yan, S. H. Park, G. Finkelstein, J. H. Reif, and T. H. LaBean, "DNA-Templated Self-Assembly of Protein Arrays and Highly Conductive Nanowires," *Science,* vol. 301, no. 5641, 2003, pp. 1882-1884.

[40] C. Pistol, and C. Dwyer, "Scalable, low-cost, hierarchical assembly of programmable DNA nanostructures," *Nanotechnology,* vol. 18, no. 12, 2007, pp. 125305-125309.

[41] S. H. Park, C. Pistol, S. J. Ahn, J. H. Reif, A. R. Lebeck, C. Dwyer, and T. H. LaBean, "Finite-Size, Fully Addressable DNA Tile Lattices Formed by Hierarchical Assembly Procedures," *Angewandte Chemie-International Edition,* vol. 45, no. 5, 2006, pp. 735-739.

[42] V. Mao, C. Dwyer, and K. Chakrabarty, "Fabrication Defects and Fault Models for DNA Self-Assembled Nanoelectronics," *International Test Conference (ITC 2008)*, 2008, pp. 1-10.

[43] V. Mao, V. Thusu, C. Dwyer, and K. Chakrabarty, "Connecting fabrication defects to fault models and SPICE simulations for DNA self-assembled nanoelectronics," *IET Computers and Digital Techniques,* vol. 3, no. 6, 2009, pp. 553-569.

[44] P. T. C. So, C. Y. Dong, B. R. Masters, and K. M. Berland, "Two-Photon Excitation Fluorescence Microscopy," *Annual Review of Biomedical Engineering,* vol. 2, no. 1, 2000, pp. 399-429.

[45] D. S. Bradshaw, and D. L. Andrews, "Competing mechanisms for energy transfer in two-photon absorbing systems," *Chemical Physics Letters,* vol. 430, no. 1-3, 2006, pp. 191-194.

[46] S. Heer, K. Kompe, H. U. Gudel, and M. Haase, "Highly Efficient Multicolour Upconversion Emission in Transparent Colloids of Lanthanide-Doped $NaYF_4$ Nanocrystals," *Advanced Materials,* vol. 16, no. 23-24, 2004, pp. 2102-2105.

[47] J. C. Boyer, and F. van Veggel, "Absolute quantum yield measurements of colloidal $NaYF_4$: Er^{3+}, Yb^{3+} upconverting nanoparticles," *Nanoscale,* vol. 2, no. 8, 2010, pp. 1417-1419.

[48] Z. Q. Li, Y. Zhang, and S. Jiang, "Multicolor Core/Shell-Structured Upconversion Fluorescent Nanoparticles," *Advanced Materials,* vol. 20, no. 24, 2008, pp. 4765–4769.

[49] T. Riuttamaki, I. Hyppanen, J. Kankare, and T. Soukka, "Decrease in Luminescence Lifetime Indicating Nonradiative Energy Transfer from Upconverting Phosphors to Fluorescent Acceptors in Aqueous Suspensions," *Journal of Physical Chemistry C,* vol. 115, no. 36, 2011, pp. 17736-17742.

[50] L. A. Cheng, K. Yang, M. W. Shao, S. T. Lee, and Z. A. Liu, "Multicolor In Vivo Imaging of Upconversion Nanopaticles with Emissions Tuned by Luminescence Resonance Energy Transfer," *Journal of Physical Chemistry C,* vol. 115, no. 6, 2011, pp. 2686-2692.

[51] D. T. Tu, L. Q. Liu, Q. Ju, Y. S. Liu, H. M. Zhu, R. F. Li, and X. Y. Chen, "Time-Resolved FRET Biosensor Based on Amine-Functionalized Lanthanide-Doped $NaYF_4$ Nanocrystals," *Angewandte Chemie-International Edition,* vol. 50, no. 28, 2011, pp. 6306-6310.

[52] A. Bednarkiewicz, M. Nyk, M. Samoc, and W. Strek, "Up-conversion FRET from Er^{3+}/Yb^{3+}:$NaYF_4$ Nanophosphor to CdSe Quantum Dots," *Journal of Physical Chemistry C,* vol. 114, no. 41, 2010, pp. 17535-17541.

[53] W. Q. Zou, C. Visser, J. A. Maduro, M. S. Pshenichnikov, and J. C. Hummelen, "Broadband dye-sensitized upconversion of near-infrared light," *Nature Photonics,* vol. 6, no. 8, 2012, pp. 560-564.

[54] G. Y. Chen, J. Damasco, H. L. Qiu, W. Shao, T. Y. Ohulchanskyy, R. R. Valiev, X. Wu, G. Han, Y. Wang, C. H. Yang, H. Agren, and P. N. Prasad, "Energy-Cascaded Upconversion in an Organic Dye-Sensitized Core/Shell Fluoride Nanocrystal," *Nano Letters,* vol. 15, no. 11, 2015, pp. 7400-7407.

[55] Z. G. Chen, H. L. Chen, H. Hu, M. X. Yu, F. Y. Li, Q. Zhang, Z. G. Zhou, T. Yi, and C. H. Huang, "Versatile Synthesis Strategy for Carboxylic Acid-Functionalized Upconverting Nanophosphors as Biological Labels," *Journal of the American Chemical Society,* vol. 130, no. 10, 2008, pp. 3023-3029.

[56] M. Wang, C. C. Mi, W. X. Wang, C. H. Liu, Y. F. Wu, Z. R. Xu, C. B. Mao, and S. K. Xu, "Immunolabeling and NIR-Excited Fluorescent Imaging of HeLa Cells by Using $NaYF_4$:Yb,Er Upconversion Nanoparticles," *ACS Nano,* vol. 3, no. 6, 2009, pp. 1580-1586.

[57] J. F. Suyver, A. Aebischer, D. Biner, P. Gerner, J. Grimm, S. Heer, K. W. Kramer, C. Reinhard, and H. U. Gudel, "Novel materials doped with trivalent lanthanides and transition metal ions showing near-infrared to visible photon upconversion," *Optical Materials,* vol. 27, no. 6, 2005, pp. 1111-1130.

[58] Y. Wang, L. P. Tu, J. W. Zhao, Y. J. Sun, X. G. Kong, and H. Zhang, "Upconversion Luminescence of ß-$NaYF_4$: Yb^{3+}, Er^{3+}@ß-$NaYF_4$ Core/Shell Nanoparticles: Excitation Power, Density and Surface Dependence," *Journal of Physical Chemistry C,* vol. 113, no. 17, 2009, pp. 7164-7169.

[59] C. F. Gainer, G. S. Joshua, C. R. De Silva, and M. Romanowski, "Control of green and red upconversion in $NaYF_4:Yb^{3+},Er^{3+}$ nanoparticles by excitation modulation," *Journal of Materials Chemistry,* vol. 21, no. 46, 2011, pp. 18530-18533.

[60] J. Hwang, J. Kang, S. K. Kim, and Y. Kim, "A convenient and efficient purification method for chemically labeled oligonucleotides," *Biotechniques,* vol. 54, no. 5, 2013, pp. 280-282.

[61] Y. A. Pyatenko, and A. A. Voronkov, "The Formula of Gagarinite," *Journal of Structural Chemistry,* vol. 3, no. 6, 1962, pp. 696-697.

[62] G. S. Yi, and G. M. Chow, "Water-Soluble $NaYF_4$: Yb,Er(Tm)/$NaYF_4$/Polymer Core/Shell/Shell Nanoparticles with Significant Enhancement of Upconversion Fluorescence," *Chemistry of Materials,* vol. 19, no. 3, 2007, pp. 341-343.

[63] F. Y. Liu, Q. Zhao, H. P. You, and Z. X. Wang, "Synthesis of stable carboxy-terminated $NaYF_4:Yb^{3+}$, Er^{3+}@SiO2 nanoparticles with ultrathin shell for biolabeling applications," *Nanoscale,* vol. 5, no. 3, 2013, pp. 1047-1053.

[64] L. L. Li, R. B. Zhang, L. L. Yin, K. Z. Zheng, W. P. Qin, P. R. Selvin, and Y. Lu, "Biomimetic Surface Engineering of Lanthanide-Doped Upconversion Nanoparticles as Versatile Bioprobes," *Angewandte Chemie-International Edition,* vol. 51, no. 25, 2012, pp. 6121-6125.

[65] S. van de Linde, I. Krstic, T. Prisner, S. Doose, M. Heilemann, and M. Sauer, "Photoinduced formation of reversible dye radicals and their impact on super-resolution imaging," *Photochemical & Photobiological Sciences,* vol. 10, no. 4, 2011, pp. 499-506.

[66] R. Fujii, T. Nishimura, Y. Ogura, and J. Tanida, "Nanoscale energy-route selector consisting of multiple photo-switchable fluorescence-resonance-energy-transfer structures on DNA," *Optical Review,* vol. 22, no. 2, 2015, pp. 316-321.

[67] T. Nishimura, Y. Ogura, and J. Tanida, "A Nanoscale Set-Reset Flip-Flop in Fluorescence Resonance Energy Transfer-Based Circuits," *Applied Physics Express,* vol. 6, no. 1, 2013, pp. 1-3.

[68] G. T. Dempsey, J. C. Vaughan, K. H. Chen, M. Bates, and X. W. Zhuang, "Evaluation of fluorophores for optimal performance in localization-based super-resolution imaging," *Nature Methods,* vol. 8, no. 12, 2011, pp. 1027-1036.

[69] M. Bates, T. R. Blosser, and X. W. Zhuang, "Short-Range Spectroscopic Ruler Based on a Single-Molecule Optical Switch," *Physical Review Letters,* vol. 94, no. 10, 2005, pp. 1-4.

[70] M. Bates, B. Huang, G. T. Dempsey, and X. W. Zhuang, "Multicolor Super-Resolution Imaging with Photo-Switchable Fluorescent Probes," *Science,* vol. 317, no. 5845, 2007, pp. 1749-1753.

[71] B. Huang, W. Q. Wang, M. Bates, and X. W. Zhuang, "Three-Dimensional Super-Resolution Imaging by Stochastic Optical Reconstruction Microscopy," *Science,* vol. 319, no. 5864, 2008, pp. 810-813.

[72] M. Heilemann, S. van de Linde, A. Mukherjee, and M. Sauer, "Super-Resolution Imaging with Small Organic Fluorophores," *Angewandte Chemie-International Edition,* vol. 48, no. 37, 2009, pp. 6903-6908.

[73] T. Kottke, S. van de Linde, M. Sauer, S. Kakorin, and M. Heilemann, "Identification of the Product of Photoswitching of an Oxazine Fluorophore Using Fourier Transform Infrared Difference Spectroscopy," *Journal of Physical Chemistry Letters,* vol. 1, no. 21, 2010, pp. 3156-3159.

[74] G. T. Dempsey, M. Bates, W. E. Kowtoniuk, D. R. Liu, R. Y. Tsien, and X. W. Zhuang, "Photoswitching Mechanism of Cyanine Dyes," *Journal of the American Chemical Society,* vol. 131, no. 51, 2009, pp. 18192–18193.

[75] M. Torimura, S. Kurata, K. Yamada, T. Yokomaku, Y. Kamagata, T. Kanagawa, and R. Kurane, "Fluorescence-Quenching Phenomenon by Photoinduced Electron Transfer Between a Fluorescent Dye and a Nucleotide Base," *Analytical Sciences,* vol. 17, no. 1, 2001, pp. 155-160.

[76] X. Y. Li, and D. R. Liu, "DNA-Templated Organic Synthesis: Nature's Strategy for Controlling Chemical Reactivity Applied to Synthetic Molecules," *Angewandte Chemie-International Edition,* vol. 43, no. 37, 2004, pp. 4848-4870.

[77] E. M. Conwell, and D. M. Basko, "Hole Traps in DNA," *Journal of the American Chemical Society,* vol. 123, no. 46, 2001, pp. 11441-11445.

[78] B. Giese, "Long Distance Charge Transport in DNA: The Hopping Mechanism," *Accounts of Chemical Research,* vol. 33, no. 9, 2000, pp. 631-636.

[79] F. D. Lewis, X. Liu, J. Liu, R. T. Hayes, and M. R. Wasielewski, "Dynamics and Equilibria for Oxidation of G, GG, and GGG Sequences in DNA Hairpins," *Journal of the American Chemical Society*, vol. 122, no. 48, 2000, pp. 12037-12038.

[80] G. J. Kavarnos, *Fundamentals of Photoinduced Electron Transfer*, Wiley-VCH, 1993.

[81] K. Kawai, E. Matsutani, A. Maruyama, and T. Majima, "Probing the Charge-Transfer Dynamics in DNA at the Single-Molecule Level," *Journal of the American Chemical Society*, vol. 133, no. 39, 2011, pp. 15568-15577.

[82] K. Kawai, Y. Osakada, M. Fujitsuka, and T. Majima, "Charge Separation in Acridine- and Phenothiazine-Modified DNA," *Journal of Physical Chemistry B*, vol. 112, no. 7, 2008, pp. 2144-2149.

[83] K. Kawai, Y. Osakada, T. Takada, M. Fujitsuka, and T. Majima, "Lifetime Regulation of the Charge-Separated State in DNA by Modulating the Oxidation Potential of Guanine in DNA Through Hydrogen Bonding," *Journal of the American Chemical Society*, vol. 126, no. 40, 2004, pp. 12843-12846.

[84] M. J. Rust, M. Bates, and X. W. Zhuang, "Sub-diffraction-limit imaging by stochastic optical reconstruction microscopy (STORM)," *Nature Methods*, vol. 3, no. 10, 2006, pp. 793-795.

[85] S. Wang, "A Molecular-scale Programmable Stochastic Process Based On Resonance Energy Transfer Networks: Modeling and Applications," Ph.D. Thesis, Electrical and Computer Engineering, Duke University, 2016.

[86] S. Doose, H. Neuweiler, and M. Sauer, "Fluorescence Quenching by Photoinduced Electron Transfer: A Reporter for Conformational Dynamics of Macromolecules," *Chemphyschem*, vol. 10, no. 9-10, 2009, pp. 1389-1398.

[87] M. Heilemann, E. Margeat, R. Kasper, M. Sauer, and P. Tinnefeld, "Carbocyanine Dyes as Efficient Reversible Single-Molecule Optical Switch," *Journal of the American Chemical Society*, vol. 127, no. 11, 2005, pp. 3801-3806.

[88] H. Brismar, and B. Ulfhake, "Fluorescence lifetime measurements in confocal microscopy of neurons labeled with multiple fluorophores," *Nature Biotechnology*, vol. 15, no. 4, 1997, pp. 373-377.

[89] L. Qian, and E. Winfree, "Scaling Up Digital Circuit Computation with DNA Strand Displacement Cascades," *Science,* vol. 332, no. 6034, 2011, pp. 1196-1201.

[90] J. Widengren, and R. Rigler, "Mechanisms of photobleaching investigated by fluorescence correlation spectroscopy," *Bioimaging,* vol. 4, no. 3, 1996, pp. 149-157.

[91] H. Ow, D. R. Larson, M. Srivastava, B. A. Baird, W. W. Webb, and U. Wiesner, "Bright and stable core-shell fluorescent silica nanoparticles," *Nano Letters,* vol. 5, no. 1, 2005, pp. 113-117.

[92] S. Zaiba, F. Lerouge, A. M. Gabudean, M. Focsan, J. Lerme, T. Gallavardin, O. Maury, C. Andraud, S. Parola, and P. L. Baldeck, "Transparent Plasmonic Nanocontainers Protect Organic Fluorophores against Photobleaching," *Nano Letters,* vol. 11, no. 5, 2011, pp. 2043-2047.

[93] W. C. W. Chan, D. J. Maxwell, X. H. Gao, R. E. Bailey, M. Y. Han, and S. M. Nie, "Luminescent quantum dots for multiplexed biological detection and imaging," *Current Opinion in Biotechnology,* vol. 13, no. 1, 2002, pp. 40-46.

[94] M. D. Mottaghi, A. Rallapalli, C. Dwyer, and Ieee, "RETLab: A fast design-automation framework for arbitrary RET networks," *Design, Automation, and Test in Europe Conference and Exhibition*, 2014.

[95] A. Iqbal, S. Arslan, B. Okumus, T. J. Wilson, G. Giraud, D. G. Norman, T. Ha, and D. M. J. Lilley, "Orientation dependence in fluorescent energy transfer between Cy3 and Cy5 terminally attached to double-stranded nuclelic acids," *Proceedings of the National Academy of Sciences of the United States of America,* vol. 105, no. 32, 2008, pp. 11176-11181.

[96] S. Y. Mak, and D. H. Chen, "Fast adsorption of methylene blue on polyacrylic acid-bound iron oxide magnetic nanoparticles," *Dyes and Pigments,* vol. 61, no. 1, 2004, pp. 93-98.

[97] R. I. Masel, *Principles of Adsorption and Reaction on Solid Surfaces*, John Wiley & Sons, 1996.

Biography

Craig LaBoda was born on May 14, 1989 in Manchester, CT. In 2011, he received his Bachelor of Science in Electrical Engineering from Boston University. He was introduced to the field of DNA nanotechnology while studying the photolithographic synthesis of DNA under the guidance of the Department Chair, Professor Franco Cerrina. After graduating with his B.S., Craig joined the Self-Assembled Systems Group at Duke University, where he received his Master of Science in Electrical and Computer Engineering in 2013. His Ph.D. thesis focuses on the development of RET-based devices and circuit design strategies for building scalable integrated molecular circuits.

Publications:

[1] C. LaBoda, A. Lebeck, and C. Dwyer, "An Optically Modulated Self-Assembled Resonance Energy Transfer Pass Gate," (Submitted).

[2] C. LaBoda, C. Dwyer, and A. Lebeck, "Exploiting Dark Fluorophore States to Implement Resonance Energy Transfer Pre-Charge Logic," (Submitted).

[3] C. D. LaBoda, and C. L. Dwyer, "Upconverting Nanoparticle Relays for Resonance Energy Transfer Networks," *Advanced Functional Materials*, vol. 26, no. 17, 2016, pp. 2866-2874.

[4] C. LaBoda, H. Duschl, and C. L. Dwyer, "DNA-Enabled Integrated Molecular Systems for Computation and Sensing," *Accounts of Chemical Research*, vol. 47, no. 6, 2014, pp. 1816-1824.